A STUDY OF CYTOPLASMIC MACROMOLECULAR CROWDING, REACTIVE OXYGEN SPECIES, AND MICRORHEOLOGY FROM THE PERSPECTIVE OF MAMMALIAN CELL VOLUME REGULATION

Thesis Submitted for the Degree of

Doctor of Philosophy (Science)

to

Jadavpur University

2022

by

Parijat Biswas

School of Biological Sciences,
Indian Association for the Cultivation of Science,
Jadavpur, Kolkata- 700032.
India

INDIAN ASSOCIATION FOR THE CULTIVATION OF SCIENCE
2A & 2B Raja SC Mullik Road, Jadavpur, Kolkata 700032, India

२ए एडं बी, राजा एस. सि. मल्लिक रोड, यादवपुर, कोलकत्ता-700 032, 2A & B, RAJA S. C. MULLICK ROAD, JADAVPUR, KOLKATA - 700 032
दुरभाष Phone : 2473-4971, 3372, 3073 फैक्स /FAX : (91) (33) 2473 2805, ग्राम / GRAM : इंडासन / INDASSON, यादवपुर / JADAVPUR

Date: 16.08.2022

Dr. Deepak Kumar Sinha
Professor
School of Biological Sciences
Indian Association for the Cultivation of Science
Jadavpur, Kolkata-700032, India
E-mail: bcdks@iacs.res.in, emaildks@gmail.com
Fax: +91 33 2473 2805
Phone: +91 33 2473 4971

Certificate from the supervisor

This is to certify that the thesis entitled- "**A study of cytoplasmic macromolecular crowding, reactive oxygen species, and microrheology from the perspective of mammalian cell volume regulation**", submitted by **Parijat Biswas**, Registration index number: **71/17/Life Sc./25**, who got his name registered on **16th August 2017** for the award of **Ph.D. (Science) degree of Jadavpur University**, is absolutely based upon his own work under my supervision, and neither this thesis nor any part of it has been submitted for either any degree/diploma or any other academic award anywhere else before.

Supervisor's signature
(Date with the official seal)
16/8/22

Dr. Deepak Kumar Sinha
~~Associate~~ Professor
Department of Biological Chemistry
I.A.C.S., 2A & 2B Raja S. C. Mullick Road
Jadavpur, Kolkata - 700 032, India

Declaration

The research work embodied in this thesis entitled "**A study of cytoplasmic macromolecular crowding, reactive oxygen species, and microrheology from the perspective of mammalian cell volume regulation**", being submitted to Jadavpur University, Kolkata, has been carried out under the supervision of Dr. Deepak Kumar Sinha, Professor, School of Biological Sciences, Indian Association for the Cultivation of Science. This work is original and has not been submitted in part or in full, for any degree or diploma to this or any other university.

Parijat Biswas
Index number: 71/17/Life Sc./25

Abstract

Index number: **71/17/Life Sc./25**

Thesis title: A study of cytoplasmic macromolecular crowding, reactive oxygen species, and microrheology from the perspective of mammalian cell volume regulation

Submitted by: Parijat Biswas
School of Biological Sciences,
Indian Association for the Cultivation of Science
Jadavpur, Kolkata- 700032

Synopsis

Cells can regulate their volume to acclimatize to the changing physicochemical external environment, like osmolarity of the extracellular fluid, as well as a response to various intracellular biochemical signalings, like cell cycle, apoptosis, necrosis, and transepithelial migration. In the aspect of cell volume regulation, the identity of a cell volume sensor remains unclear. The cell is effectively a closed system of densely packed macromolecules, any change in the intracellular macromolecule density can impact the thermodynamic activity of numerous biochemical processes. Hence, it is often proposed that the macromolecular crowding (MMC) in the protoplasmic fluid acts as a cell volume sensor. To establish intracellular MMC as a cell volume sensor, a reliable, quantitative probe is essential and currently lacking. We established that fluorescence anisotropy of EGFP (r_{EGFP}) can serve as a fast, high throughput probe for MMC, both *in vitro* and *in vivo*. We showed that r_{EGFP} scales linearly with increments in macromolecule density and is more sensitive to protein density than smaller molecules like polysucrose, amino acids, and salts. Further, r_{EGFP} is independent of solution pH, viscosity, and EGFP concentration. We found that the average intracellular MMC is distinguishably different among diverse cell lines. Intracellular r_{EGFP} measurements showed that the

cytoplasmic MMC is spatially heterogeneous despite free diffusion of macromolecules, and the organization of the actin cytoskeleton separates the regions of varying cytoplasmic MMC. We then used r_{EGFP} to study the intracellular MMC homeostasis and tested the role of MMC as a cell volume sensor. We found that cells maintain MMC homeostasis during volume recovery from osmotic shocks, but perturbing the intracellular MMC isosmotically does not trigger any cell volume change. Furthermore, cell spreading and microtubule depolymerization enlarge cell volume, ignoring the changes in intracellular MMC. Hence, we hypothesized that MMC is not a cell volume sensor, but alternately proposed sensors like the plasma membrane may be more relevant. We found that pharmacologically inhibiting TNFR1 (Tumor Necrosis Factor Receptor 1) activity increases plasma membrane tension and arrests cell volume regulation during anisotonic challenges, microtubule disruption, and cell spreading. Hence, we propose that the plasma membrane is a more relevant cell volume sensor. We then investigated the biochemical influences of cell volume and cell morphology on the physiology of adherent cells. We found that detaching cells from their adhesion points leads to oxidative stress, while the reintroduction of adhesion-promoting substrates rescues the cells from oxidative stress. However, not allowing cells to spread after attachment makes the oxidative stress persist, and the persistence of intracellular oxidative stress increases the mechanical viscoelasticity of the cytoplasm.

Supervisor’s signature Candidate’s signature

Acknowledgments

"*I am not a self-made man; I got a lot of help.*"- Arnold Schwarzenegger

As a schoolboy fascinated with all things science, obtaining a Ph.D. degree seemed like an ultimate goal that provided the license to be a scientist. At the end of more than six years of studying Biology while being an "outsider" with training in Physics, I feel like the more I know, the more I realize how little I know. A Ph.D. is not a license to science, but a tedious battle training for the big war on the frontiers of the unknowns of human knowledge. Obtaining a Ph.D. degree is not a milestone, but merely a stepping stone for a long way uphill the mountain of science. However, just reaching this stepping stone is an arduous task, one that requires consistent effort, constant attention, relentless motivation, and numerous sacrifices to deal with the uncertainties of experiments and the confounding variables in the emerging hypotheses. And the journey to this stepping stone is vehemently difficult to undergo without proper guidance and encouragement, and I am fortunate to have both.

I will start by thanking my Ph.D. supervisor, Dr. Deepak Kumar Sinha, for allowing me to work in his lab and guiding my trajectory through all these years. But I am truly grateful to him for giving me the privilege to oppose his ideas and encouraging my free thinking and giving me the opportunities to prove my conjectures. I am thankful for his trust in my scientific findings despite the many disappointments I made him endure, for teaching me to dare without the fear of failure, and for training me in the ways of communicating my research through many, many, many group meetings. More than everything, I have learned a lot from him regarding how to approach the problems of science or life, and for that, I would always be grateful.

I want to thank Dr. Bidisha Sinha and her group at IISER Kolkata, particularly, Dr. Rinku Patel, Dr. Arikta Biswas, Madhura, Tithi, and Jibitesh, for providing every assistance and friendly support I needed during Bioscopy 2019 and my Ph.D. tenure. I would also like to extend my gratitude to Dr. Aprotim Mazumdar and Kesavan of TCIS Hyderabad for their incredible help during FLIM imaging.

I want to thank Dr. Prosenjit Sen, Dr. Prashant Chandra Singh, Dr. Prasanta Kumar Das, and Dr. Raja Paul for evaluating my progress during my tenure at IACS.

The two people pivotal for anything and everything I have achieved in my Ph.D. is Dr. Asmita Dutta and Dr. Mahesh Agarwal, my seniors whom I look up to in lab and life. Outside the academics and research stuff, Asmita-di taught me how to have an organized approach towards problems, scientific or otherwise, how to be patient, and how to stand your ground and push your ideas through, come rain or thunder. Mahesh-da has taught me how to be cool under pressure and how to be resourceful enough to get seemingly impossible tasks done in the quickest possible way and has been an all-time inspiration for his lightning-fast problem-solving ability, something I have seen in very few people and something I aspire to match someday. Above all else, if these two extremely good and caring human beings were not my seniors, I very much doubt that I would have survived the initial years of my Ph.D. They taught me the basics and the fundamental know-hows of the lab; they established the cordial and vibrant work culture that still exists in the lab; and they have supported me and continue to support me in matters of profession or life, be it physical health or mental. And I will be eternally grateful to them.

I will thank Dr. Anindita Bhattacharya, Arka Ghosh, and Dr. Deblina Sain Basu, the other eminent seniors of mine, for undergoing a lot of pain while teaching me the basics of molecular biology. I will thank Dr. Rinku Patel for the many enlightening discussions about the dynamics of actin and focal adhesions. I will also thank Dr. Abhishek Roy and Dr. Kaushik Das, alumni of Dr. Prosenjit Sen's group at IACS, for showing me how to culture the MDA-MB-231 cell line in the cleanest possible way. I would like to thank Dr. Prabuddha Gupta for imbibing me with his passion for science and enlightening me with his humor. I would also thank Dr. Sampali Banerjee, Dr. Sukanya Bhattacharya, and Dr. Ruma Sarkar for all the insights they have imparted to me during my tenure. The list of seniors, from my own lab or outside, is too long to enlist here, so I will conclude right here with my heartiest thanks. A special thanks to Mithun-da for showing me Hyderabad and the biryani in Paradise.

Among the current compatriots in my lab co-traveling the Ph.D. journey, without whom life in the lab is colorless, I sincerely thank Sudipta, Priyanka, Subhamoy, Dipanjan, and our newest member Sayani, for all the cheer and joy they bring to

the otherwise seemingly dull day-to-day lab life. And while not officially a part of the lab, Debapriya-di too. I have been extremely fortunate to have such wonderful lab mates all throughout my Ph.D. tenure, who have supported me in times of joy and in times of great anguish. It has been a delight sharing so many adventures and misadventures with you. It has been a privilege knowing you all. Other people have coworkers in their lab, I have friends.

Speaking of friends in IACS, I consider myself extremely lucky to have so many. Arpana, Srijita, and Sangheeta are my neighboring peers and have shared many a burden bestowed by the life of a Ph.D. scholar. Occupying a very large fraction of my heart is our humble pack of boyz- Abhik, Apurba, Dipanjan, Kingshuk, Mahesh-da, Subhamoy, Subhanka, and Subhasis. Be it the trip to the riverside for chop-muri, or the pineapple juice worth INR200 after paragliding in Pokhara, the wrestling with tumultuous seas in the rain, or our games of table tennis and Tekken, or the many sessions of meat, mead, and majestic laughs that we have shared as comrades, I will never forget them. I will be forever indebted to you all for never leaving me alone in all the dark times I have been through. Words cannot do justice to the great compadres that you are. Subhanka, a rare combination of brain and brawn, carries a gigantic heart filled with nothing but kindness and has been taking care of me since we were roommates during our Masters. Abhik is one of the most resourceful people I know and his timely humor can light up the darkest of rooms. Dipanjan's incredible grasp of all things tech and excellent quotes can catch you off guard anytime. Subhamoy's passion for science mirrors my own and his dedication to the art far surpasses mine. Apurba's earnestness melts the toughest of rocks, and Kingshuk's practicality is something to learn from. And I would like to especially thank Subhasis for imparting me his great wisdom when I was in dire need of it. Off IACS, Mostafizur, Anamul, Samik, Dipanjan, Sasthi, Tapas, Rup, Sayan, Ikbal, Subhendu, Subhadeep, Priyabrata, and Koushik, to name only a few of my masters' mates, have made these last eight years much memorable. My childhood buddies Debajit, Sayantan, Gayerike, Indranil, and Animesh, I thank you for being friends with me despite my non-participation in all the shenanigans.

I want to thank Sushanta-da, Pratap-da, Manoj-da, Asim-da, and Samar-da of the IACS workshop for engineering the electromagnet and many a mechanical devices for our experiments. Sovan-da of the SBS office and Sujit-da and Sasanka-da of

the academic office were extremely helpful for any queries regarding the official formalities in IACS.

I have had the delight of having the most wonderful trainees in the lab who have helped me in a lot of my experiments. Radhika had painstakingly dissected and isolated the salivary glands from Drosophila larvae and had taught me the techniques. I must thank Dr. Riddhi Majumdar for generously providing us with the Drosophila culture equipment and the Actin-GAL4-UAS-GFP flies. Rohit had done a wonderful job of studying the diffusion of EGFP and actin-GFP through FRAP. Rounak compiled a massive database of literature to understand the role of cell morphology in oxidative stress. All the other wonderful people who have done their projects in our lab during my tenure- Subham, Sourish, Sukanya, Sreejita, Upama, Nirjharini, Nandana, Jagaran, Debasrija, Ridita, Dev, and Nirikshan, I thank you all and wish you the very best. I have to especially thank Upama for providing valuable advice regarding protein solubility and proteasome biology. And a very special thanks to Soumik for all the entertaining days during his tenure.

The list of teachers who have made me who I am today is inexhaustible. However, I cannot fail to mention Chitrita-miss for encouraging my love for Physics and science as a whole, and for disappointing Saswati-miss for never learning Chemistry properly despite her best attempts. I must thank Prosenjit-sir for imbibing the love of coding within me, and Chandana-miss, Chinmoyee-miss, Nandini-miss, Pompa-miss, and Aditi-miss for nurturing my English language abilities, the relevance of which I am finding right now while writing to express my research.

Last but not least and above everything else, I will not thank my mother because nothing I say can fulfill the void that I have created by not taking responsibility and selfishly pursuing a career in science. I am not fit to thank her for her never-ending support and I will never be able to repay this debt. I can only hope, and try my best, to make her proud of the sacrifices she made for me.

Contents

Prelude

The discipline of Biology encompasses studying Life and all its glorious complexities. Observing the behavior of organisms in specific environments, natural or otherwise, has always been the core principle of biologists. Evolution has led living organisms to create increasingly intricate pieces of biochemical machinery, and more often than not, a single biological phenomenon is influenced by other biological processes in the organism. It thus becomes essential to study the individual contributions of specific components in the biological machinery when they are isolated from the noisy microenvironment inside living organisms. Biologists have isolated living tissue material from organisms and cultured them in artificial nutrient-supplemented salt buffers, leading to the development of the so-called primary cell culture. With the advent of immortalized cell lines, even the need for primary cell culture has subsided for those cases where the observed cellular biochemical properties are conserved across species. Cell lines offer tremendous ease in the rigor required for culturing living organisms, and cells can be studied more closely in engineered environments that mimic a specific condition inside a living organism. Nevertheless, a question persists: how close are such cell lines grown *in vitro* to those present *in vivo*?

We culture cell lines on rigid substrates, like glass or plastic, sometimes coated with positively charged polymers like poly-l-lysine or extracellular-matrix derivatives like fibronectin, collagen, and gelatin. However, the physical microenvironment of cells inside a living organism is specific to the parent organ. Epithelial cells of the circulatory system are continuously exposed to pressurized, rhythmic liquid flow; skeletal myocytes and osteoclasts are attached to hard bones where they are constantly subjected to multi-directional tension and torsion; hepatocytes grow in soft liver tissue and may face variations in the substrate rigidity depending on the level of fibrosis; kidney and gut cells are facing repeated challenges due to shifts in

the extracellular osmolarity. Once we remove cells from such intricate systems and culture them in passive, sterile, enhanced salt buffers on a solid substrate of constant rigidity, how similar will they behave when compared with their counterparts in the tissue of the parent organ? Cells that adhere and spread on two-dimensional rigid substrates exhibit a typical morphology dictated by an increased number of focal adhesion points [1] and enhanced levels of filamentous cytoskeletal structures [2]. Even extracellular mechanical stiffness can influence a stem cell's fate [3]. Cells grown in three-dimensional, artificial substrates that mimic soft tissue are typically much closer to their counterparts in the living organism [4]. Hence, we must always consider that the results we see from experiments we perform on cell lines may not translate to the biology exhibited inside a living organism.

Nevertheless, when we want to really "look" inside a single cell, we do not have many more choices other than to take it out of its parent system and grow it on an optically transparent, rigid substrate, and label our biomolecule of interest with some other molecule that reacts to electromagnetic waves, giving some form of unique spectral signature. Embracing the philosophy of "Seeing is Believing", scientists have, still are, and forever will be looking for new ways to look into cells, try to understand the physics and chemistry of the cytoplasm, study the dynamics of the biochemical processes, and get cleaner, sharper maps of single-molecule localizations inside a cell. This thesis will cover a few such biophysical techniques, their application in unprecedented circumstances, and how they helped uncover the contributions of macromolecular crowding and reactive oxygen species in regulating one of the most fundamental aspects of cell biology- cell volume regulation.

Chapter 1: Introduction

The sustenance of a living cell relies on its energy production capacity as well as the efficiency of energy transport logistics. Assuming identical functionality, a cell of a comparatively large size consumes more energy to survive than a smaller cell. The two primary energy currencies in the cytosol are ATP (Adenosine triphosphate) and GTP (Guanosine Triphosphate). To drive the machinery of Life, however, the sourced energy must be transported to the individual components of the cell. The general intracellular transport processes are, in essence, diffusion mediated. Even directed transport requires a continuous supply of ATP to run the molecular motors, and the ATP supply is ultimately mediated via diffusion. In this reaction-diffusion system of Life, the efficiency of intracellular transport is, thus, a critical factor in determining the survivability of a cell. In a cell having a comparatively large volume, the transit distances increase, making the delivery logistics slow and inefficient.

Moreover, an increase in the size of a cell results in the cell volume increasing at the rates of length units cubed, while the cell's surface area increases only at rates of length units squared. Hence for a comparatively large cell, having less membrane surface implies that the exchange rate of materials through the cell membrane is insufficient to meet the cell's energy needs. Therefore, the biochemical kinetics of a relatively large cell will be much slower than a smaller cell, making the large cell's reaction to external stimuli slower, effectively making the cell incapable of adapting to harsh environments. The surface-area-to-volume ratio of a cell is thus one of the crucial determinants of cell size and is one of the foremost physical reasons behind why a cell divides instead of continuous growth and why the more complex lifeforms are multicellular rather than unicellular. Therefore, the size of a cell is an important parameter to consider when evaluating questions about the functions of Life. A cell's size, or more specifically, its volume, changes at each stage of its life cycle, hand-in-hand with the

intracellular metabolism. In multicellular organisms, the variations observed in cell volume are almost always dependent on the function of the cell. Also, there exist variabilities in the volume of functionally identical cells, which could depend on the cell cycle stage or any stress factors that affect cell volume.

Changes in the cell volume generally arise from shifts in the osmolarity of the extracellular fluid, whence a cell exhibits a remarkable property- adjusting its volume back to pre-stress conditions. This adjustment process is called *cell volume regulation*. The chemical composition of the plasma membrane is inherently opposed to water exchange, but the specialized water channels- aquaporins, enable cells to control water exchange through the membrane directionally. Osmotic stress enforces water efflux/influx, thereby decreasing/increasing cell volume. The cell auto-restores its volume back to its pre-stress condition, wherein recovery from hyperosmotic shrinkage is called regulatory volume increase or RVI, and recovery from hypoosmotic swelling is called regulatory volume decrease or RVD. Alongside osmotic stress, many different biological conditions can induce cell volume regulation. Some critical conditions enforcing cell volume change are cell differentiation [3], necrosis [5], apoptosis [6], and transepithelial migration [7].

A question has always eluded scientists: how does a cell sense its volume? A popular hypothesis envisages that a cell “senses” its volume through the changes in cytoplasmic macromolecule density [8–13]. The volume of a cell and the density of its intracellular macromolecules are reciprocally related. Any perturbation in a cell’s volume instantaneously affects the density of the cytoplasmic molecules. The proponents of the above hypothesis reason that the density of solutes having a high molecular weight (i.e., macromolecules) is relatively high in the aqueous intracellular microenvironment. This density is significantly higher at the physiological pH conditions than what we can generate *in vitro*. Besides, cell volume regulation is always associated with an exchange of organic and inorganic molecules (i.e., osmolytes) between

the cytoplasm and the extracellular environment, implying that cells try to balance the internal and external osmolarities. Thus, one can claim that the extreme number density of the cytoplasmic macromolecules must have an entropic effect on the intracellular thermodynamic activity, changing proportionally with cell volume fluctuations. A closer look reveals that proteins are plentiful in the cytoplasm, and depending on the cell type, intracellular protein concentrations can range from 90 to 400 mg/ml [14]. Among the biologically significant macromolecules- proteins, nucleic acids, lipids, and polysaccharides, account for ~56%, ~23%, ~9%, and ~3% of a cell's dry weight [15]. The physical sizes of these intracellular macromolecules are not negligible. For instance, the hydrodynamic radii of individual proteins generally vary between 2 to 15 nm [16]. The sum of the volumes of all individual cytoplasmic macromolecules amounts to about ~30% of the total cell volume [17]; thus, only about ~70% of the intracellular space is free for diffusion and hosting biochemical reactions (ignoring solvent molecules) (**Figure 1.1**).

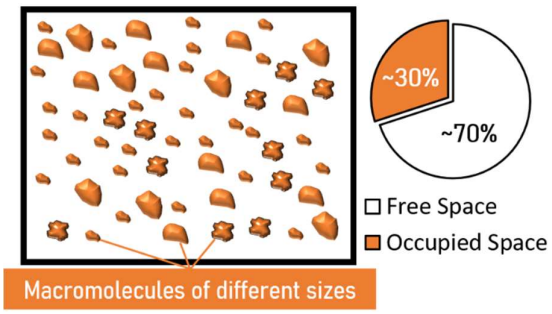

Figure 1.1: Cartoon representation of the intracellular space occupancy. Inside the illustrative cell boundary (black box), macromolecules of different sizes (orange) occupy ~30% of the cell volume.

This decrease in free space thus increases the effective macromolecule concentration for a given cell. As a result, the probability of interaction between macromolecules rises, which may further accelerate reaction kinetics and self-association. Concurrently, the increased interactions may also hinder a macromolecule's movement in the cell, thus decreasing the actual reaction rates. The simultaneous rise of effective concentration and diminution of mobility creates a chemical conundrum in the cytoplasm, which emerges as an entropic effect- Macromolecular Crowding [18,19].

1.1. Macromolecular Crowding

A “crowded” solution differs from a “concentrated” solution because a so-called crowded solution does not have a single solute species of macromolecule explicitly present in high concentrations. Instead, a significantly large number of solute species present in relatively moderate concentrations increases the overall macromolecule density in a crowded solution. So for two solutes that interact chemically, the rest of the solute species generally act as nothing more but space-filling inert “crowders”, which non-specifically affect the biochemical reaction rates through the *excluded volume effect*. This effect arises because a macromolecule has a finite size and cannot access the physical space already occupied by another macromolecule. The finite size and additional steric repulsions make each macromolecule “exclude” every other macromolecule from its occupied zone in space. To illustrate the principle of excluded volume, let us assume the macromolecules as hard spheres whose centers describe their positions in space. The spheres have no specific attractive or repulsive interactions and are assumed to be suspended in a solvent medium whose constituent molecules have nominal size. One such sphere can approach another from any random direction, and the distance of the closest approach between two such spheres is when their surfaces touch, which amounts to the sum of their radii (**Figure 1.2**).

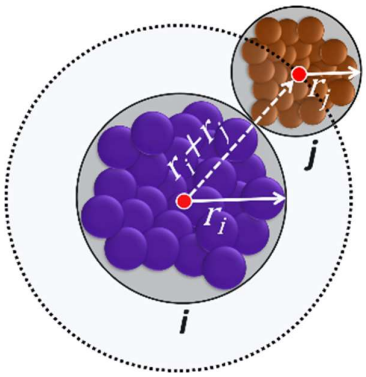

Figure 1.2: A macromolecule (i) approximated as a hard sphere of radius r_i excluding another such sphere (j) of radius r_j, results in an excluded spherical volume having a radius ($r_i + r_j$)

If a sphere (i) of radius r_i excludes another sphere (j) of radius r_j, then the excluded volume for i, which is inaccessible to the center of j is-

$$^4/_3\,\pi(r_i + r_j)^3 \qquad \ldots i$$

Thus, the total excluded volume for the *center of* j is larger than the physical volume of the individual macromolecule i. If the two molecules are identical (the radii of both are equal), the excluded volume is 8-times the volume of the spherical macromolecule. However, the total excluded volume for a pair of identical spheres is still 8-times the volume of a single sphere, as the excluded volume is the same region of space for both spheres. So, to avoid counting the excluded volume twice, the total excluded volume for two identical spheres is halved, that is, 4-times the volume of one macromolecule.

The volume exclusion phenomenon influences the entropy of tightly packed solutions [20]. Due to volume exclusion, the available free space shrinks, reducing the number of ways the macromolecules can occupy positions in the intracellular space. Let us imagine the intracellular space as a system of boxes, where the black boxes describe positions already occupied by macromolecules, and the white spaces represent free spaces occupiable by a macromolecule (**Figure 1.3**).

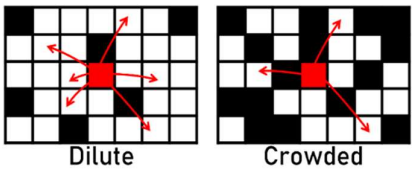

Figure 1.3: The number of ways the red box can occupy one of the white spaces is less in the crowded system

For a freely diffusible macromolecule (central red box), the number of occupiable boxes is less in the crowded system than in the dilute system. Keeping the positions of the black boxes fixed, the position of the red box in any white space corresponds to a single configurational microstate of the

system. The number of ways the red box can occupy one of the white spaces corresponds to the total number of configurational microstates (Ω) of the system. The total number of configurational microstates is observably less in the crowded system, and so, the crowded system has less entropy (S) compared to the dilute system, as-

$$S = k_B \ln \Omega \quad \text{... ii}$$

The resultant decrease in entropy increases the free energy (G) of the system since-

$$G = H - TS \quad \text{... iii}$$

where H represents the system's enthalpy, T represents the system's temperature in Kelvin, and k_B denotes the Boltzmann constant. An infinitely dilute solution of macromolecules is effectively free of any solute-solute interaction and behaves like an ideal system. The thermodynamic activity of an ideal system is simply equivalent to the solute concentration. Progressively increasing solute concentrations forces the solution to deviate from ideality, making the thermodynamic activity inequivalent to the solute concentration, even without attractive/repulsive forces. The increase in the partial molar free energy, or chemical potential (μ_i) of any species i present in a crowded solution, manifests through its thermodynamic activity $a_i = c_i\gamma_i$ (c is the concentration, γ is the activity coefficient), following-

$$\mu_i = \mu_i^{\Theta} + k_B T \ln a_i = \mu_i^{\Theta} + k_B T \ln c_i + k_B T \ln \gamma_i \quad \text{... iv}$$

where μ_i^{Θ} refers to the chemical potential of the i^{th} species in a specified standard condition. If the macromolecules do not interact, as in the ideal case, then $\gamma_i = 1$, but when they do, as in crowded conditions, $\gamma_i > 1$. The rise in free energy due to volume exclusion translates to an increase in γ_i. This increase in γ_i can be deconstructed into components contributing to the

total excluded volume of the system due to two-particle, three-particle…n-particle interactions. Using the virial theorem [20,21], one can expand $\ln \gamma_i$ as-

$$ln\,\gamma_i = \sum_j \alpha_{ij} c_j + \sum_j \sum_k \alpha_{ijk} c_j c_k + \cdots \quad \ldots v$$

Where,

$$\alpha_{ij} = V_{ij}^{Excluded} - V_j \quad \ldots vi$$

Here, $V_{ij}^{Excluded}$ is the total volume of macromolecule i excluding the macromolecule j and V_j is the volume of macromolecule j (**Figure 1.2**). The summations denote the contributions to excluded volume by interactions in all two-particle, three-particle…, and n-particle systems. For >2 particle volume exclusion, the virial coefficients become- $\alpha_{ijk} = V_{ijk}^{Excluded} - V_j - V_k$.

As all systems tend to maximize S, systems tend to minimize the excluded volume by favoring conformations that occupy the least space. Two good examples of this tendency are protein folding and protein aggregation.

Consider the case of a protein folding from unfolded (U) to folded state (F) according to $U \leftrightharpoons F$ (**Figure 1.4**).

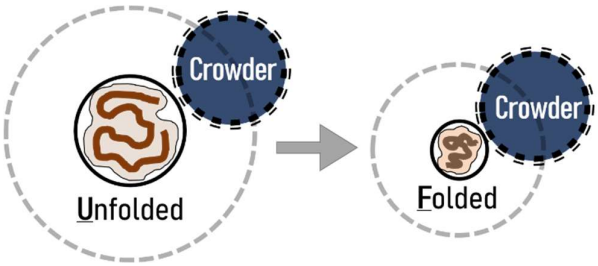

Figure 1.4: The unfolded state **U** creates a larger excluded volume for the non-interacting crowder macromolecules than the folded state **F**; thus, the system favors the folded state with the smaller excluded volume.

Mathematically, we can express the chemical equilibrium constant K_{eq} for the reaction $U \leftrightharpoons F$ by taking a ratio of their respective thermodynamic activities, as in-

$$K_{eq} = \frac{a_F}{a_U} = \frac{[\,F\,]\,\gamma_F}{[\,U\,]\,\gamma_U} \qquad \dots vii$$

Now, inside a cell, if we ignore the chemical reactivity of the remaining intracellular macromolecules with the folding protein in context, they essentially function as inert crowders- C. Due to the high concentration of such crowders, we cannot neglect the excluded volume of the crowders. In the virial expansion of $\ln \gamma_i$ (Equation- $\boldsymbol{v}$), we can replace i with protein conformations U and F. Since we are considering two-particle interactions (between U and C, or $F$and C), we can neglect the ≥3 particle interactions. Applying a first-order approximation to Equation- $\boldsymbol{v}$, we get:

$$ln\,\gamma_U = \left(V_{UC}^{Excluded} - V_C\right)[C] \qquad or, \qquad \gamma_U = e^{\left(V_{UC}^{Excluded} - V_C\right)[C]} \qquad \dots viii$$

$$ln\,\gamma_F = \left(V_{FC}^{Excluded} - V_C\right)[C] \qquad or, \qquad \gamma_F = e^{\left(V_{FC}^{Excluded} - V_C\right)[C]} \qquad \dots ix$$

Putting the values of γ_U and γ_F in Equation- $\boldsymbol{vii}$ gives

$$K_{eq} = \frac{[F]\gamma_F}{[U]\gamma_U} = \frac{[F]}{[U]} e^{\left(V_{FC}^{Excluded} - V_{UC}^{Excluded}\right)[C]} \qquad \dots x$$

Now, the excluded volume for the folded protein F (**Figure 1.4**) is lesser than that of the unfolded protein, i.e., $V_{FC}^{Excluded} < V_{UC}^{Excluded}$. Therefore, the term ${\gamma_F}/{\gamma_U} < 1$. Since $K_{eq} \rightarrow 1$, the reaction increases the concentration of the folded state, F. Crowding favors protein folding in the cell, and higher crowder concentrations $[C]$ increase $[F]$ exponentially. Replicating the crowded intracellular conditions is difficult *in vitro*. Since any biochemical reaction *in vivo* is exponentially faster than the same reaction *in vitro* in a

dilute solution, we should be careful while comparing reaction kinetics observed *in vitro* vs. *in vivo*. However, one must consider that proteins start folding mainly to minimize the exposure of their hydrophobic regions to intracellular water and attractive interactions between their internal components. The excluded volume effect of a crowded environment merely makes protein folding entropically favorable.

A similar logic can explain the effect of excluded volume on protein aggregation. Consider the aggregate state of n identical proteins (**Figure 1.5**).

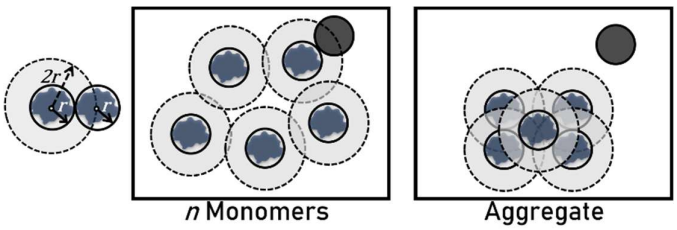

Figure 1.5: The total volume excluding the dark gray sphere is higher in the case of separated monomers than the aggregate.

In the reaction $nProtein^{monomer} \leftrightharpoons Protein^{aggregate}$, the overlap of the excluded volumes of individual proteins in the aggregate makes the total excluded volume far less than the total excluded volume of the n individual proteins. Hence, aggregation is entropically more favorable in a crowded solution. Then again, in cells, such aggregates form only when there is some degree of attractive interaction between the individual proteins, and it is the intensity of the attractive forces that primarily determines the degree of aggregation.

Now, macromolecular crowding also profoundly affects the diffusivity of intracellular macromolecules. The diffusion rate (D) of a macromolecule species is a product of the mean free path (λ), and the root-mean-squared velocity (v_{RMS}), that is-

$$D = \lambda v_{RMS}$$

... xi

The root-mean-squared velocity (v_{RMS}) is a function of the kinetic energy of a macromolecule, which depends on the system's temperature. A cell generally maintains a constant physiological temperature, and crowding has no effect on v_{RMS}. The mean free path (λ) of a macromolecule is defined as the distance traveled between two successive collisions. Thus, the λ of a macromolecule is a function of its cross-section area and the number density of the macromolecule in the solution. Assuming Maxwellian velocity distribution, the mean free path (λ) of a particle of diameter (d) and number density (ρ) is-

$$\lambda = \frac{1}{\sqrt{2}\pi d^2 \rho}$$

... xii

It is apparent that the mean free path (λ) decreases with increased crowding, that is, increased number density (ρ) of macromolecules. The decrease in the mean free path slows down the diffusion of macromolecules, as evident from Equation- $\boldsymbol{xi}$. The mean free path is also dependent on the diameter (d) of the macromolecule, implying that a smaller molecule has a larger mean free path than a comparatively bigger molecule. Hence, the effect of crowding on the diffusivity of macromolecules also depends on the molecule's size.

The effect of macromolecular crowding on intracellular biochemical reaction rates is highly ambiguous (Ma & Nussinov, 2013; Vöpel & Makhatadze, 2012). Consider the formation of a complex made of an enzyme (E) and a substrate (S) inside a cell following the reaction [24]-

$$E + S \leftrightharpoons ES^* \leftrightharpoons ES$$

... xiii

Where, ES^* is a transition state of the complex, and ES is the final oligomerization state of the complex. The rate of transition from the state

ES^* to the state ES is reliant on how much volume is excluded by each state (**Figure 1.6**).

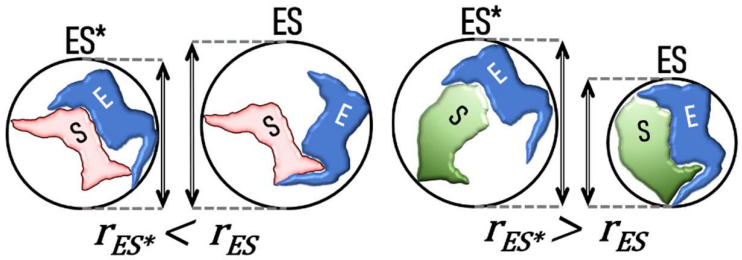

Figure 1.6: Crowding will entropically favor the formation of ES if it excludes lesser volume than ES^*.

The HIV-1 protease is an excellent example of the effect of crowding on intracellular enzymatic activity. The protease has a flap-like structure, and the inter-flap distance may range between 5 Å and 22 Å. Molecular dynamics simulations show that the opening of the flap-like structure of the enzyme is significantly obstructed in crowded environments [25,26].

The rate of ES^* formation also depends on the collision frequency of the molecules E and S, and thus, is limited by their individual diffusivities. A crowded environment will obstruct the motion of E and S, hence impeding the collision rate between them. If the rate-limiting step of the reaction $E + S \leftrightharpoons ES$ is dependent on the collision frequency between E and S, then crowding will slow down the formation of the final ES complex. If the rate-limiting step is the thermodynamic activity of ES^*, then crowding will speed up the formation of the ES complex. Another notable fact is the availability of E and S. If both species are present in sufficiently high number densities, crowding will not affect the encounter rate of E and S to a significant extent, and the thermodynamic activities of the ES complex will be the rate-limiting step for the reaction (**Figure 1.7**).

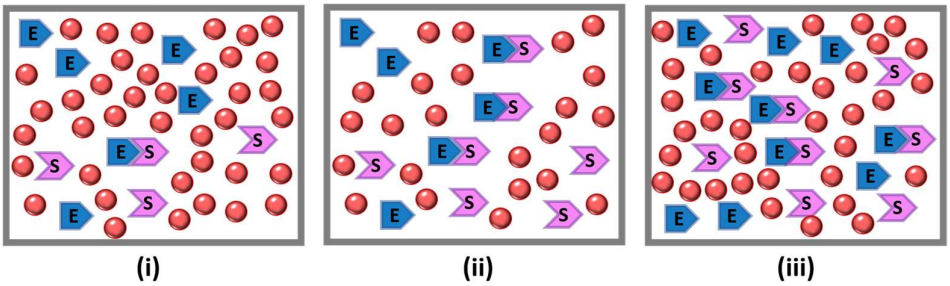

Figure 1.7: Three cases illustrating the effect of crowding on the reaction $E + S \leftrightharpoons ES^*$.
Case (i)- crowding impedes the diffusion of the individual macromolecules, thus reducing collision frequency and inhibiting the formation of the ES^*complex.
Case (ii)- reduced crowding promotes more encounters between E and S molecules, resulting in greater numbers of ES^*complexes.
Case (iii)- if the concentration of the enzyme or substrate is significantly high in crowded medium, then the collision frequency is not affected a lot, and the formation of ES^*complexes is not impeded much.

Since crowding decreases the entropy of the macromolecules, then does it violate the second law of thermodynamics? The answer is a resounding no. Cells contain a plethora of macromolecules of varying sizes, and **Figure 1.2** shows that for a given macromolecule i, the radius of the spherical volume excluding j depends on the size of j. Thus, the volume excluding a small molecule is much less than that of a larger molecule. When the excluded volumes of large macromolecules overlap, the smaller molecules gain more freedom of movement and, thus, more entropy. Hence the total entropy in a cell rises with the minimization of excluded volume. This entropy gain creates an interesting phenomenon: the *depletion-attraction force* [27,28]. The overlap of excluded volumes expels the smaller molecules from the regions of shared volumes. The overlap creates an uneven distribution of collision numbers made by the small molecules on the surface of the larger macromolecules. As the number of small molecules is depleted in the overlapped regions, there are more collisions on the exteriors than in the overlapped regions. Thus, a net entropic force pushes the large macromolecules closer, resulting in an attractive force between the macromolecules, described as depletion-attraction (**Figure 1.8**).

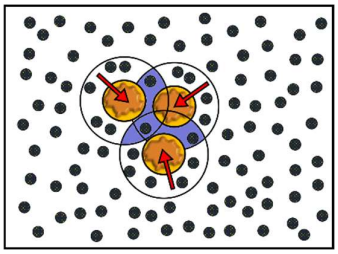

Figure 1.8: The number density of the small molecules (small black spheres) is less in the overlapped excluded volumes (blue areas) of the large macromolecules. So, the number of collisions on the exterior of the overlap of the large macromolecules is more than the interior, resulting in a net attractive force bringing them closer (red arrows).

The depletion-attraction phenomenon is one of the major driving forces behind the formation of compound macromolecular structures and biomolecular condensates [29]. Biomolecular condensates often form rapidly in the protoplasm or plasma membrane due to LLPS (liquid-liquid phase separation) [30]. The condensates are membraneless, macromolecule-rich pockets in the protoplasm with a locally enhanced thermodynamic activity [31]. Hypertonic challenge leads to the formation of such condensates, and altered reaction rates within the condensate affect the cell's regulatory volume increase process [32,33].

1.2. Tools for quantifying Macromolecular Crowding (MMC) in the cytoplasm

The role of MMC is undeniable in numerous physiological and pathophysiological processes [34]. Hence, the scientific community has been and is still actively pursuing new techniques to quantify the intracellular MMC levels with the highest spatiotemporal accuracy. Due to MMC's impact on the apparent viscosity of the cytosol, traditional diffusion measurements of fluorescent probes offer an indirect quantification of the local intracellular macromolecule density. FRAP (fluorescence recovery after photobleaching) and FCS (fluorescence correlation spectroscopy) can be used to probe the translational mobility of fluorescent molecules, while TR-FAIM (time-resolved fluorescence anisotropy imaging microscopy) offers rotational estimation [35–39]. Furthermore, customized fluorescent probes exhibiting

viscosity-sensitive spectral properties have also been used to probe intracellular protein densities [40,41]. The efficacy of such techniques has been verified by subjecting cells to osmotic stress [35,42–45] and inducing apoptotic shrinkage [41]. Nevertheless, as mentioned earlier, viscosity is merely an indirect indicator of crowding conditions, and the viscous drag felt by the probe molecule depends on its size [46,47]. So viscosity measurement is not a universal scale to compare crowdedness in different systems. Moreover, the viscosity of a solution crowded with proteins is significantly susceptible to protein-protein interactions (Yadav et al., 2011). It was only in 2015 that the idea of using FRET (Förster resonance energy transfer) as a sensor of MMC was proposed. Flexible polymer chains with fluorophores attached at each end were designed to undergo higher compactization in a crowded landscape. The fluorophores at each end, explicitly chosen to display FRET, come closer and exhibit higher energy transfer efficiency (**Figure 1.9**).

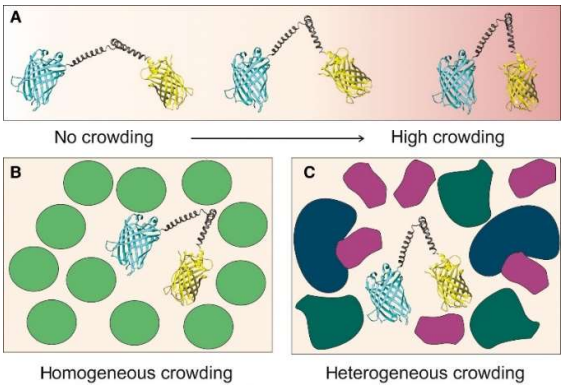

Figure 1. 9: Working principle of FRET-based crowding sensors. Adapted [206]

As for the nature of the polymer, it could be a polyether [49], protein [50,51], or nucleic acid [52,53]. While osmotic compression does induce an enhanced energy transfer efficiency, such FRET-based probes are more often than not dependent on the chemical nature of crowders populating their microenvironment. The environmental dependence arises because the FRET-based probes are not entirely immune to the intracellular landscape's ionic content, pH, or solvent viscosity. Moreover, FRET-based probes do not have a very high dynamic range owing to the very excluded volume effect it tries to measure. The two fluorophores can only come as close as their

combined radii. Hence the highest energy transfer efficiency cannot cross a certain threshold, and subsequently, the resolving power of the FRET-based probes is relatively low. Also, the bending rigidity of the biopolymer and the intrinsic solvent viscosity arising from temperature fluctuations could affect the maximum proximity of the FRET-pair fluorophores. Hence, a high-throughput, fast-sensing, reversible probe that solely reacts to MMC is still lacking for more thorough investigations of cytoplasmic MMC.

Raman microscopy, quantitative phase imaging, and optical tomography provide valuable tools for measuring the dry-mass content of individual cells, but such techniques are often computationally intensive, low-throughput, and require complex instrumentation [54–60]. An excellent, detailed discussion on crowding sensors has been reviewed by Michael Model (Model & Petruccelli, 2018).

1.3. Potential upstream sensors for cell volume regulation

While MMC has been firmly established to play a significant role as a cell volume sensor in mammalian red blood cells [62,63], this is still not the complete picture. Red blood cells contain significantly high levels of hemoglobin on average, about 340mg/ml [64]. Thus, MMC as a sensor for cell volume is highly plausible for red blood cells. However, since red blood cells are relatively simple systems compared to other mammalian cells, it is still not clear whether the dependence of cell volume on cytoplasmic macromolecule density will be upheld for all cell types. Plants, bacteria, and fungi use a comparatively simple osmosensing mechanism to regulate cell volume [10]. A protein (usually a kinase) located extracellularly senses the external fluid's osmolarity. The sensor then changes the activity of another kinase (making it the signal transmitter), and a different protein with a

receiver domain acts as a responder to begin the cell volume regulation process. The Hog1-MAPK (mitogen-activated protein kinase) pathway is especially relevant for yeast. MAPK has transcriptomic roles in mammalian cells facing hyperosmotic shrinkage [65–67], but the upstream sensor of the signaling cascade is still unclear. One of the kinases in the MAPK family, MAP3K15 or ASK3 (apoptotic signaling kinase), has been identified to be a key regulator in cell volume recovery under hypertonic stress [11,68]. Another vital member of the kinase family, the With-No-Lysine (WNK) kinase, is essential during cell volume regulation under hypertonic challenges [69]. Phosphorylation of serine-threonine residues of the cotransporters of NKCC1 ion channels by WNK kinases initiates Na^+, K^+, and Cl^- influx, while concurrently blocking the efflux of K^+ through the KCC channels. The cytoplasmic density of Na^+, K^+, and Cl^- increases, initiating regulatory volume increase.

Multiple studies have shown that mechanotransduction of the plasma membrane/cytoskeleton and intracellular ion densities play prominent roles in mammalian cell volume regulation. Transmembrane proteins organize themselves spatially, as dictated by the membrane tension (which changes with cell volume). Their conformation then affects the activities of the downstream pathways through the cytoskeleton or other proteins (signal transmission), which then initiates the cell's volume regulatory response, as illustrated in **Figure 1.10**.

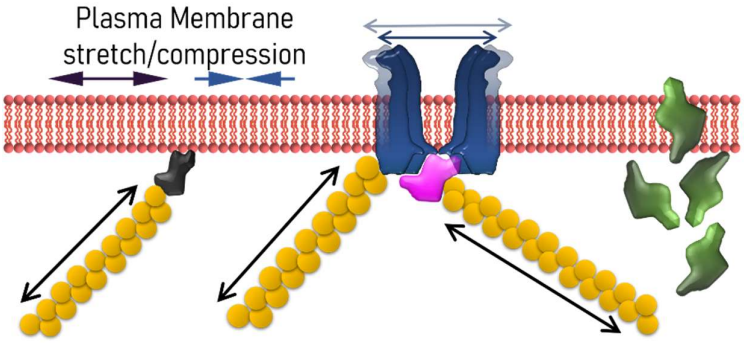

Figure 1. 10: Illustration of the postulates envisaging probable mechanisms of the plasma membrane conformation acting as a cell volume sensor.

The tension sustained by the plasma membrane (rose pink) could change the conformation of a transmembrane protein complex (blue), which further transmits signals through the cytoskeletal filaments (yellow), mechanically or biochemically. Tension may also affect the association of a membrane-binding protein (green), whose free-to-bound population ratio in the cytosol is responsible for cell volume regulation. A cytoskeleton-associated protein (magenta) binding with transmembrane proteins (blue) or another protein (black) binding directly with the membrane may have altered association kinetics under different magnitudes of membrane tension. Thus their biochemical activities act as sensors of membrane tension and cell volume. Cell volume-dependent phosphorylation/de-phosphorylation of the lipids in the membrane's inner leaflet, or a specific membrane protein, may also act as a volume sensor [70].

Aquaporins, caveolins, cavins, and proteins associated with tension-gated ion channels (Ca^{2+}, Cl^-, K^+, Na^+) are all membrane proteins implicated in cell volume regulation [71–74]. VRACs (volume-regulated anion channels) and proteins containing LRRC8A (leucine-rich repeat-containing protein 8A) like SWELL1 have been identified as potential cell volume sensors [75–80]. However, a comprehensive action pathway for such proteins has not been established yet. At the very least, it has been established that the tension sustained by the plasma membrane has an undeniable role in the later stages of cells' response to osmotic stress [74]. In adherent cells, the high abundance of integrin α/β heterodimers in the plasma membrane has led to the proposition that integrins may act as sensors of swelling-induced shear stress on the plasma membrane. Inhibiting integrin activity impedes regulatory volume decrease as a response to hypoosmotic cell swelling [81]. Integrin stretch-mediated VRAC activation has been shown in cardiomyocytes [82], and TonEBP (tonicity-responsive enhancer-binding protein) upregulation has been shown in renal epithelial cells [83].

In the cases of osmotic cell swelling/shrinkage, the excess membrane stored in caveolae can buffer the sudden stretch forces on the membrane [84]. The

cortical actin network is also responsible for alleviating most of the mechanical stress undertaken by the plasma membrane [74]. The cortical actin network binds with several membrane proteins, including integrins and VRACs [85,86]. The cytoskeletal filaments are a cell's primary mechanotransducers and are vital components of a cell's stress propagation machinery. They constantly reorganize in response to cell volume fluctuations, as shown during osmotic challenges. The transcription activators YAP/TAZ play vital roles in cell volume regulation, mediated by changes in the mechanical tension of the actin cytoskeletal network in response to cell volume fluctuations [87,88]. However, whether the cytoskeleton acts as the ultimate upstream cell volume sensor is still debatable.

The density of intracellular ions is another contender in the potential cell volume sensors list. The primary motivation behind this postulate is that cells start modifying their volume in the presence of elevated/depleted ionic content, specific or non-specific, even in isotonic environments [89–91]. The Pump Leak Model (PLM) [92] explains how a cell balances its intracellular and extracellular ion population and maintains its volume (**Figure 1.11**).

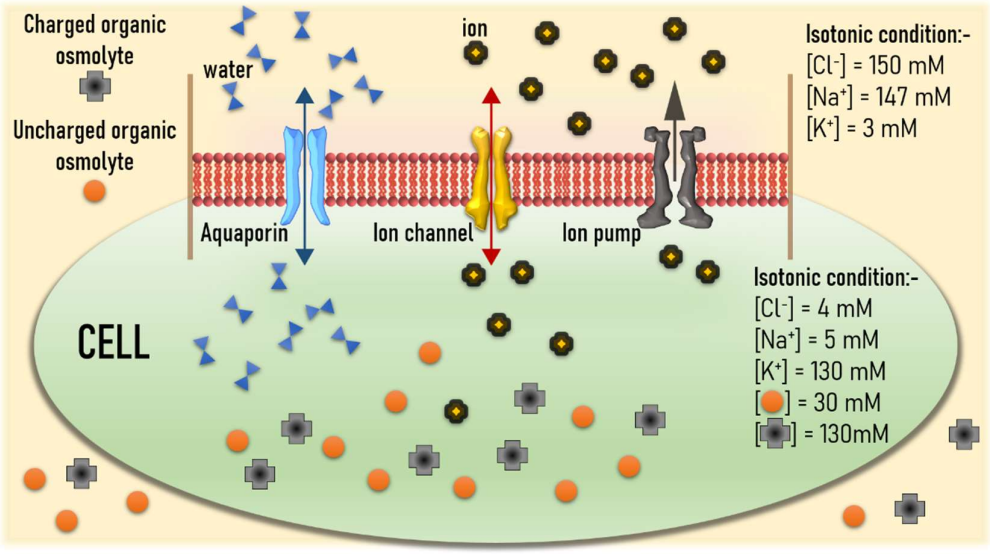

Figure 1. 11: The Pump Leak Model.

The net extracellular ion concentration is about ~300mM, while the net intracellular ion concentration is just ~150mM. Since most proteins are negatively charged, the extracellular anionic concentration is significantly higher (e.g., $[Cl^-]$ is 30 times greater outside the cell). $[K^+]$ is 40 times higher inside the cell, while $[Na^+]$ is 30 times lower [93,94]. The plasma membrane contains specific channels that allow ions and water to flow bidirectionally (the "Leak" of PLM) and actively regulated pumps that throw out ions (the "Pump" of PLM). Cells constantly pump out K^+ and Cl^- to maintain the ionic equilibrium between the intracellular and extracellular environments, and let aquaporins manage the water endosmosis/exosmosis to regulate cell volume. Cells also have organic osmolytes that could be charged or uncharged and are generally impermeable to the plasma membrane. However, during osmotic challenges, cells enforce the exchange of organic osmolytes like taurine to regulate volume [95], although the exchange rate is much slower than water molecules and ions. Calcium-dependent activities of multiple proteins may also be enforcers of cell volume regulation, but it is still unclear whether cytoplasmic ionic content is the upstream sensor of cell volume. Cells may also combine all the discussed sensing mechanisms to "know" their volume. Since much is still left unknown, more studies are needed to determine the complete mechanism of cell volume regulation. An overview of some response mechanisms to cell volume perturbation stimuli is highlighted in **Figure 1.12**.

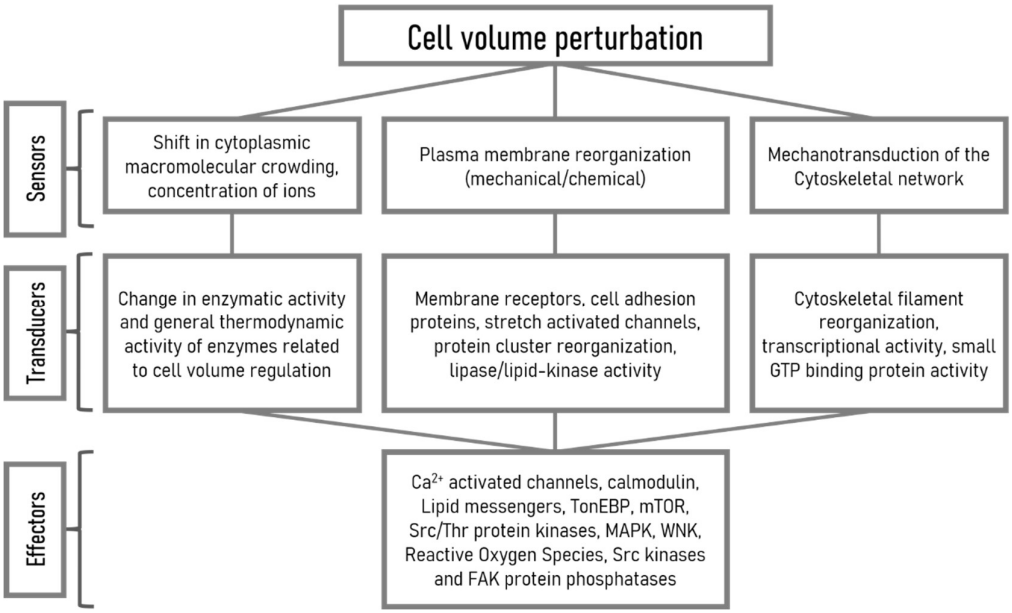

Figure 1. 12: Cell's response to volume perturbation

1.4. Downstream signaling in response to cell volume perturbations- the role of reactive oxygen species (ROS)

Even though the cellular volume regulatory mechanisms restore the cytoplasmic conditions to mitigate the ill-effects of osmotic stress, partially or entirely, the restoration does not happen instantaneously, and significant damage to proteins and DNA occurs rather quickly [96–98]. It is well known that osmotic challenges lead to the elevation of the cytoplasmic reactive oxygen species (ROS) levels [99–106] (**Figure 1.13** and **Figure 1.14**).

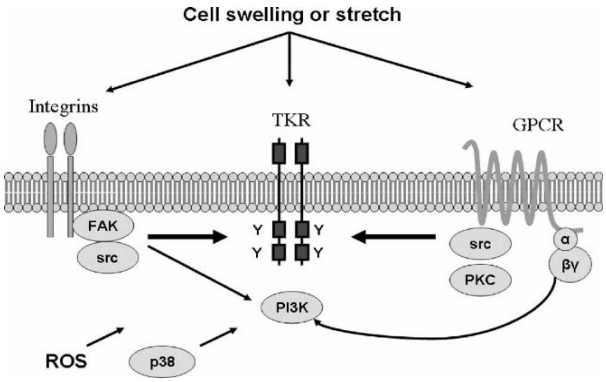

Figure 1. 13: ROS activity during hypotonic stress (cell swelling). Adapted [207]

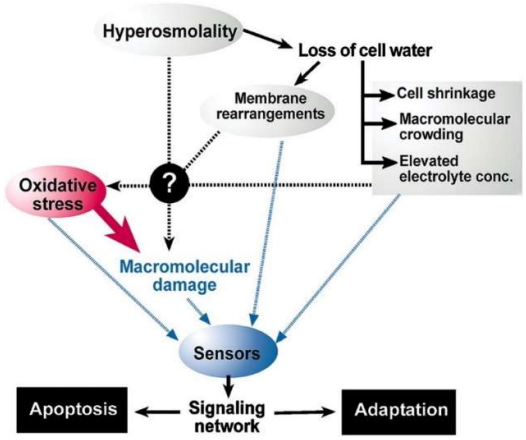

Figure 1. 14: ROS activity during hypertonic stress (cell shrinkage). Adapted [105]

While the exact mechanism behind the increase in ROS levels has not yet been identified, plasma membrane reorganization, MMC, and elevated cytoplasmic ion levels could lead to the observed oxidative stress. The damage to proteins from oxidative stress may persist until the complete abolishment of the osmotic stress.

Elevated ROS levels may trigger apoptosis, and the shrinkage of cell volume on the advent of apoptosis is termed apoptotic volume decrease (AVD). During AVD, it is natural to assume that the cell volume regulatory mechanisms are inhibited to facilitate programmed cell death. However, to combat apoptosis, cells selectively upregulate numerous processes to ensure survival. In rat hepatoma cells, oxidative stress induces volume shrinkage, but an increased influx of Na^+ and Ca^{2+} partially rescues cell volume [107]. A similar observation was found in a study on glial cells [108]. Multiple studies have further established that elevated cytoplasmic ROS

levels enhance the uptake of Na^+ and Ca^{2+} to increase the intracellular ion concentration, increasing the water influx rates and cell volume, thus stalling apoptosis [109–111]. In the cases of hypotonic challenges, cells have been found to exhibit ROS-dependent efflux of ions and osmolytes like taurine to counteract excessive swelling [95]. Thus, we can firmly say that ROS has a direct role in implementing volume regulation as a defense mechanism against unwanted cell volume perturbations.

Does ROS also regulate cell volume during natural processes where a cell's size fluctuates? Exemplarily, the volume of adherent cells changes considerably during spreading on stiff substrates. ROS has been implicated as essential for promoting proper adhesion in multiple studies [112–114]. A sudden change in cell spreading due to forced detachment from the substrate or cyclic stretch also induces cytoplasmic ROS elevation in adherent cells [115,116]. Our earlier studies have shown that elevated ROS levels directly affect the cytoplasm's mechanical stiffness [117].

During cell volume fluctuations, the cytoplasmic MMC levels, ROS, and the cell's mechanical stiffness are the physicochemical parameters that work in tandem to modulate several critical biological processes. The interaction between these factors has not been explored in detail and will be addressed in this thesis.

1.5. Scope and outline of the thesis

Cell volume regulation is a complex biological phenomenon encompassing many different molecular mechanisms and their mutual interactions. The thesis covers only a tiny aspect of the cell volume regulatory mechanisms- the components required for cell volume detection.

The second chapter includes a detailed description of the independent setup and calibration of the following biophysical techniques-

- FRAP (Fluorescence Recovery After Photobleaching)
- FAIM (Fluorescence Anisotropy Imaging Microscopy)
- PTM (Particle Tracking Microrheology)

The third chapter will cover the methodology of using fluorescence anisotropy of EGFP (Enhanced Green Fluorescent Protein) as a tool to probe intracellular macromolecular crowding (MMC).

The fourth chapter will encompass investigations on the nature of sensors of cell volume sensors- MMC and the plasma membrane organization.

The fifth chapter is a study on the involvement of ROS (Reactive Oxygen Species) in cell volume regulation during cell adhesion and spreading.

Finally, the main findings described in the dissertation have been summarized and the bibliography has been accounted for, along with the list of publications by the author.

Chapter 2: Independent setup and calibration of quantitative fluorescence microscopy techniques

Proteins implement virtually every biological process in a cell, which is why biologists study the expression levels of relevant proteins while investigating any physiological or pathophysiological function. However, sometimes the knowledge of protein expression levels alone is insufficient to understand the evolution of a biological process. Co-localization studies of different proteins or protein-nucleic acid oligomers reveal many insights into their mutual interactions. However, mere co-localization information is not enough to paint a complete picture of how such dynamic interactions affect intracellular biochemistry or how the physical state of the cell affects such interactions. Proteins are highly mobile inside a cell, exhibiting both the processes of *passive diffusive movement* and *active transport*. Hence measuring the time-evolution and binding kinetics of protein-protein interactions is equally important. Studying the shuttling of various proteins between different organelles or micro-compartments inside the cell is also necessary to understand numerous biological processes. Visualization of protein trafficking is easy if we can attach a fluorophore to it and observe its dynamics under a microscope. Moreover, we can physically modulate the properties of the fluorophore, and by employing additional mathematical modeling, we can generate a lot more insight into our biological process of interest than simply studying co-localization or expression levels.

FRAP (Fluorescence Recovery After Photobleaching), FAIM (Fluorescence Anisotropy Imaging Microscopy), and FCS (Fluorescence Correlation Spectroscopy) are some of the most well-established methods for studying protein dynamics, both inside and outside the cell body. FRAP and FCS can accurately measure translational diffusion and binding kinetics, while FAIM

is useful for estimating rotational diffusion, oligomerization, and cluster size/density. PTM (Particle Tracking Microrheology) provides information on the local mechanical stiffness and viscosity of the cell's interior or membrane, depending on where the probe is attached.

2.1. Fluorescence Recovery After Photobleaching (FRAP)

FRAP is a reasonably straightforward technique involving pulse-photobleaching a fluorescent probe of interest in a comparatively small region of a cell and then monitoring the recovery kinetics of the probe in the same region with a reasonably fast time-lapse imaging (**Figure 2.1**).

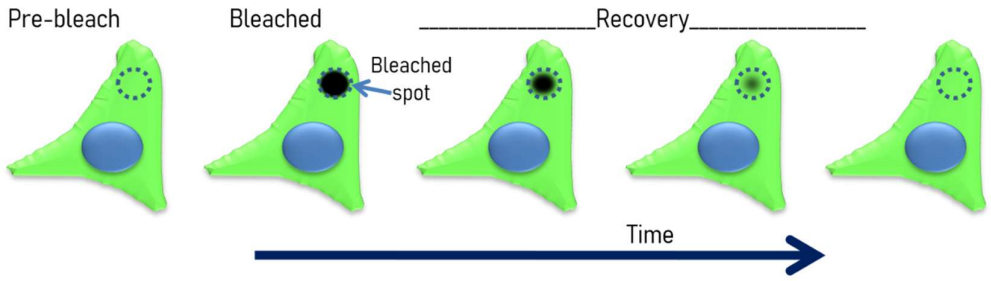

Figure 2. 1: Schematic of a typical FRAP experiment. Photobleaching the fluorophores inside the dotted circle and video-graphing the recovery inside the circle provides information on the translational diffusion rate of the fluorophore

The recovery rate is proportional to the rate of diffusion/transport of the fluorescent probe. Photobleaching ideally removes just the probe's fluorescence property while keeping its diffusive or interactive nature intact. The diffusion rate can be calculated by plotting the intensity of the bleached spot over time and fitting the resulting curve to an equation (**Figure 2.2**).

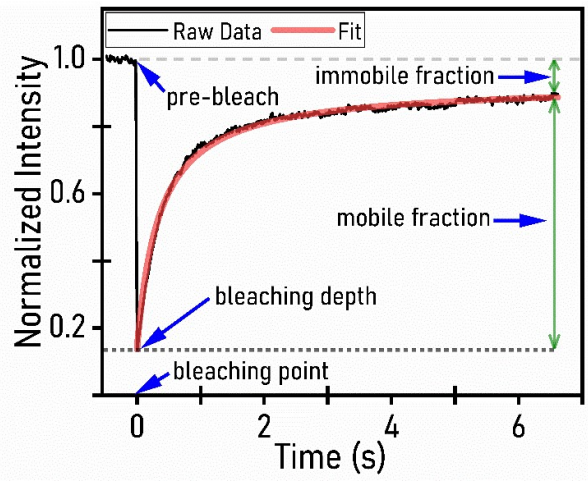

Figure 2. 2: The intensity of the region of interest (normalized by pre-bleach values) is plotted against time during pre-bleaching, bleaching point (at t=0s) and the recovery of intensity post bleaching. The experimental subject was a NIH/3T3 fibroblast expressing LifeAct-mEGFP, and a circular spot of diameter 2µm radius was photobleached in the basal plane of the cell containing ample actin stress fibers.

In **Figure 2.2**, the raw data (black) is fitted to the equation [118] which best describes the recovery kinetics. Since the recovery does not reach maxima, there exists an immobile fraction of the fluorophore population that is not exchanged between the bleaching spot and the rest of the cell in the time scales represented. There are two critical parameters in FRAP experiments- the bleaching depth, which refers to the maximum amount of photobleaching that can be visualized, and the actual bleaching area, which refers to the proper size of the photobleaching spot. Usually, there is a non-negligible time gap between the bleaching pulse and the acquisition of the first image post bleaching, and even pulse-photobleaching takes a finite time to occur. During this process, the fluorophores inside the bleaching spot may exchange with the surroundings and thus show a slight recovery- giving the maximum obtainable bleaching depth and area for data analysis (**Figure 2.3**).

Figure 2.3-A explains how the diffusive exchange between the fluorophores inside the expected bleaching area (white dotted circle) and the surroundings can effectively increase the actual bleaching area (black dotted circle). The increase in the bleaching area depends on the diffusivity of the fluorophores present. If the fluorophores show fast diffusion kinetics, the size of the actual bleaching area will be comparatively much larger. The

bleaching must occur in the shortest possible time to reduce this increase in the actual photobleaching area.

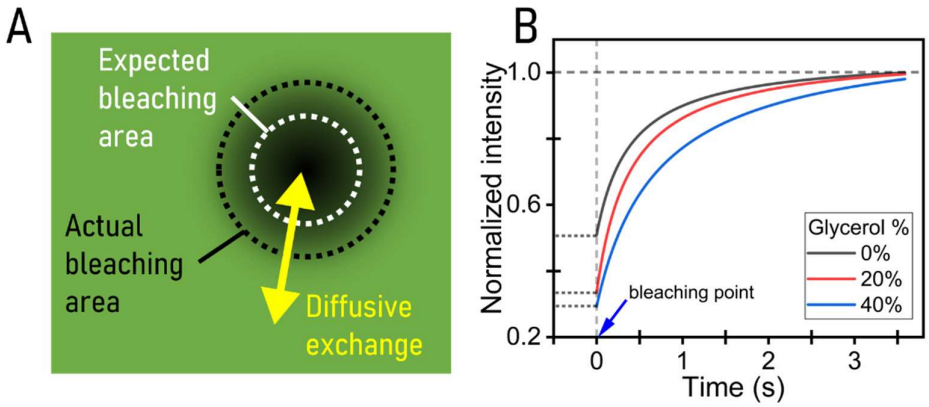

Figure 2. 3: (**A**) depicts the actual bleaching area vs. the expected bleaching area due to the exchange of fluorophores (green) between the bleaching spot and the surroundings. (**B**) shows the recovery kinetics of reconstituted EGFP in different mixes of Glycerol and 1xPBS (Phosphate Buffer Saline) at 25°C and pH 7.4.

In **Figure 2.3-B**, increasing the glycerol percentage naturally slows the recovery rate, and the bleaching depth increases with increasing solution viscosity because there is less exchange of fluorophores with the surroundings in the more viscous solutions. Bleaching depth depends on both the solution viscosity and the image acquisition rate, so when the diffusion rate of the probe is fast in the solution, the image acquisition rate must also be made faster so as to not miss the initial data points post photobleaching.

Another caveat of FRAP experiments is the persistent photobleaching while monitoring the intensity recovery. The general methodology of performing FRAP experiments is using a high-powered laser beam to photobleach the fluorophores in the shortest possible time and then imaging the recovery using a fluorescent lamp. The excitation light from the lamp is more than sufficient to photobleach all the fluorophores in the system. Hence, it is advisable to use low-intensity light to observe the recovery process. In laser-scanning-confocal microscopes, the excitation intensity must be reduced to

avoid this problem. Another method is a Point-FRAP system, where a high-intensity laser pulse is used to perform the photobleaching, and another low-intensity laser beam is used to image the recovery only in the bleaching spot. Imaging a small area prevents additional photobleaching in the rest of the cell area and reduces overall phototoxicity.

2.1.1. Point-FRAP setup for a wide-field epifluorescence microscope

While laser scanning confocal microscopy (LSCM) has made FRAP exponentially easier with customizable bleaching areas and shapes, LSCM is inherently slow and unsuitable for studying fast diffusion. LSCM photobleaches the area of interest sequentially in a Raster pattern. For fast diffusing species, there is a chance of recovery starting in the sub-regions that are bleached first. A FRAP setup in an epifluorescence microscope coupled with a high-powered laser system overcomes this artifact by quickly bleaching the spot in a short burst but sacrifices the ability to choose any shape for the bleaching area. Hence, setting up a Point-FRAP system on a wide-field epifluorescent microscope has some advantages. Our Point-FRAP setup can be coupled to any wide-field epifluorescence microscope with an open port and an accessible path leading directly to the objective. A diagram of setting up a Point-FRAP system using a single 488 nm LASER source is included below, with each component's function explained (**Figure 2.4**).

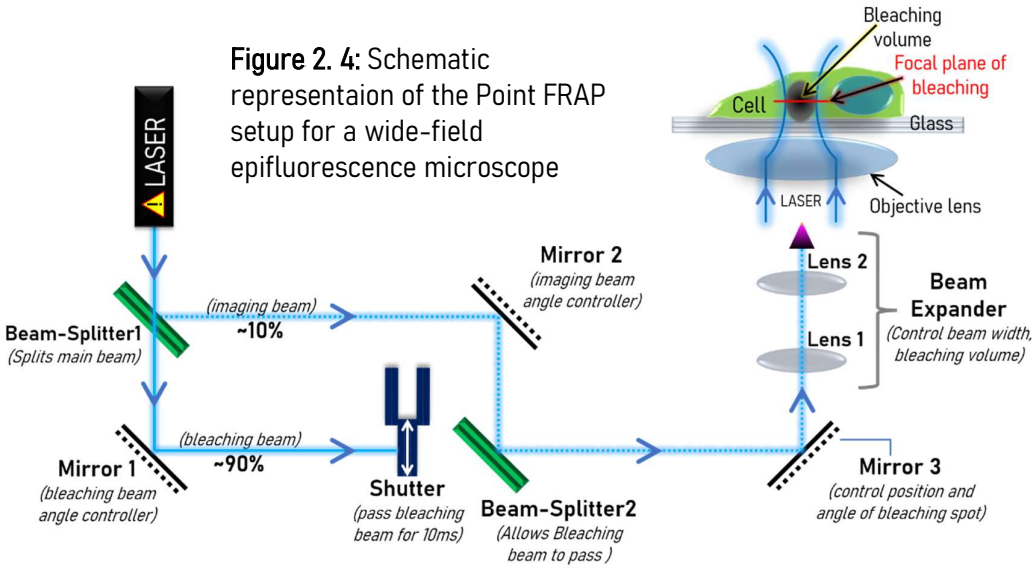

Figure 2. 4: Schematic representaion of the Point FRAP setup for a wide-field epifluorescence microscope

Briefly, the LASER beam is split in a 10:90 intensity ratio. The low-intensity (10%) beam will continuously illuminate a small spot of the cell, and the high-intensity (90%) beam is to be exposed for a short interval (using a shutter) to bleach the spot. Beam alignment is crucial- the imaging and bleaching beam must coincide. Most microscopes have an internal tube lens causing the laser beam to diverge. A diverging beam falling on the objective will focus the light on a different plane than intended. Hence we have used two lenses as a beam expander, which along with the internal lens, help collimate the laser beam until the beam reaches the objective completely parallel (**Figure 2.5**).

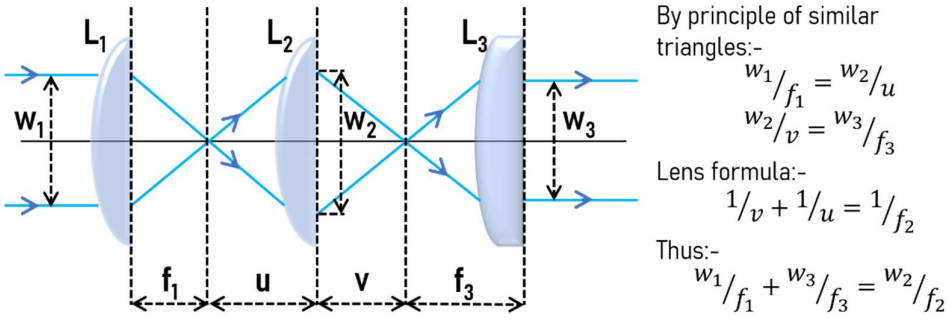

Figure 2. 5: Incident laser beam collimation using two external lenses (L_1, L_2) and the internal tube lens (L_3) of the microscope.

Finding f_3 is tricky. One has to pass the external laser beam through the lens system (L_1, L_2, L_3) and let the beam come out of the microscope turret through a port not containing an objective. One must then check if the emergent beam is parallel or adjust the two external lenses (L_1, L_2) until the emergent beam is parallel. Then, measuring w_3 can give f_3. One may further adjust the external lenses to achieve any possible w_3.

Before starting any FRAP experiment, one must ensure that

1. The imaging beam and bleaching beam coincide laterally (XY-alignment)
2. The focal plane of bleaching coincides with the plane where the light from the lamp gets focussed (Z-alignment)

One of the ways to verify these two conditions is to use fixed cells with a fluorescent cytoplasm. No recovery will occur upon photobleaching in 4% PFA (paraformaldehyde) fixed cells. For the 488nm laser, we can use fixed cells expressing EGFP in the cytoplasm. To verify whether the imaging and bleaching beam coincide (**Figure 2.6**), we can take an image of the cell with the spot illuminated by the imaging beam (**Figure 2.6-1**). Then, we can photobleach the spot and take an image of the whole cell with the fluorescent lamp (**Figure 2.6-2**). Lastly, upon merging the two images, one can verify if the two spots coincide or not (**Figure 2.6-3**).

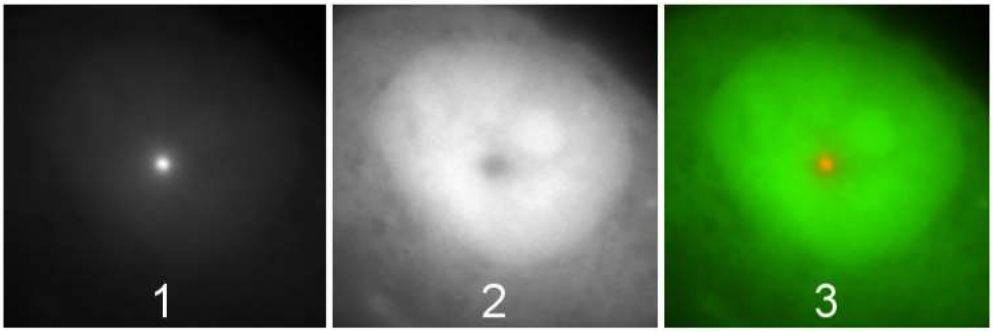

Figure 2. 6: Lateral (XY) alignment of the imaging and bleaching spots

After ensuring the lateral alignment, we verify if the bleaching beam is focussed vertically at the actual focal plane. One can photobleach a fixed cell after focussing anywhere in the cell's vertically middle region, and acquiring a Z-stack of the whole cell gives the 3D profile of the bleaching volume (**Figure 2.7**).

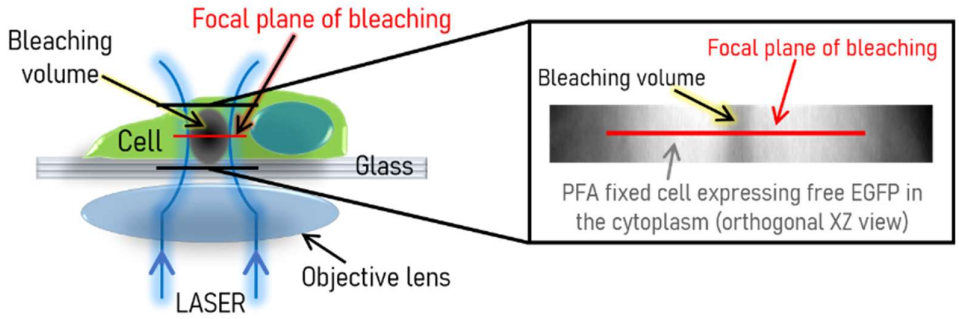

Figure 2. 7: Left- "waist" of the laser and the bleaching volume. Right- 3D bleaching profile of a fixed NIH/3T3 fibroblast cytosolic EGFP (XZ view)

The focal plane of bleaching (red) should be at the thinnest part of the "waist", which one can verify after inspecting the 3D Z-stack. The position of the bleaching plane is also a test of the parallelity of the incoming laser beam after rectification with the two external lenses. Only a parallel beam will focus on the actual focal plane of the objective, coincident with the focal plane of the fluorescent lamp.

After setting up the FRAP optics, one should check whether the imaging beam contributes to significant photobleaching. To check for photobleaching, we can again use the fixed fluorescent cells, and this time, by taking a time-lapse of the cell with just the imaging beam illuminating the cell. As there are no mobile fluorophores in fixed cells, the intensity profile of the spot from the time-lapse video reveals the level of photobleaching. Using ND filters to reduce the imaging beam's intensity circumvents the imaging beam's excess photobleaching.

2.1.2. Extracting diffusion rates from FRAP data

The diffusion rate (D) is analytically determinable for a diffusion-driven fluorescence recovery by fitting the recovery curve to a system-specific model. Assuming that the bleaching beam has a Gaussian profile, the diffusion rate D for a 2D system is given by-

$$D = \frac{\omega^2}{4\tau_D} \quad \text{... xiv}$$

where ω refers to the bleaching beam's radius and τ_D refers to the characteristic diffusion time obtained from the fitting parameters of the recovery curve.

The most straightforward way to extract τ_D is to fit the intensity recovery part $I(t)$ of the data to an exponential recovery function-

$$I(t) = A(1 - e^{t/\tau_D}) \quad \text{... xv}$$

Here, A is a measure of the mobile fraction of the fluorophores in the sample. For multiple timescales of diffusion, one can use-

$$I(t) = A\left(1 - e^{t/\tau_{D,1}}\right) + B\left(1 - e^{t/\tau_{D,2}}\right) + \cdots \quad \text{... xvi}$$

However, Equation $\boldsymbol{xv}$ or $\boldsymbol{xvi}$ does not account for the bleaching depth or the actual bleaching area. Multiple articles describe various fitting functions suitable for different situations and systems, and discuss ways to account for the bleaching depth and area artifacts [119–121]. For our studies, we chose the fitting function given by Minchul Kang [120] as it was optimal for FRAP experiments for fast diffusing proteins in the cytoplasm. The function

accounts for the increase in the bleaching area and the bleaching depth. FRAP data analysis was done using custom codes written in MatLab.

2.1.3. Calibration of the Point-FRAP setup

The easiest way to check if the FRAP setup works is to measure the diffusion rate of any free, non-binding fluorescent molecule in solutions of different viscosities (fluorescein, rhodamine, reconstituted EGFP). Using a variable glycerol-buffer mix, one can fine-tune the viscosity of the solution, simultaneously testing the sensitivity of the setup to changes in solution viscosity (**Figure 2.8**). One must account for the bleaching depth for fast diffusing fluorophores like fluorescein in water. Ignoring the bleaching depth and improper normalization of intensity recovery may lead to underestimation of the diffusion rate of the fluorescent probe.

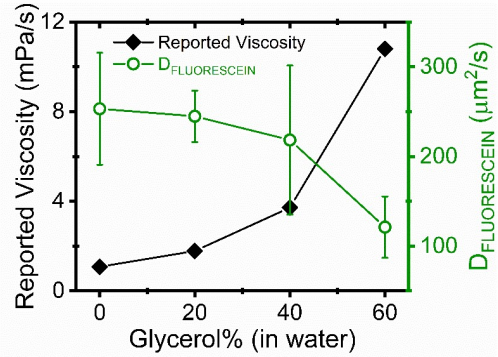

Figure 2. 8: Calibration of the Point-FRAP setup:- measuring the diffusion rate of fluorescein in different glycerol/water solutions at 25°C compared with reported viscosity coefficients of the same solutions

2.1.4. Drawbacks of FRAP

- The diffusion of fluorophores in and out of the bleaching region during a finite photobleaching time results in underestimating the diffusion rate.
- Longer exposure time for a good signal/noise ratio leads to a slower image acquisition rate, thus ignoring sub-millisecond diffusive recovery.

- The shape of the bleaching volume affects the recovery of fluorophores in 3D systems, like the cytoplasm. FRAP is best suited for 2D or vertically thin systems like the plasma membrane, as we effectively view a 2D recovery, and fluorophores in 2D systems move only laterally. For 3D systems, it is best if the bleaching volume is geometrically a vertical cylinder, as this creates an approximate 2D system where the observed recovery is contributed by lateral diffusion only.

FRAP is highly reliable for studying the translational diffusion of slow-moving molecules in 2D systems, like membrane proteins. Numerous mathematical models are available that describe both diffusion and association kinetics of proteins in 2D systems. For 3D systems, the diffusion rates measured by FRAP are not as accurate as other techniques like FCS (Fluorescence Correlation Spectroscopy). However, FRAP works reliably well for comparing two species having different diffusivity.

2.1.5. Point-FRAP in live cells

2.1.5.1 Measuring the translational diffusion rate of cytoplasmic and nuclear EGFP

The cytoplasm and the nucleus are the two major compartments of a cell with different architecture and molecular content. Monomeric EGFP (mEGFP) diffuses freely within both compartments. With point FRAP, we try to estimate if EGFP exhibits different rates of translational mobility in the cytoplasm and nucleus. The montage in **Figure 2.9-A** shows an NIH/3T3 fibroblast expressing free EGFP, and the graph in **Figure 2.9-B** depicts the average diffusion rate of EGFP measured in the cytoplasm and nucleus.

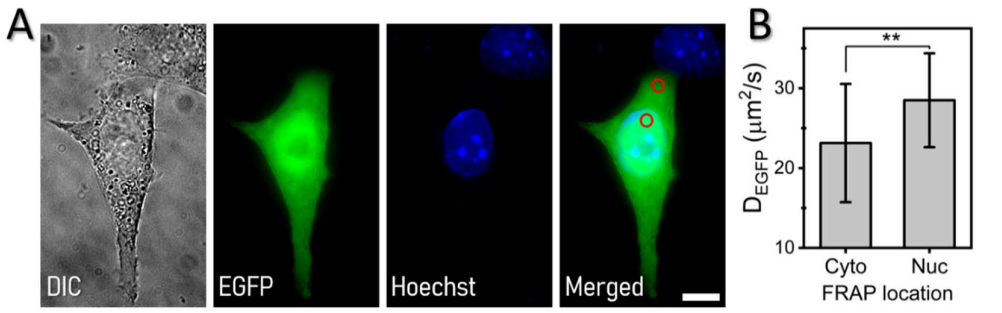

Figure 2. 9: (**A**) Montage depicting an NIH/3T3 fibroblast stably expressing monomeric EGFP (mEGFP) and Hoechst-stained nuclei. The red circles (diameter=2μm) in the merged image depicts the locations of photobleaching for studying FRAP. Scale bar=10μm. (**B**) Quantification of the average diffusion rate of EGFP in the cytoplasm and nucleus measured in 32 cells.

2.1.5.2 Measuring the translational diffusion rate of actin-mEGFP at the basal and mid planes of RAW 264.7 macrophages

Actin filaments are the most abundant of all cytoskeletal elements of the cell. Intracellular actin primarily exists in two forms, globular actin, or G-actin, and filamentous actin, or F-actin. Actin plays a significant role in cells' mechanical rigidity and mechano-transduction, including cell motility, migration, spreading, and proliferation. Actin filaments undergo continuous depolymerization and polymerization, contributing to cell motility and traction stress. In cells growing on two-dimensional, stiff substrates, the actin filament architecture varies at the cell's different vertical regions– the basal, mid, and apical planes. At each of these planes of a cell, filaments have different roles to play. The basal plane has focal adhesions and a dense network of stress fibers that regulate cell migration, spreading, and traction forces. In the mid and apical planes, the actin filaments play different roles, such as mechanical support, intracellular transport, and contractile stress on the cortex. FRAP can be utilized to study whether there is a measurable change in the mobility of actin at the different vertical planes of the cell. **Figure 2.10-A** highlights the structure of actin networks in RAW 264.7 macrophages transiently expressing actin-mEGFP in the basal plane (**Figure 2.10-A-i**) and the midplane (**Figure 2.10-A-ii**). The difference in the

diffusion rates of actin-mEGFP in the basal and mid planes estimated by FRAP is negligible (**Figure 2.10-B**), but the mobile fraction of actin-mEGFP is significantly different in the two planes. Thus we can conclude that actin-mEGFP does not have an observable difference in their diffusivity at different cell heights. However, there is a visibly different fraction of the bound and free population of actin-mEGFP at the different vertical planes of RAW 264.7 macrophages. Expectedly, free mEGFP shows no difference in either quantity measured at the different planes of RAW 264.7 cells.

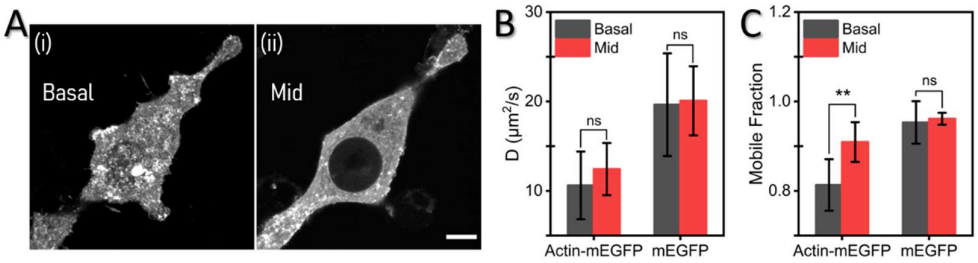

Figure 2. 10: (**A**) Basal (**i**) and mid (**ii**) plane of a RAW 264.7 cell expressing actin-mEGFP. Scale bar= 5μm. (**B**) Quantification of diffusion rate in the basal and mid planes for actin-mEGFP and free EGFP. (**C**) Mobile fraction of actin-mEGFP and free EGFP in the basal and mid planes.

2.2. Fluorescence Anisotropy Imaging Microscopy (FAIM)

A fluorophore can absorb photons of appropriate wavelengths in the timescale of femtoseconds. The electrons shift to a higher energy state upon excitation, and then vibrational relaxations pull them down to a slightly lower metastable state in the timescales of picoseconds. Further, the electrons return to the ground state in a few nanoseconds upon releasing longer wavelength photons. Hence, the net fluorescence lifetime of a fluorophore amounts to a few nanoseconds.

If a fluorophore is being excited by plane-polarized light, the probability of excitation depends on $\cos^2\theta$ if θ is the angle subtended by the fluorophore's absorption dipole moment on the excitation light's plane of polarization. The light emitted by the fluorophore upon de-excitation is also plane-polarized, oriented in the plane of its emission dipole moment. If the fluorophore is undergoing Brownian motion in a fluid medium, then a few nanoseconds would have passed between the time it absorbs the plane-polarized photons and emits its own photons. Hence, the fluorophore would not be as similarly oriented as it was while absorbing the photons. The resultant emission would be polarized at a different angle, and the magnitude of the angle will be determined by the extent of the fluorophore's rotation away from the excitation plane.

Upon examining the emitted light of an ensemble of such fluorophores by mutually orthogonal polarizers (analyzers), one could find a difference in the number of photons passing through the parallel and perpendicular polarizers. Hence, using this method, one could estimate how much a fluorophore rotates in a fluid medium. Fluorescence Anisotropy utilizes this principle to monitor any fluorescent molecule's rotational dynamics (**Figure 2.11**).

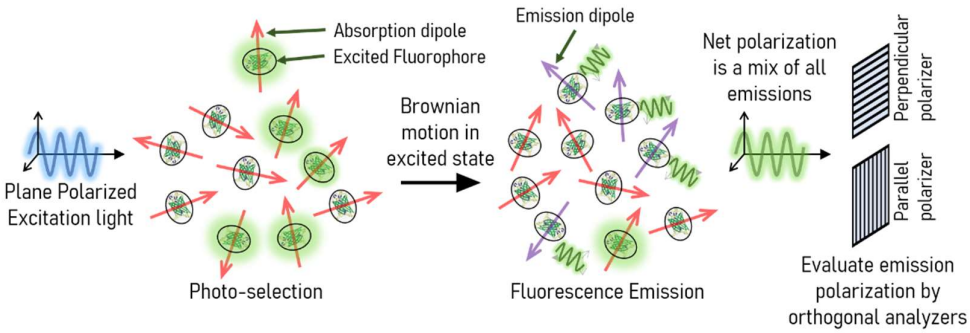

Figure 2. 11: The principle of Fluorescence Anisotropy

Details of fluorescence anisotropy are well illustrated in "Principles of Fluorescence Spectroscopy" by Joseph R. Lakowicz (chapters 10-12) [122], which talks about the theoretical background as well as the experimental

principles and methodology. Another good read is “Introduction to Fluorescence” by David M. Jameson (chapter 5)[123,124].

2.2.1. Time-resolved and steady-state Fluorescence Anisotropy

The principle of fluorescence anisotropy illustrated above is implemented using a picosecond laser that excites an ensemble of fluorophores for the briefest time. The technique is called time-resolved fluorescence anisotropy. The excited fluorophores gradually lose their energy by fluorescence emission, whose intensity decreases exponentially (**Figure 2.12**).

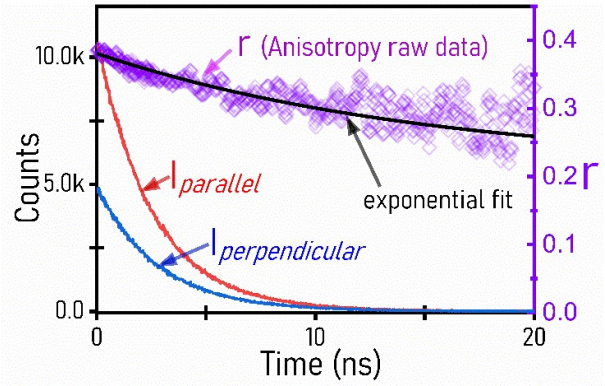

Figure 2. 12: Typical Time-resolved fluorescence anisotropy data.Red line- photon count (intensity) of the parallel channel. Blue line- intensity observed in the perpendicular channel. Violet diamonds- anisotropy values calculated from the raw data. Black line- fitted curve to the raw anisotropy data.

The fluorescence is observed through a set of mutually orthogonal polarizers, and fluorescence anisotropy (r) is computed from the normalized difference between the parallel and perpendicular channels’ intensities using the formula-

$$r = \frac{I_{parallel} - gI_{perpendicular}}{I_{parallel} + 2gI_{perpendicular}} \quad \ldots xvii$$

Here, g refers to an instrumental grating factor that accounts for differences in the optical transmission efficiency of the polarizers. The denominator in Equation- $\boldsymbol{xvii}$ represents the total intensity of emission by the fluorophore

if all the emitted light could be collected. However, the instrumental geometry allows the measurement of emission polarization in only two directions: one parallel to the orientation of the excitation light and another along one of the perpendicular directions to the orientation of the excitation light. As the contributions of fluorescence emission to the perpendicular directions are equal for an electric dipole (the fluorophore), we can safely double the intensity value in the perpendicular channel for our total intensity estimation.

Steady-State Fluorescence Anisotropy refers to anisotropy measurements when the excitation is continuous and not mediated by a pulsed laser beam. The steady-state measurements are merely time-averaged measurements of time-resolved fluorescence anisotropy. Steady-state measurement only reflects the value of the time-resolved anisotropy after the exponential decay is complete and the anisotropy values have reached a steady-state (**Figure 2.12**). To set up Steady-State Fluorescence Anisotropy on a microscope, one can simply make the excitation light plane-polarized with a linear polarizer and add a polarizing beam splitter in the emission path to divide the image into the “parallel” and “perpendicular” channels, as explained in **Figure 2.13**.

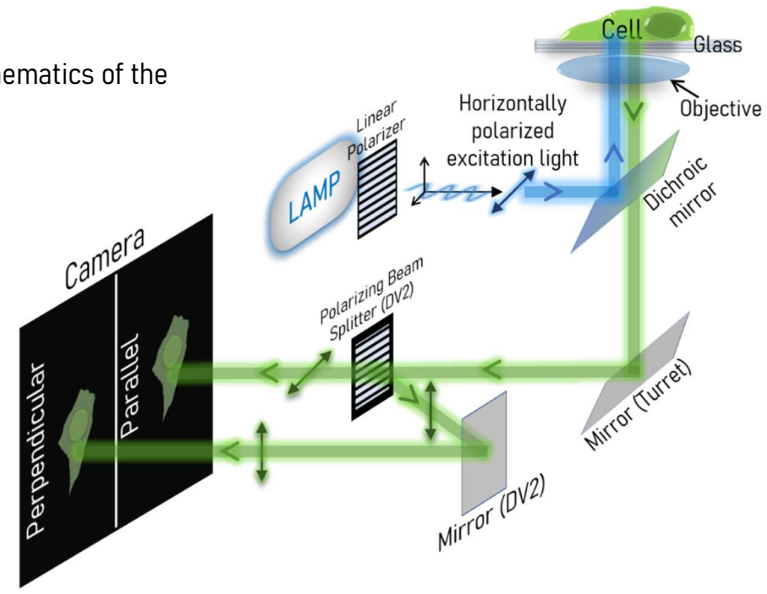

Figure 2. 13: Schematics of the FAIM set up

The above schematic describes the simultaneous acquisition of both parallel and perpendicular channels. One can use a linear polarizer instead of the polarizing beam splitter and rotate the polarizer at 90 degrees to obtain the same image in the parallel and perpendicular emission modes sequentially [125]. However, this method may be too slow if the fluorophore-tagged objects of interest have fast intracellular dynamics that reorient within the time the emission polarizer is rotated. While simultaneously acquiring the two channels overcomes this problem, the method still has its issues. The optics used to focus the image on the camera chip may distort the parallel and perpendicular channels differently, and then the images obtained in the two halves of the chip must be registered accurately.

Another important factor regarding FAIM image analysis is background correction. Ideally, the average intensity of a cell-free space in the image can be considered as background. The same region must be considered for both channels, and the respective averages must be subtracted from each channel for proper background correction. To get the correct g-factor for each pixel, one can take a solution containing a fluorophore whose fluorescence anisotropy would be zero (for example, fluorescein in water). After image registration, anisotropy can be calculated using the formula in Equation- $\boldsymbol{xvii}$ using the pixel values of the parallel and perpendicular channels. Custom-written macros in Fiji (ImageJ) were used for such analysis. The horizontal excitation polarization was chosen for the above setup to minimize the reflection-mediated polarization losses (Brewster's law).

2.2.2. Physical parameters affecting fluorescence anisotropy

The measured fluorescence anisotropy (r) depends on the fluorescence lifetime (τ), the fluorophore's rotational correlation time (θ_C), and the intrinsic anisotropy (r_0) of the fluorophore. The fluorophore's rotational correlation time, that is, the average time a molecule takes to rotate through 1 radian,

is dependent on the volume of the molecule (V), the solution viscosity (η), and the solution temperature (T). The intrinsic anisotropy of a fluorophore corresponds to the measured anisotropy if the molecule does not rotate (hence no decay is observed, as in **Figure 2.12**) and is a function of the photophysical properties of the molecule itself. The celebrated Perrin equation describes the relationship between these parameters in-

$$r = \frac{r_0}{1 + {}^{\tau}/_{\theta_C}} \qquad \text{... xviii}$$

$$\theta_C = {}^{\eta V}/_{k_B T} \qquad \text{... xix}$$

The above equations imply that a change in the θ_C of the fluorophore (through an increase in V or η) can affect the value of r, showing how fluorescence anisotropy measurements can be used to study the rotational properties of molecules.

However, if $\theta_C \gg \tau$, the ${}^{\tau}/_{\theta_C}$ ratio is significantly less than 1, and the measured r is almost independent of rotation. Fluorescent proteins with large V and relatively short τ exhibit this property (**Figure 2.14**).

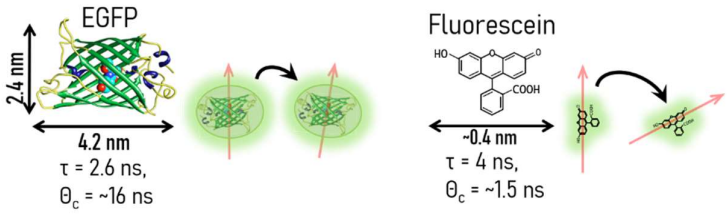

Figure 2. 14: Comparison of the Enhanced Green Fluorescent Protein (EGFP) with Fluorescein. ${}^{\tau}/_{\theta_C}$ for EGFP is ~0.16 while for Fluorescein it is ~2.6

EGFP rotates much slower than fluorescein in the excited state, making anisotropy measurements of EGFP practically insensitive to its rotational motion. Hence, EGFP is not sensitive to changes in solution viscosity. However, fluorescein is highly sensitive to viscosity as resistance to its rotational motion can significantly affect the anisotropy measurements.

FRET between the same fluorophores, or homo-FRET, is another physical parameter affecting fluorescence anisotropy measurements. Homo-FRET usually occurs when the average intermolecular distance between the fluorophores is small, and there is a significant spectral overlap between the excitation-emission bands of the fluorophore. The average intermolecular distance between fluorophores in highly concentrated solutions is low enough to exhibit homo-FRET (**Figure 2.15**).

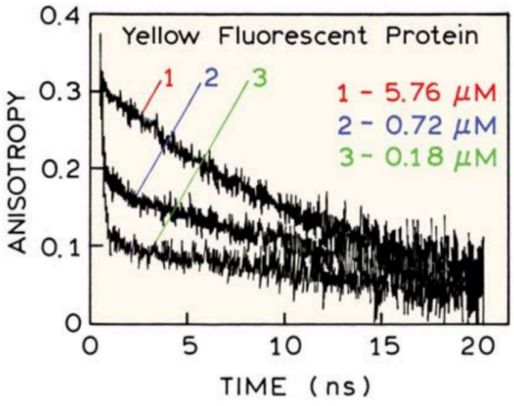

Figure 2. 15: Time-resolved anisotropy decays of YFP at three different concentrations show homo-FRET levels increasing with fluorophore concentration. Adapted [122].

The energy transfer rate (k_{hFRET}) between two fluorophores separated by a distance r is determined by-

$$k_{hFRET} = {}^{1}/_{\tau}\left({}^{R_0}/_{r}\right)^{6} \qquad \text{... xx}$$

Where R_0 is called the Förster distance and is dependent on the fluorophore's spectral overlap integral- $J(\lambda)$, quantum yield- Q_D, the relative orientation factor- κ, and the refractive index of the solution- n. For λ in cm units and $J(\lambda)$ in cm^3/M units, R_0 (in $\dot{A}$) is expressed as-

$$R_0 = 9780 \times \left(\frac{\kappa^2 Q_D J(\lambda)}{n^4}\right)^{1/6} \qquad \text{... xxi}$$

Homo-FRET efficiency (E_{hFRET}) becomes 50% when $r = R_0$ as E_{hFRET} is defined as-

$$E_{hFRET} = \frac{k_{hFRE}}{k_{hFRET} + {}^{1}/_{\tau}} \quad \ldots xxii$$

Simplistically, one can visualize the effect of homo-FRET on measured anisotropy between two identical fluorophores when the two fluorophores are located at a distance r such that $r \sim R_0$ but oriented at different angles. If one of the fluorophores (say, A) is more aligned with plane-polarized excitation light, then its photo-excitation could transfer the excitation energy to its neighboring, un-excited fluorophore (say, B). Now, the plane of fluorescence emission from B would be shifted away from the plane of excitation by a greater magnitude than the plane of emission by A, if A had emitted instead of B. Thus, the resultant emission is more depolarized, and the value of the measured fluorescence anisotropy is lesser than expected (**Figure 2.16**).

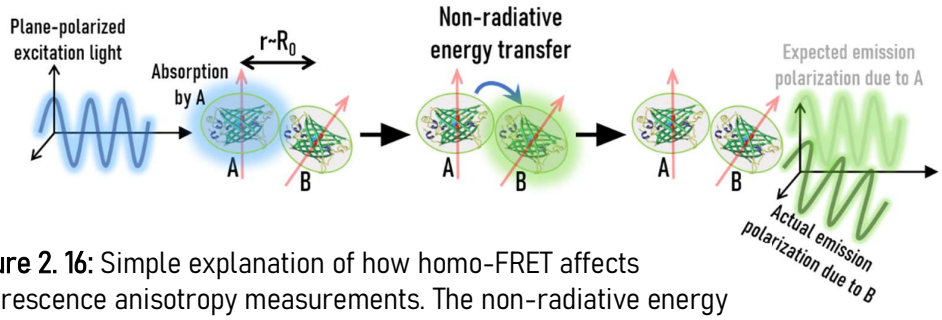

Figure 2. 16: Simple explanation of how homo-FRET affects fluorescence anisotropy measurements. The non-radiative energy transfer from A to B makes the resultant emission come from B and not A. Hence the resultant emission is more depolarized and the value of the measured anisotropy decreases

Another factor that can depolarize fluorescence emission is scattering by the medium containing the fluorophores. Biological objects like membranous organelles have a relatively high refractive index and are prominent scatterers notorious for affecting intracellular fluorescence anisotropy measurements.

2.2.3. Steady-State FAIM in live cells

2.2.3.1 Estimating the contractile stress on actin filaments in NIH/3T3 fibroblasts using FAIM

Actin filaments having alternating polarities are crosslinked by proteins like α-actinin to create stress fibers, which are usually connected to focal adhesions. Non-muscle myosin II proteins are one of the molecular motors widely prevalent in stress fibers and produce tensile forces along the length of an actin filament upon actuation by ATP. Stress fibers have a vital role in wound healing. Fibroblasts along the periphery of a wound differentiate into myofibroblasts, which use the actomyosin machinery in stress fibers to generate contractile forces through focal adhesions to mediate wound closure [126,127]. The actin cytoskeleton also generates the necessary mechanical forces for epithelial cell migration to the wound site [128]. We asked whether mechanical forces cause a change in the conformation of actin filaments, like buckling under compression or extending under tension. As the intra-molecular separation distance between each monomer of a filament is in the nanometer range, which is well below the diffraction limit of optical microscopes, one cannot directly observe the bending or lengthening of actin filaments using standard fluorescence microscopy. Homo-FRET between fluorophores attached to actin monomers in the filament could serve as a potential metric of conformational changes in actin filaments (**Figure 2.17**).

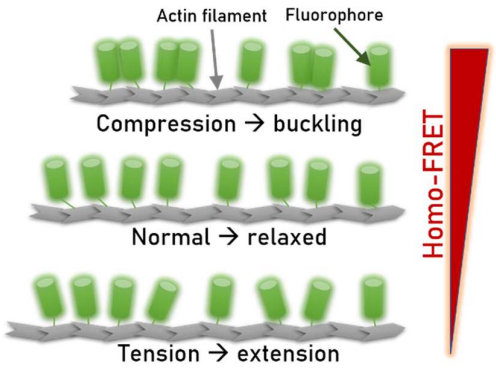

Figure 2. 17: Principle of using Homo-FRET to gauge tension in actin filaments

Under compression, the fluorophores attached to actin filaments come closer, and homo-FRET levels increase, while tension causes the filaments to extend and a decrease in homo-FRET levels due to the increase in intra-fluorophore distances. As for the fluorophores, a fluorophore-tagged cytosolic protein that selectively binds to actin filaments (like LifeAct-EGFP) or genetically encoded fluorophore-tagged actin (like actin-EGFP) can serve as probes to measure homo-FRET.

To visualize homo-FRET in actin filaments, we transfected NIH/3T3 fibroblasts with LifeAct-EGFP and performed FAIM (**Figure 2.18-A**). Photobleaching increases the effective intra-fluorophore distance by virtually "turning off" the fluorescence randomly (**Figure 2.18-B**), thus reducing homo-FRET.

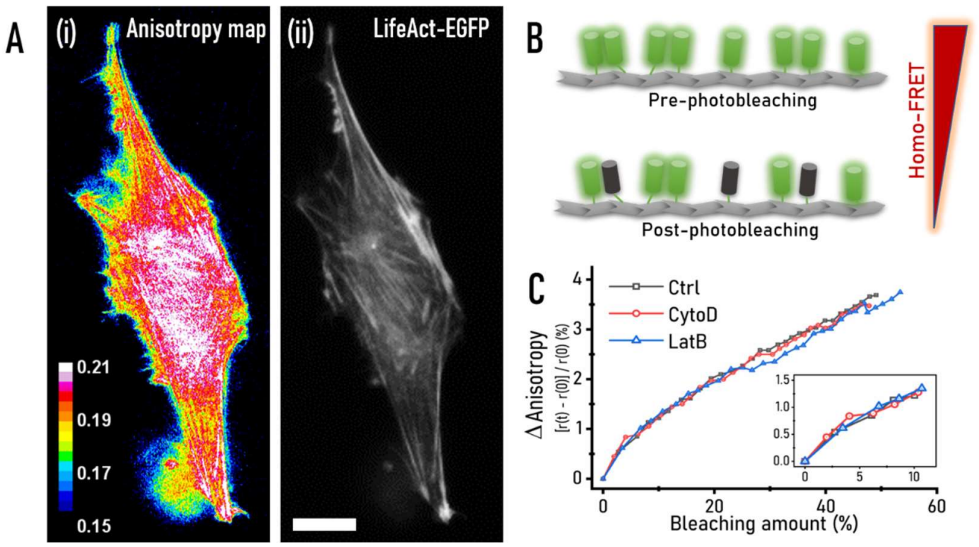

Figure 2. 18: (**A**) Representative anisotropy map (with color bar representing anisotropy values) of a NIH/3T3 cell expressing LifeAct GFP in (**i**) and its corresponding intensity in (**ii**). Scale bar= 10µm. (**B**) Concept of photobleaching to prove the presence of homo-FRET. (**C**) Plot of %change in anisotropy upon photobleaching NIH/3T3-LifeAct GFP cells without actin filament disruption (Ctrl, gray) and with disruption (CytoD- 2µM,1h; LatB- 1µM, 1h). Inset zooms-in on the 10% bleaching activity of the same graph. Photobleaching experiments were performed on >40 cells in each case.

Further, upon actin filament disruption, the homo-FRET between LifeAct-EGFP bound to actin should be abolished, and thus the change in anisotropy upon photobleaching should have a different rate (**Figure 2.18-C**). Contrary to our expectations, the rate of homo-FRET was identical irrespective of the conformation of the filamentous actin. Some NIH/3T3-LifeAct EGFP cells with highly intense stress fibers (indicating high concentrations of fluorophores) had a lower anisotropy than the neighboring areas, signifying homo-FRET in those regions. However, on average, **Figure 2.18-C** depicts that most actin filaments do not exhibit any homo-FRET between LifeAct-EGFP molecules.

2.2.3.2 Perturbing the contractile stress in actin filaments pharmacologically and mechanically

We hypothesized that if the binding-unbinding rate of LifeAct is faster than the imaging speed, photobleached LifeAct-EGFP molecules could dissociate from actin filaments and diffuse away before another image of the cell can be captured post photobleaching. Hence we get similar rates of anisotropy increase even if the cell contains comparatively fewer numbers of filamentous actin. However, changing tension in the actin filaments would be longer-lasting and could show a visible rise in anisotropy due to loss of homo-FRET. Hence, we proceeded to perturb the tension in the filamentous actin by inhibiting myosin II activity with the drug blebbistatin and disrupting focal adhesions using trypsin/EDTA to see if homo-FRET levels could be affected (**Figure 2.19**). Blebbistatin hinders the ATPase activity of myosin II, relaxing actomyosin contractility and reducing tension on the actin filaments (**Figure 2.19-A**). Although the average anisotropy per cell does not rise significantly, a local increase in anisotropy is noticeable in blebbistatin-treated NIH/3T3-LifeAct EGFP (**Figure 2.19-B**). Focal adhesion disruption also reduces tension in the stress fibers by cutting down the tether points, and a concurrent rise in the average anisotropy is visible in all cells (**Figure 2.19-C**). However, the rise in anisotropy values upon trypsin treatment cannot be attributed to loss of homo-FRET in the actin filaments but to

another interesting intracellular phenomenon- Macromolecular Crowding (MMC). The effects of MMC on fluorescence anisotropy will be discussed in the subsequent chapters.

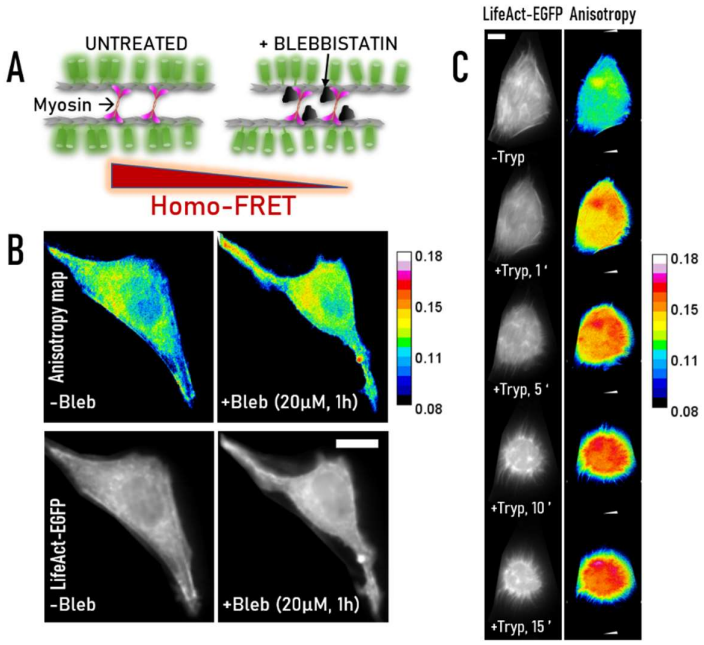

Figure 2. 19: (**A**) Schematic of Blebbistatin treatment affecting homo-FRET through mechanical relaxation. (**B**) Representative NIH/3T3-LifeAct EGFP treated with Blebbistatin shows increase in local anisotropy. Scale bar= 10µm. (**C**) Focal adhesion disruption by trypsin treatment leads to visible increase in overall anisotropy values of NIH/3T3-LifeAct EGFP, as evident from the representative cell. Scale bar= 10µm.

2.2.3.3 FAIM in biological tissue- Salivary gland of Drosophila melanogaster

FAIM can also be performed on transparent biological tissues if the microscope objective's working distance permits a full range of view through the tissue's thickness. **Figure 2.20** shows the salivary gland of a fruit fly (*Drosophila melanogaster)* larva expressing Actin-GAL4-UAS-GFP being poked by a glass capillary needle to create a wound. Within 5 min of poking, the neighboring regions around the wound start showing higher anisotropy of actin GFP, indicating a substantial change in the conformation of the actin filaments. The cause of the visible change in anisotropy is still speculative and requires further studies.

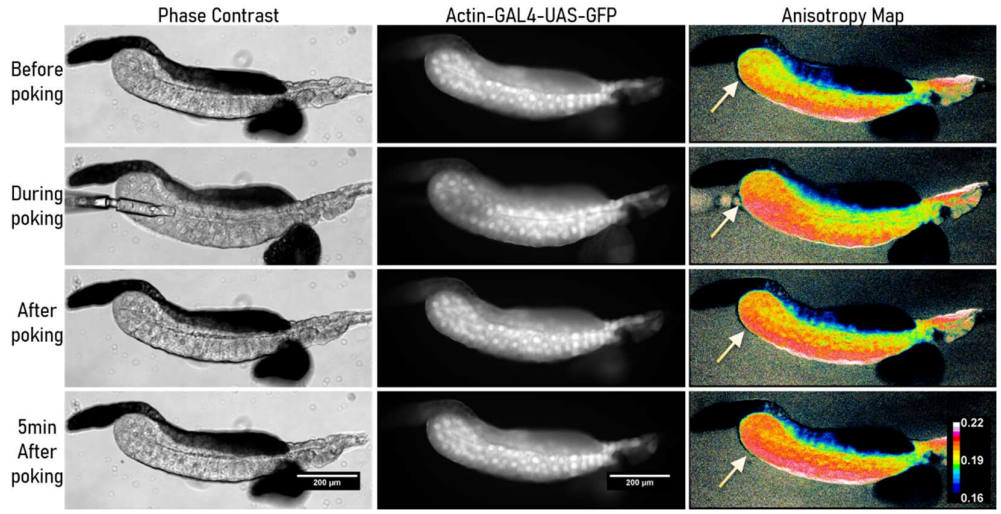

Figure 2. 20: The salivary gland imaged through 10x objective shows a net increase in anisotropy of actin GFP around the regions (indicated by arrows) that experienced mechanical stress due to poking by the glass needle. Scale bars indicate 200 µm.

2.3. Particle Tracking Microrheology (PTM)

The cytoplasm is usually imagined as a viscous fluid enclosed within a thin membrane. The dense cytoskeletal network in nucleated eukaryotic cells alters the cytoplasmic fluid's mechanical properties and transforms it into a hydrogel. Thus, the microrheological nature of the cytoplasm is both viscous and elastic, that is, viscoelastic. The effect of cytoplasmic viscoelasticity also depends on the probe's size used to measure the viscoelasticity. A probe smaller than the average pore size of the cytoskeletal mesh experiences more viscosity, while a probe comparable to or larger than the average pore size experiences the elastic nature of the hydrogel more than the viscous nature. The viscoelastic nature of the cytoplasm can be mechanically modeled by a combination of spring-dashpot systems (**Figure 2.21**).

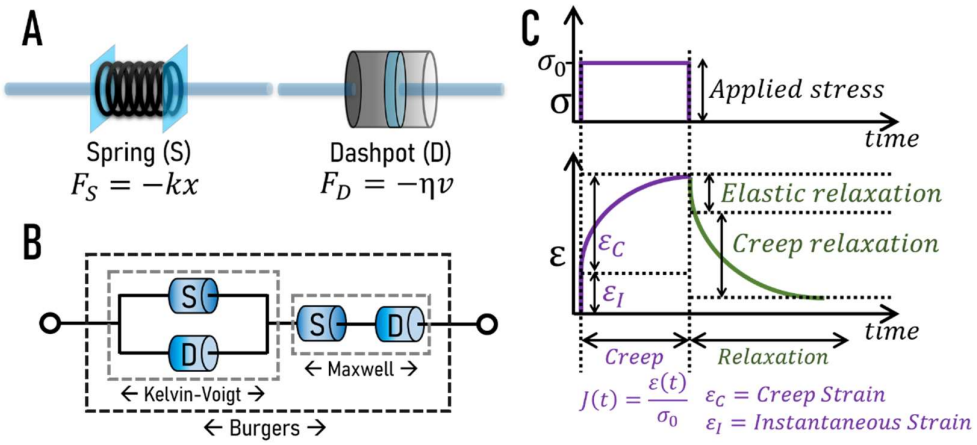

Figure 2. 21: Schematic representation of the spring-dashpot systems to model viscoelasticity. (**A**) Description of a spring which exerts a force (F_S) proportional to the displacement (x) and spring constant (k), and a dashpot which exerts a resistive force (F_D) proportional to the velocity (v) of the object and the viscosity (η) of the fluid. (**B**) One type of the Burgers model which combines the Kelvin-Voigt and Maxwell models to describe viscoelasticity. (**C**) Creep relaxation behavior of viscoelastic materials under stress (σ). In cells, the cytoskeletal organization typically determines the viscoelastic properties of the cytoplasm. While single cytoskeletal polymers are typically elastic, the mesh-like network structures coupled with the protein-rich cytosol add the viscous effect to the cytoplasm, ultimately making the cytoplasm viscoelastic in nature.

Micrometer-sized polystyrene beads coated with a fluorescent molecule can be ballistically injected into the cell, and tracking their motion can be used to probe the viscoelastic properties of the cytoplasm. The technique is termed Particle Tracking Microrheology (PTM). The Brownian motion of the probe can be tracked in response to the intracellular thermal forces, that is- Passive PTM, or the motion of the probe in response to a known external force can be quantified and compared to the creep-relaxation as described in **Figure 2.21-B**, that is- Active PTM. The external forces can be applied optically on fluorescent beads through Optical Tweezers, or if the bead has a magnetic core, a magnetic field can be used to generate forces on the beads using Magnetic Tweezers.

2.3.1. Passive Particle Tracking Microrheology

The Brownian motion of micrometer-sized tracer particles suspended in a hydrogel reflects the hydrogel's rheological nature. If the particle were suspended in a fluid, the mean-squared displacement (MSD) of the particle plotted against the lag time (τ) would be related to the particle's diffusion rate (D) in the fluid as $MSD(\tau) = 4D\tau$ (in 2D). If the particle were attached to an elastic substrate, then $MSD(\tau) = Constant$. However, as the intracellular environment is viscoelastic, the MSD of the particle of radius R would be related to the hydrogel's viscoelastic modulus (G^*) according to -

$$G^*(s) = \frac{k_B T}{\pi R \mathcal{L}\{MSD(s)\}s}$$

... xxiii

Here, T is the hydrogel's temperature, and $\mathcal{L}\{MSD(s)\}$ is the Laplace transform of the MSD for a Laplace frequency $s \propto {}^{1}/_{\tau}$. The viscoelastic modulus can be broken down into the elastic (G') and viscous (G'') components as- $G^* = G' + iG''$. The MSD of such a tracer particle with trajectory (x_t, y_t) is given by-

$$MSD(\tau) = \langle (x_{t+\tau} - x_t)^2 + (y_{t+\tau} - y_t)^2 \rangle$$

... xxiv

For our experiments, fluorescent polystyrene beads of diameter 200 nm (Invitrogen, #F8888) are ballistically injected into the cell with the Helios Gene Gun (BioRad) delivery system. The beads are tracked at 100 frames per second with a 63x oil immersion objective to capture the beads' thermal motion. Cells are "shot" with a pressure of 100 PSI from a distance of 3-4 cm from the petridish. Cells are gently washed with serum-free media thrice to remove beads stuck on the plasma membrane or glass. Then the cells are incubated in phenol red-free DMEM at 37℃, 5%CO_2 for 1 h to allow them to recuperate (**Figure 2.22-A, B-i**). The trajectories of the fluorescent beads are extracted using the Mosaic plugin (Particle Tracking 2D/3D) of ImageJ

(**Figure 2.22-B-ii, B-iii**). MSD and viscoelastic moduli computation (**Figure 2.22-C**) was performed using a custom-written MATLAB code according to the work of Maxine Jonas [129].

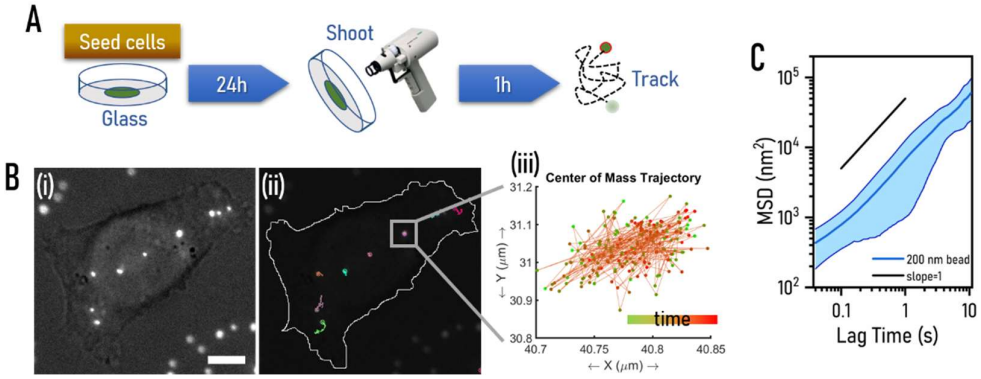

Figure 2. 22: (**A**) Schematic of sample preparation for passive particle tracking microrheology. Cells seeded on glass-bottom petridishes for 24 hours are shot by the Gene Gun with 200 nm tracer beads and allowed to recover for 1 hour. Then the injected beads are tracked. (**B**) (**i**)An NIH/3T3 cell ballistically injected with 200 nm fluorescent beads imaged with both brightfield and 488/510 fluorescence channel. Scale bar = 15 µm (**ii**) The same cell with the bead trajectories overlaid along with the cell's perimeter. (**iii**) The trajectory of the center of mass of one of the beads (white square in (**ii**)) plotted against time (dots coloured green to red). (**C**) Mean MSD (blue line) and standard deviation (blue fill) of the bead trajectories in **B-(ii)** compared to purely Brownian MSD with slope=1.

2.3.2. Active Particle Tracking Microrheology

We use a magnetic tweezer to simulate active PTM and probe the microrheological properties of cells. The sample preparation method is similar to passive PTM, except the tracer beads are larger in size, have a magnetic core, and are not necessarily fluorescent. For our experiments, 2.8 µm sized magnetic beads (Dynabeads, M280) are ballistically injected into cells. An electromagnet was designed with a soft iron core with a sharp, conical tip to increase the gradient of the magnetic field (**Figure 2.23-A-i, ii**). The coil of the electromagnet is made with .30 gauge insulated copper wire and has a resistance of 40 Ω. A current of 2 A through the coil can generate >50 pN of force on the 2.8 µm beads at a distance of ~100 µm. Pulses of

high current lasting ~1s are passed through the electromagnet coil to generate creep strain in the cells (**Figure 2.23-A-iii, iv**). The motion of the magnetic bead is tracked similarly to passive PTM, and the bead displacement vs. time gives the creep strain for the cell (**Figure 2.23-B**). The forces generated by the electromagnet were computed by suspending the 2.8 µm beads in a 50% glycerol solution, and further using the electromagnet to drag the beads through the glycerol solution enables us to equate the viscous drag on the beads (from their trajectories) with the local magnetic force using the relation- $F_{magnetic} = 6\pi\eta R v$ (**Figure 2.23-C**). Here, η is the viscous coefficient of the glycerol solution, R is the radius, and v is the velocity of a bead.

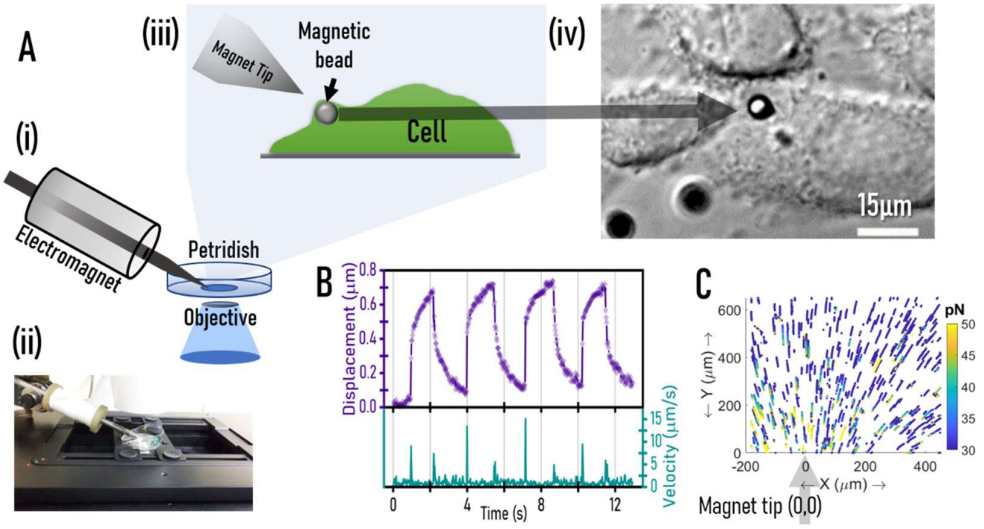

Figure 2. 23: (**A**) Description of a magnetic tweezer setup. (**i**) shows the schematic of the electromagnet and the cell in petridish. (**ii**) is the photograph of the setup. (**iii**) is the side view of a magnetic bead inside a cell being pulled by the magnetic tweezer. (**iv**) is the image of a magnetic bead inside an NIH/3T3 fibroblast. (**B**) shows the displacement and velocity of the magnetic bead in (**A-iv**) upon applying the magnetic pulses. (**C**) shows the force map obtained when 2.8 µm beads are dragged through 50% glycerol solution for a current of 2A at 20V.

Chapter 3: Steady-state Fluorescence Anisotropy of EGFP as a sensor for cytoplasmic macromolecular crowding

Since its discovery, the Enhanced Green Fluorescent Protein (EGFP) has been a handy and versatile tool for biologists to probe various aspects of cellular function. EGFP has high molecular brightness, efficient chromophore maturation, and good photostability. The chromophore of EGFP, located inside a beta-barrel composed of 11 antiparallely arranged beta-strands, is practically unaffected by fluctuations in the intracellular pH at physiological ranges [130–132]. Thus, using EGFP as a probe for quantitative measurements of intracellular processes is sensible in the photophysical context.

3.1. Theory

The intracellular environment is crowded with macromolecules, and the dense packing of macromolecules increases the refractive index of the cytoplasm. Hence, quantifying the refractive index could enable one to gauge the macromolecular crowding (MMC) level in the cytoplasm. The elevated cytoplasmic refractive index alters the fluorescence lifetime of EGFP from the values measured in salt buffers. The effect of refractive index (n) on the intrinsic fluorescence lifetime (τ_0) of EGFP can be understood from the Strickler-Berg equation [133]-

$$1/\tau_0 = 2.88 \times 10^{-9} n^2 \frac{\int I(\vartheta) d\vartheta}{\int I(\vartheta) \nu^{-3} d\vartheta} \int \frac{\varepsilon(\vartheta)}{\vartheta} d\vartheta$$

... XXV

Here, $I(\vartheta)$ and $\varepsilon(\vartheta)$ represents the fluorescence emission spectrum and the molar extinction coefficient of the molecule for a wavenumber ϑ. Thus essentially, $^1/_{\tau_0} \propto n^2$ when all other factors are preserved. The intrinsic fluorescence lifetime, τ_0, is defined as- $\tau_0 = {}^1/_{k_r}$, where k_r is the rate of radiative decay of the fluorophore's electronic excitation. τ_0 is different from the observed fluorescence lifetime, τ, where $\tau = \frac{1}{k_r + k_{nr}}$, with k_{nr} being the non-radiative decay rate. Hence, the effect of the solution refractive index on fluorescence photophysics is independent of the fluorophore's intersystem conversion rate or triplet transition rate [134]. Since the quantity k_r is affected, the solution refractive index has an additional effect on the transition dipole moment of the fluorophore [135].

Altering the MMC conditions changes the intracellular refractive index and, subsequently, the lifetime of EGFP. Now, since the Perrin equation for fluorescence anisotropy states that $r = \frac{r_0}{1 + {}^{\tau}/_{\theta_C}}$, therefore $r \propto {}^1/_{\tau_0} \propto n^2$. For EGFP, τ is ~2.6 ns [136] and θ_C is ~14 ns in water [137]. Thus, ${}^{\tau}/_{\theta_C}$ for EGFP is 0.19 in water. Increased MMC decreases τ and increases θ_C, thus increasing the value of r. Further, r_0 itself could also be affected by changes in n due to changes in the angle of the chromophore's transition dipole moment. Hence, fluorescence anisotropy of EGFP (r_{EGFP}) could be used to probe the cytoplasmic MMC. While direct fluorescence lifetime imaging microscopy has been used to study intracellular protein densities [138,139], we used Steady State FAIM, which requires less complicated instrumentation and has a higher throughput than measuring fluorescence lifetime with confocal microscope systems. We show that r_{EGFP} is a reliable probe for measuring intracellular MMC, one that has a high dynamic range, is virtually insensitive to intracellular pH, and can rapidly sense the changes in MMC conditions during various cellular processes.

3.2. r_{EGFP} as a probe for Macromolecular Crowding

3.2.1. r_{EGFP} is highly sensitive to protein concentrations

3.2.1.1 Purification and estimation of EGFP concentration by FCS

We purified EGFP from competent *E. Coli* using a Ni-NTA column protein purification method. First, we estimated the concentration of the purified EGFP using FCS (Fluorescence Correlation Spectroscopy). Through FCS, we can count the fluctuations in the fluorophore flux within the confocal volume of a microscope objective for a nanomolar-picomolar range of fluorophore concentrations in a liquid medium. Then, upon computing the autocorrelation of the fluctuations, one can estimate the concentration of the fluorophore in the solution. FCS measurements were performed in solutions diluted from our purified EGFP stock solution using a 40x/1.2NA water immersion objective on a confocal microscope (Zeiss LSM 780) at 20°C. EGFP was diluted from the stock at the indicated volume fractions in 100mM Hepes (pH 7.4), then 100 µL of each solution was sandwiched between glass coverslips with 1mm spacer sealed airtight and bubble-free. Fluorescence fluctuations were measured for 2 s at the height of 200 µm from the basal coverslip glass, and the averaged auto-correlation data of 500 repetitions was plotted for each solution (**Figure 3.1-A**). The autocorrelation curve $G(\tau)$ was fit by the built-in curve fitting system to the analytical function for 3D anomalous diffusion- $G(\tau) = 1 + \frac{1}{N}\frac{1-F+F_e^{-\tau/\tau_f}}{1-F}\frac{1}{1+(\frac{\tau}{\tau_D})^{\alpha}[(1+\frac{1}{S^2})(\frac{\tau}{\tau_D})^{\alpha}]^{1/2}}$, where N is the number of fluorophores in the confocal volume, τ is the lag time, F is the fraction of fluorophores in the triplet state, and S is the structure parameter ($S = {\omega_Z}/{\omega_{XY}}$; with ω_Z being the axial radius and ω_{XY} being the lateral radius). The value of the diffusion anomaly parameter, α, was fixed at 1 during curve fitting for simplicity. The triplet state fraction was not accounted for while fitting $G(\tau)$ of the EGFP

solutions. The number density of fluorophores in the confocal volume $N = 1/(G(0) - 1)$ is independent of fitting parameters. The theoretical values of ω_Z and ω_{XY} (for 488 nm light, 1.2NA objective, and 1.33 refractive index for Hepes buffer) is 901 nm and 248 nm, respectively. The ellipsoidal confocal volume (V) thus amounts to ~0.109 fL. Since $G(0)$ = 1.028 for the 0.1 dilution (10% v/v dilution), the concentration of EGFP can be calculated using $[EGFP] = \frac{N}{N_A}\frac{1}{V}$, which amounts to ~543 nM. Thus, our stock solution of purified EGFP has a concentration of ~5.4 μM. The EGFP solutions subjected to FCS measurements were then imaged with the FAIM setup to compare their total intensity readouts against known fluorophore concentrations (**Figure 3.1-A-inset**).

3.2.1.2 Fluorescence Anisotropy measurements of purified EGFP in crowded solutions

We then measured the fluorescence anisotropy of EGFP (r_{EGFP}) at a concentration of ~50 nM in solutions of different macromolecular crowders dissolved in Hepes buffer of pH 7.4. We chose a protein- BSA (Bovine Serum Albumin, molecular weight 66.4 kg/mol), a polysucrose- HiSep (identical to Ficol 1000, molecular weight ~1 kg/mol), amino acids- L-Arginine (174.2 g/mol) and Glycine (75 g/mol), and a salt- NaCl (58.4 g/mol). The value of r_{EGFP} increases linearly with BSA concentration in the mM range. HiSep, amino acids, and NaCl induce a noticeable change in r_{EGFP} at a very high, non-physiological concentration range (**Figure 3.1-B**). Hence, we can conclude that r_{EGFP} is more sensitive to protein concentrations than smaller molecules.

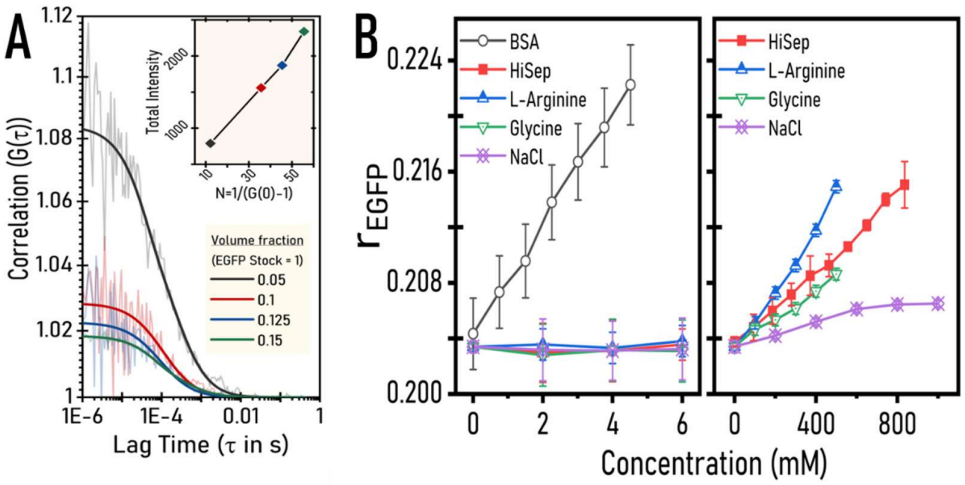

Figure 3. 1: (**A**) FCS data of purified EGFP in 1xPBS (pH 7.3) at 20°C on a 40x water immersion objective. Autocorrelation of fluorescence fluctuations (semi-transparent lines) and their fit (solid lines) are plotted. Inset shows total intensity of the depicted EGFP solutions measured on the FAIM setup vs. their number density measured by FCS. (**B**) r_{EGFP} vs. concentration of different molecular crowders. 0.4nM EGFP was reconstituted in Hepes buffer (100mM, pH 7.4) and the molecular crowders were dissolved in indicated concentrations at 25°C. The solutions were then sandwiched between two glass coverslips with unstretched parafilm spacers and r_{EGFP} was measured on an epifluorescent microscope with a 40x objective.

3.2.2. r_{EGFP} is not sensitive to solution viscosity

Increasing MMC increases both the solution viscosity η [140] and the refractive index n, leading to a decrease in τ, according to the Strickler-Berg equation ($1/\tau \propto n^2$) [133]. Since ${}^{\tau}/_{\theta_C}$ for EGFP is 0.19 in water, a further increase in η should cause a negligible change in r_{EGFP} [136,141]. Therefore, we conclude that the observed increase in r_{EGFP} in crowded solutions is caused mainly by a reduction in τ and an increase in r_0. To establish the independence of r_{EGFP} on η, we compare the fluorescence anisotropy measurement of EGFP (r_{EGFP}) with that of fluorescein (r_{FLRSCN}) in 80-90% glycerol solutions (fluorescein's ${}^{\tau}/_{\theta_C} \approx {}^{4}/_{0.2} \gg 1$) [142]. For these solutions, viscosity (η) increases significantly by 264%, whereas the refractive index (n) changes by a minuscule amount (1%) [143]. The shape of the r_{EGFP} and r_{FLRSCN} plots in **Figure 3.2** establish that an exponential increase of solution η has a negligible effect on r_{EGFP}.

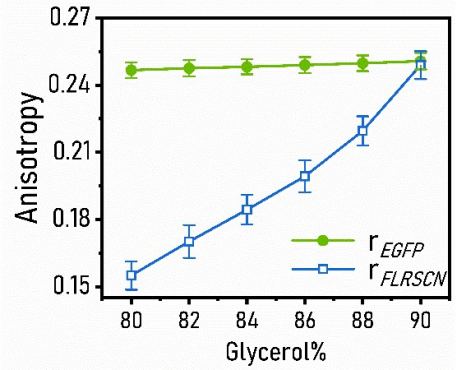

Figure 3. 2: Comparison of fluorescence anisotropies of EGFP (50nM, indicated by green, filled circles) and fluorescein (50nM, indicated by blue, hollow squares) in glycerol-1xPBS solutions with glycerol content ranging from 80% to 90%.

3.2.3. The increase in r_{EGFP} is due to a decrease in τ_{EGFP} and an increase in r_0

We further verified the dependence of r_{EGFP} on τ and r_0 through time-resolved fluorescence anisotropy measurements. We used TCSPC (Time-Correlated Single-Photon Counting) to measure τ_{EGFP} for increasing concentrations of BSA and HiSep (**Figure 3.3-A**), and measured time-resolved fluorescence anisotropy of EGFP in 3 different concentrations of BSA (**Figure 3.3-B**). Increasing crowder concentrations lead to a decrease in the fluorescence lifetime of EGFP, τ_{EGFP} (**Figure 3.3-A**), as expected from the Strickler-Berg equation. However, the intrinsic anisotropy r_0 (**Figure 3.3-C-i**), and rotational correlation time θ_C (**Figure 3.3-C-ii**) increases significantly upon increasing crowder concentrations. We speculate that the increase in r_0 due to increased crowding (thus, increased refractive index) is mediated through changes in the angle between the absorption and emission dipole moments of the EGFP chromophore.

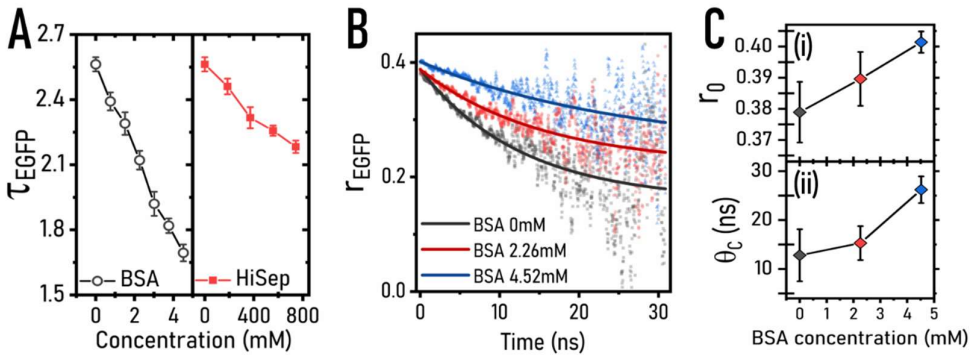

Figure 3. 3: (**A**) TCSPC data for 50 nM EGFP in increasing concentrations of BSA and HiSep. (**B**) Time-resolved fluorescence anisotropy values (symbols) of 50 nM EGFP in increasing BSA concentrations fitted to an exponential decay model (lines) (Reduced χ^2 = 0.00563, 0.00269, 0.00258 for 0, 2.26, 4.52 mM BSA). (**C**) Quantification of r_0 (**i**) and θ_C (**ii**) from time-resolved anisotropy fits. The solutions were made in Hepes buffer (100mM, pH 7.4) and measurements were taken at 25°C.

3.2.4. r_{EGFP} is unaffected by EGFP concentration and solution pH

To verify the robustness of r_{EGFP} as a probe of cytoplasmic MMC, we further explored its dependency on pH and EGFP concentration. **Figure 3.4-A** establishes that r_{EGFP} is independent of the variations in its own concentration, and **Figure 3.4-B** depicts the pH independence of r_{EGFP} in the physiological range. Therefore, cell-to-cell variations in EGFP expression level, cytosolic pH, salt concentrations, or small molecule crowder concentrations will not alter the measured r_{EGFP}, making it a reliable probe of cytoplasmic MMC.

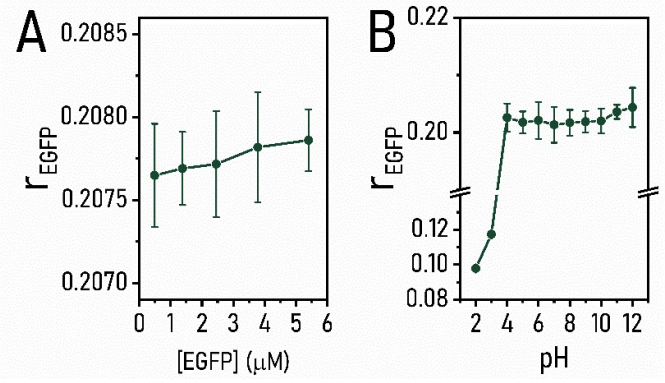

Figure 3. 4: Self-concentration (**A**) and pH (**B**) independence of r_{EGFP}. For (**A**), different concentrations of purified EGFP were diluted in 100mM Hepes (pH 7.4). For (**B**), 50 nM of purified EGFP was diluted in Hepes buffer of varying pH. All r_{EGFP} measurements were performed at 25°C.

3.3. r_{EGFP} measurements in different cell lines

3.3.1. Individual cell lines inherently possess uniquely different cytoplasmic MMC

Having explored the robustness of r_{EGFP} as a reliable probe for MMC *in vitro*, we directly probe the efficacy of r_{EGFP} in the cytoplasm of multiple cell lines. pCAG-mGFP (Addgene #14757) plasmid transfection (by Fugene®, Promega) enables the transient expression of monomeric EGFP in NIH/3T3 fibroblasts, RAW 264.7 macrophages, HeLa carcinomas, and MDA-MB-231 adenocarcinomas, which were further stabilized using geneticin (Sigma, G418-RO) antibiotic selection. Our intracellular r_{EGFP} measurements (**Figure 3.5-A-i, ii**) indicate that the individual cell lines maintain different levels of average cytoplasmic MMC (**Figure 3.5-B**).

We then exposed the different cell lines to hypertonic culture media facilitated by excess dextrose (50 mM and 150 mM) to induce rapid water efflux from cells, thus increasing the cytoplasmic MMC [144–146]. Interestingly, RAW 264.7 macrophages exhibit a more remarkable rise (>15%) in r_{EGFP} within 10 minutes of exposure to either level of hypertonicity when compared to the NIH/3T3, HeLa, and MDA-MB-231 cell lines (**Figure 3.5-C-i, ii**). Further, unlike the NIH/3T3 and HeLa cells, the RAW 264.7 and MDA-MB-231 cells fail to restore the effect of osmotic imbalance endogenously during our 30 minutes observation time.

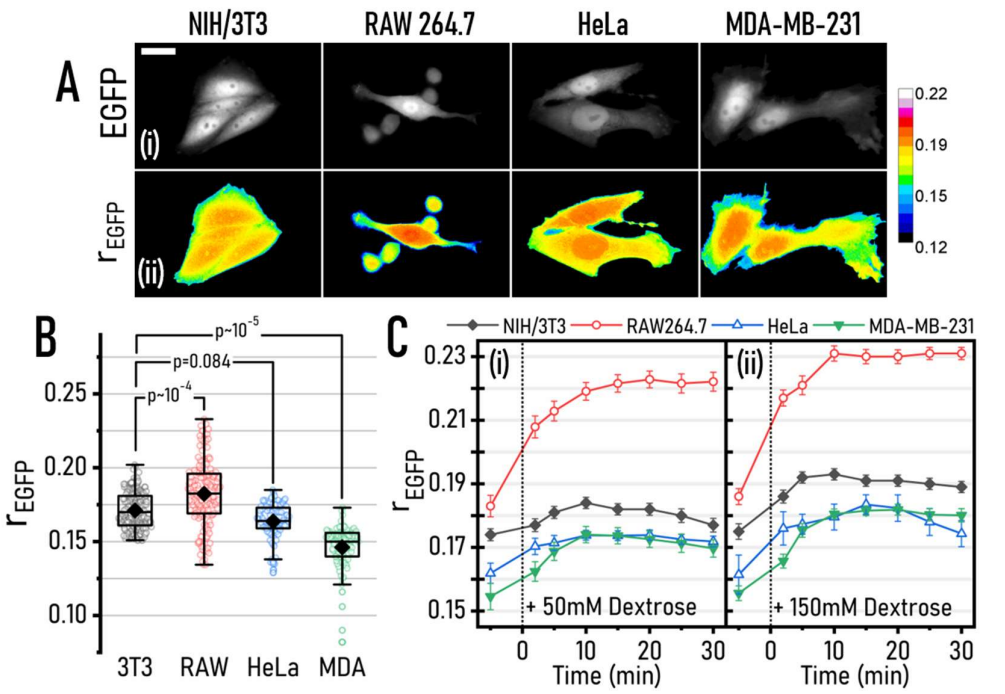

Figure 3. 5: (**A**) Representative images of different cell lines expressing monomeric EGFP (**i**) and their r_{EGFP} maps (**ii**) with color bar indicating the values. Scale bar=30µm. (**B**) Variations of the average intracellular r_{EGFP} levels in the different cell lines. Black diamonds indicate the mean value, horizontal lines of the box represent the 25th, 50th, and the 75th percentile (from bottom). (**C**) Response of the cell lines to hypertonic shock of excess dextrose at the concentrations of 50 mM (**i**) and 150mM (**ii**). Dotted line at t=0 indicates time of hypertonic shock induction

3.3.2. r_{EGFP} reliably tracks MMC in both hypertonic and hypotonic conditions

We exposed different populations of NIH/3T3-EGFP to varying levels of dextrose-supplemented hypertonic shocks. We see that NIH/3T3-EGFP can recover their cytoplasmic MMC from lower hypertonic shocks (50-200 mM dextrose) within 30 minutes (**Figure 3.6-A**), presumably via regulatory volume increase (RVI) [74]. However, these cells cannot recover from higher doses of hypertonic shocks (>200 mM dextrose) within the 30 minutes of our observation span. Fast time-lapse measurement of r_{EGFP} (**Figure 3.6-B**) shows that the cytoplasmic MMC in NIH/3T3-EGFP cells increases rapidly within 80 seconds of exposure to hypertonic conditions of 600 mM dextrose. Subsequently, cells maintain the increased cytosolic MMC for at least 2

hours (**Figure 3.6-C**). Our r_{EGFP} measurements in NIH/3T3-EGFP show that hypotonic conditions (50% dilution of culture media with MiliQ water) make the cells swell up and reduce the cytoplasmic MMC (**Figure 3.6-D**). However, cells can counteract the effect of hypotonic shock within 2 hours (as evident from the r_{EGFP} and cell spread area trajectory), possibly through the phenomenon of regulatory volume decrease (RVD) [74]. These observations suggest that r_{EGFP} measurements permit fast, precise monitoring of a significantly large degree of changes in the cytoplasmic MMC.

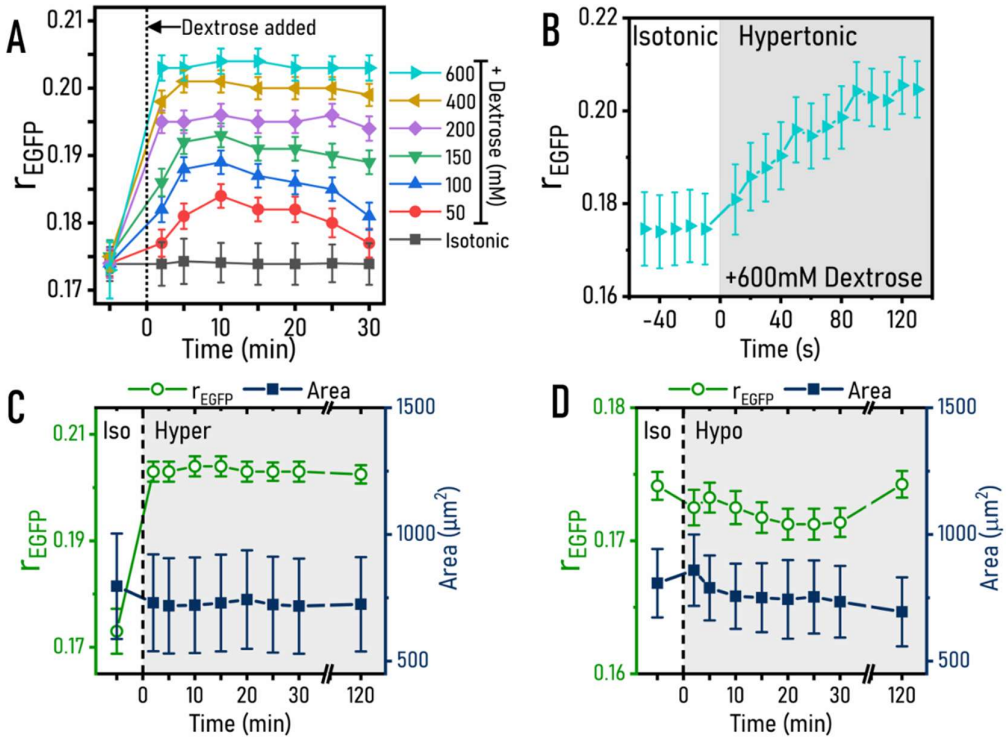

Figure 3. 6: (**A**) NIH/3T3-EGFP cells exposed to varying levels of dextrose supplemented hypertonic shocks. The excess dextrose was added at t=0, as indicated by the dotted line. (**B**) Rapid image acquisition of NIH/3T3-EGFP exposed to 600mM dextrose shows that cells reach the MMC maxima in ~80s after exposure to hypertonic shock at t = 0 s. (**C**) NIH/3T3-EGFP exposed to 600mM dextrose cannot recover from the hypertonic shock within 2 hours. (**D**) Cells exposed to hypotonic shock by diluting the culture media to 50% show that cells counteract the decreased MMC rapidly (within 5 minutes) and the cell spread area decreases significantly after 2 hours in hypotonic media. N>40 cells for each case discussed. Error bars indicate standard deviation.

3.3.3. Elevated MMC reduces the fluorescence lifetime of EGFP (τ_{EGFP}), thereby increasing r_{EGFP}

To verify if the observed hypertonicity-induced increase of intracellular r_{EGFP} is caused primarily by the decrement of its fluorescence lifetime (τ_{EGFP}) [136], we performed FLIM (Fluorescence Lifetime Imaging Microscopy) in NIH/3T3-EGFP exposed to an excess of 150 mM dextrose (**Figure 3.7-A**). Expectedly, τ_{EGFP} decreases in the hypertonic conditions in concurrence with the increase in r_{EGFP} values (**Figure 3.7-B**). There is a noticeable difference in the magnitude of increase in r_{EGFP} induced by decreasing τ_{EGFP} when comparing *in vitro* (**Figure 3.1-B** and **Figure 3.3-A**) and intracellular measurements (**Figure 3.6-A** and **Figure 3.7-B**). Intracellular r_{EGFP} values are greatly affected by the scattering of fluorescence emission by the membranous organelles and cytoskeletal components inside cells. Such artifacts are not present during the *in vitro* measurements made in Hepes buffers having high concentrations of a single crowder molecule.

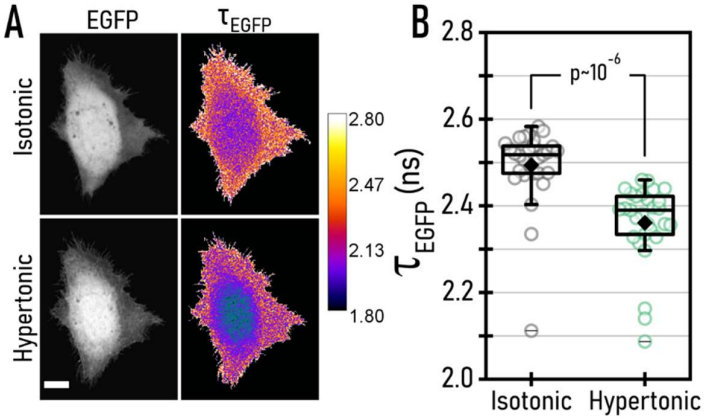

Figure 3. 7: Representative FLIM (Fluorescence Lifetime Imaging Microscopy) images of NIH/3T3-EGFP showing a decrease in fluorescence lifetime (τ_{EGFP}) in hypertonic condtions (+150mM dextrose) (**A**) and its quantification (**B**). Scale bar=10µm.

3.3.4. Hypertonic shock-induced rise of cytoplasmic MMC is dependent on the chemical nature of the osmolyte

A dextrose-induced hypertonic shock of 600 mM causes about ~20% increase in r_{EGFP} in NIH/3T3-EGFP without recovery within 2 hours (**Figure 3.6-A**). However, 600 mM NaCl-induced hypertonic shock causes a

comparatively minor change (~10%) in r_{EGFP} (**Figure 3.8-A**). The lesser change in NaCl-induced shock is presumably because cells can pump out the excess Cl^- and Na^+ ions to alleviate the adverse effects of osmotic imbalance [147,148]. However, hypertonic shock with mannitol, a non-metabolizable analog of dextrose, has an identical impact on NIH/3T3 cells (**Figure 3.8-B**). Reversing the osmotic imbalance (600 mM dextrose) with isotonic DMEM causes immediate reversal of r_{EGFP} to pre-shock value (**Figure 3.8-C**). Thus, showing that the MMC sensing ability of EGFP is not permanently altered by increasing MMC.

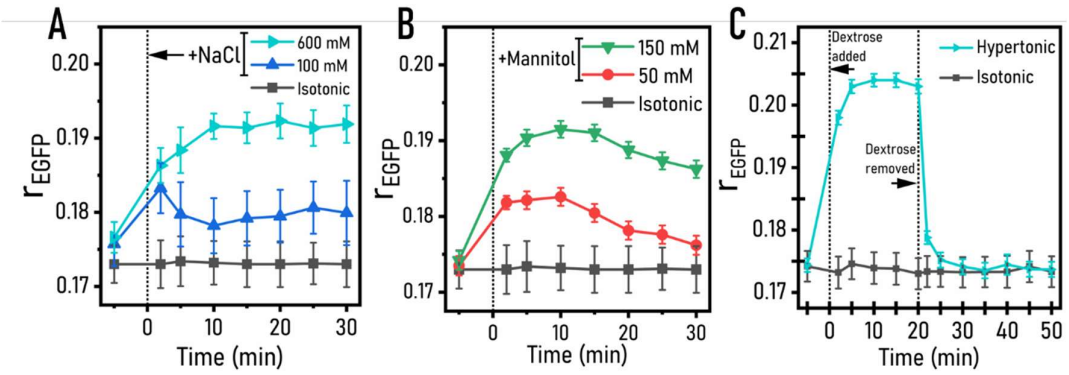

Figure 3. 8: (A) NaCl mediated hypertonic shock on NIH/3T3-EGFP. (B) Mannitol mediated hypertonic shock on NIH/3T3-EGFP. (C) Cells exposed to high dextrose (t=0 min) and media osmolarity restored (t=20 min) show that photophysical properties of EGFP are not permanently altered by MMC. N>60 cells in each quantification of average. Error bars indicate standard deviation.

3.3.5. Nucleic acid compaction during hypertonic shock

Since EGFP localizes both in the cytoplasm and the nucleoplasm, we investigate the impact of enhanced cytoplasmic MMC on the mobility of cytoplasmic and nucleoplasmic proteins using FRAP. **Figure 3.9-A** shows that increasing magnitudes of hypertonicity decreases the mobility of EGFP monotonically in the cytoplasm and the nucleoplasm. In isotonic conditions, the diffusion rate (D) of EGFP is higher in the nucleus than in the cytoplasm. However, upon increasing the culture media hypertonicity, the nucleus and cytoplasm show similar diffusivity of EGFP. Moreover, excessive

hypertonicity causes chromatin to condense in the nucleus (**Figure 3.9-B-i**), presumably via liquid-liquid phase separation [149,150]. Further, the regions of compacted DNA puncta expel EGFP, as visualized by Hoechst staining (**Figure 3.9-B-i**).

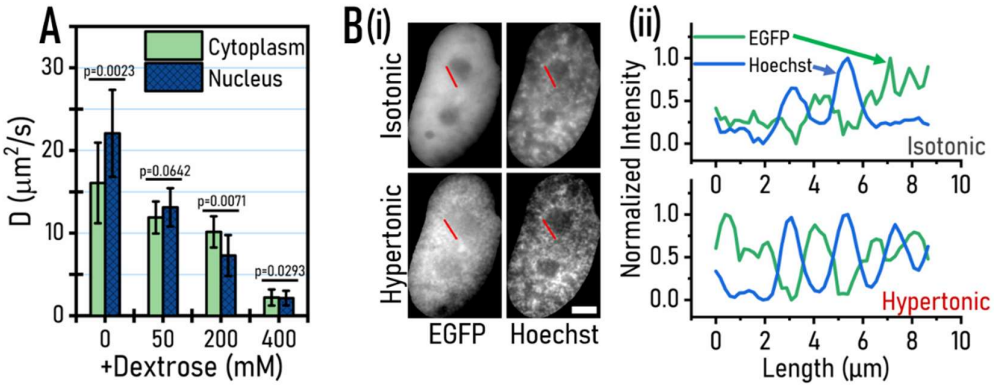

Figure 3. 9: (**A**) Quantification of the average diffusion rate and standard deviation of free EGFP in the nucleus and cytoplasm of NIH/3T3-EGFP via point-FRAP. N>30 cells for each data-set. (**B**) (**i**) Representative image of a NIH/3T3-EGFP nuclei with the DNA stained by Hoechst during isotonic and hypertonic condition (+600 mM dextrose). Image was thresholded according to the Hoechst stain perimeter. Intensities along the line profile (red) in the nuclei images are plotted in (**ii**). Maxima of Hoechst (blue) do not correspond to EGFP (green) maxima. Scale bar = 5 μm.

3.3.6. The mitochondrial matrix is more crowded than the cytoplasm

It is well known that the mitochondrial matrix is more viscous than the cytosol since mitochondria have a comparatively denser composition [151–153]. We took Steady-State FAIM images (**Figure 3.10-A**) of NIH/3T3 cells expressing mito-Dendra2 (Addgene, #55796) and found that mito-Dendra2 has a much higher fluorescence anisotropy than cytoplasmic EGFP (**Figure 3.10-B**), despite Dendra2 having a longer fluorescence lifetime (3.3ns before photoconversion to red emission) than EGFP. According to the Perrin equation, a fluorophore with a longer fluorescence lifetime should have a lower fluorescence anisotropy.

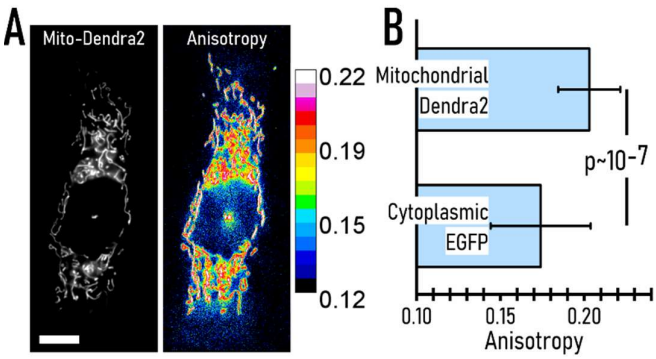

Figure 3. 10: (**A**) Representative images of mito-Dendra2 expression and fluorescence anisotropy. (**B**) Comparison of the averages and standard deviation between Dendra2 expressed in the mitochondrial matrix and EGFP expressed in the cytoplasm. N>50 cells for each quantification. Scale bar = 15 µm.

3.3.7. Isotonic perturbation of cytoplasmic MMC studied through r_{EGFP}

Osmotic imbalances cause rapid changes in cytoplasmic MMC via fast efflux/influx of water. We employ other methods that perturb the cytoplasmic MMC without inducing quick water exchange- (i) by treating cells with Heclin, an inhibitor of HECT E3 ubiquitin ligase [154], to reduce protein degradation, thereby increasing cytosolic protein concentration, (ii) by using Cycloheximide to inhibit protein translation [155], thus reducing cytosolic protein concentration, and (iii) exposing cells to heat shock, causing widespread cytoplasmic protein degradation [156]. Cells incubated with Heclin (70 µM, 4 hours) show a significant rise in cytoplasmic MMC, whereas Cycloheximide treatment (1 µM, 4 hours) causes a small but significant reduction of cytoplasmic MMC. Heat shock (incubation at 42°C for 1 hour, then reverted to 37°C before imaging) causes a considerable decrease in r_{EGFP} values (**Figure 3.11-A**). Using the Bradford assay, we independently validate the findings of **Figure 3.11-A** by estimating total protein mass per cell in response to Heclin, Cycloheximide, and heat shock (**Figure 3.11-A, inset**). RAW 264.7 macrophages inherently have high cytoplasmic MMC, which they fail to auto-regulate under hypertonic conditions (**Figure 3.5**). To understand whether the higher cytoplasmic MMC in RAW 264.7 cells disarms them of their ability to undergo RVI**,** we increased the intrinsic MMC of NIH/3T3-EGFP cells with Heclin treatment (70 µM, 4 hours) and exposed them to 150 mM dextrose supplemented hypertonic shock. **Figure 3.11-B**

shows that increasing the inherent MMC in NIH/3T3-EGFP cells does not deprive them of their ability for RVI, suggesting that the cellular ability to enforce RVI is independent of the cytoplasmic MMC and inherent to the cell type.

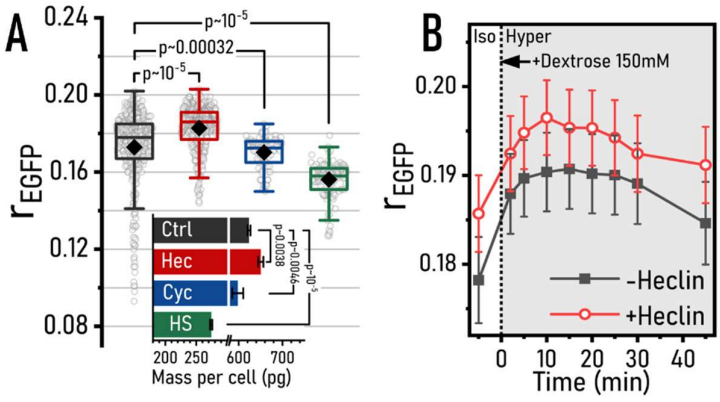

Figure 3. 11: (**A**) (Main)- r_{EGFP} for treatment with Heclin (red), cycloheximide (blue), heat shock (green) and control (dark gray). (Inset)- average protein mass per cell during each treatment. (**B**) Mean and SD r_{EGFP} of Heclin treated cells vs. intreated during hypertonic shock. (N>60 cells)

3.4. Spatial heterogeneity of cytoplasmic MMC

3.4.1. The cytoplasm has a spatially differential response to hypertonic shock

The representative r_{EGFP} images of the different cell lines in isotonic conditions (**Figure 3.5-A**) show that cytoplasmic MMC is non-uniform at a few microns' length scales. Additionally, a significant fraction of different cell lines exhibit a higher nucleoplasmic MMC than the neighboring perinuclear cytoplasm- Hela (~54%), NIH/3T3 (~23%), RAW 264.7 (~16%), and MDA-MB-231 (~14%). Our observations are in direct contrast with the findings of FRET-based sensors [53]. This discrepancy can be explained by the far-field influence (up to 2 μm) of refractive index on fluorescence lifetime [157]. The super-coiled nucleic acid structures reduce the total excluded volume for the freely diffusing macromolecules in the nucleoplasm. Hence, the FRET-based probes cannot probe the true nature of MMC in the nucleoplasm,

similar to EGFP diffusion as per our FRAP results (**Figure 3.9-A**). However, as r_{EGFP} is mainly influenced by the solution refractive index, it can sense the super-structured crowding in the nucleus and thus exhibit higher values than the cytoplasm. We also observe that the lamellipodia-like structures show lower values of r_{EGFP} than the perinuclear regions of the cytoplasm, suggesting differential MMC levels within the cytoplasm. This observation is also prevalent in time-lapse imaging of cells generating new lamellipodial extensions, showing that the MMC in newly developed lamellipodial cytoplasm is lower than the rest of the cell body and agreeing with previous rheology measurements [158]. We find that the lamellipodial edges of NIH/3T3-EGFP exhibit a higher rise in r_{EGFP} than the rest of the cell perimeter (**Figure 3.12**). Numerous articles in the literature body suggest that lamellipodia are abundant with aquaporins and thus can expel more water than non-lamellipodial edges of the cells [159–161]. Hence, we speculate that hypertonic shock-induced water efflux from cells is higher in the lamellipodial structures compared to the perinuclear regions.

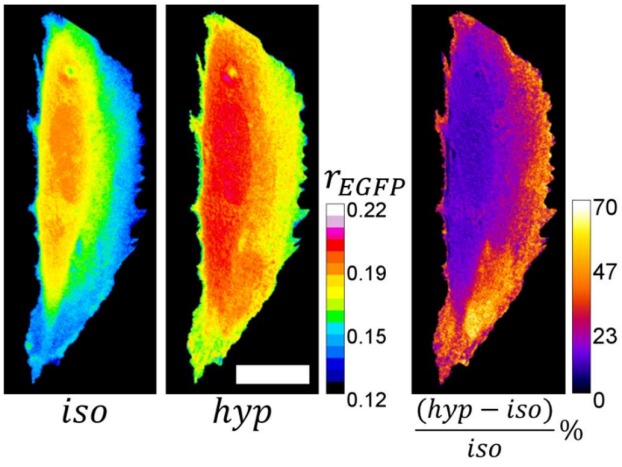

Figure 3. 12: Hypertonic shock (+400mM dextrose) induces spatially differential response in the cytoplasm of HeLa-EGFP. Lamellipodial regions show a higher change in r_{EGFP} than perinuclear regions as visible from the normalized difference ($\frac{hyp-iso}{iso}$ %) map. Scale bar=15µm.

3.4.2. The filamentous actin network facilitates the spatial heterogeneity of cytoplasmic MMC

As actin filament protrusions govern the dynamics of the lamellipodial regions, we measured r_{EGFP} in NIH/3T3-EGFP and stained the cells with phalloidin conjugated Alexa 488 to visualize the actin filaments in cells showing prominent lamellipodial structures. Interestingly, the sharp boundary that separates the low MMC cytoplasmic region at the cortex from the rest of the cytoplasm is often associated with actin filaments (shown by the arrows in **Figure 3.13-A**). We hypothesized that the actin stress fibers might be crucial in maintaining the sharp difference in cytoplasmic MMC. So, we treated NIH/3T3-EGFP with cytochalasin D (2 μM, 1 hour) to depolymerize the actin filaments. Actin filament disruption leads to homogenization of the cytoplasmic MMC (**Figure 3.13-B-i**) and establishes the importance of actin fibers in maintaining the intracellular MMC boundaries. Disruption of microtubules and the intermediate filament vimentin leads to an insignificant change in the spatial distribution of cytoplasmic MMC (**Figure 3.13-B-ii, iii**). Actin disassembly leads to a significant rise in the average cytoplasmic MMC compared to the disassembly of microtubules and vimentin (**Figure 3.13-C**). It is probably because the disassembly of filamentous actin generates a significantly larger concentration of corresponding actin monomers than microtubules and intermediate filaments [162–164].

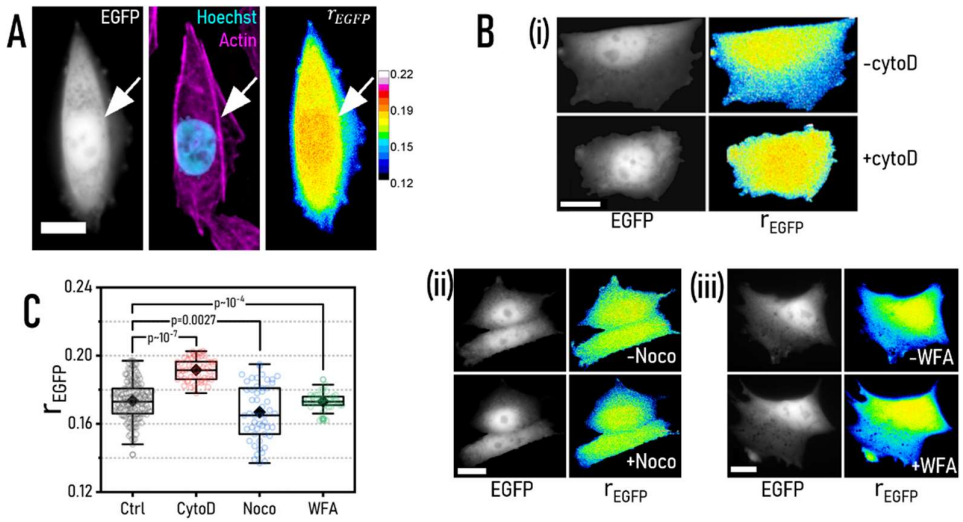

Figure 3. 13: (**A**) Highlighting the spatial variation of MMC governed by the actin cytoskeleton. The arrow indicates the boundary between regions of lower MMC and higher MMC, which has high actin density. First column- EGFP intensity; Middle column- phalloidin-Alexa488 stained actin (magenta) and Hoechst 33342 stained nucleus (cyan); Third column-r_{EGFP} map. Scale bar=15µm. (**B**) Representative images of NIH/3T3-EGFP after disruption of actin by Cytochalasin D (2µM,1h) (**i**), microtubules by Nocodazole (20µM,1h) (**ii**) and vimentin by Withaferin A (3µM,3h) (**iii**). (**C**) r_{EGFP} after disruption of actin by Cytochalasin D (2µM,1h), microtubules by Nocodazole (20µM,1h) and vimentin by Withaferin A (3µM,3h). Scale bar=15µm for every image.

3.4.3. The lower r_{EGFP} values in the lamellipodia is not an artifact of cell height

The vertical height of the lamellipodial regions is comparable to, sometimes even lower than, the objective's axial (Z-axis) resolution. Since the cells show lower r_{EGFP} values in such regions, we assumed that the local height of the cells is the primary factor behind the lowering of r_{EGFP} values. However, an inspection of the FLIM images (**Figure 3.7-A**) reveals that the fluorescence lifetime of EGFP (τ_{EGFP}) is lower in the lamellipodial regions as well. Further still, we independently validated the differential cytoplasmic MMC in the lamellipodial and the perinuclear cytoplasm using alternate methods to estimate MMC. Using FRAP, we compared the translational diffusion rate of EGFP in lamellipodial and the perinuclear cytoplasm (**Figure 3.14-A**). Although higher MMC leads to increased solution viscosity

[140] the FRAP results in **Figure 3.14-A** exhibit an indiscernible difference in the averaged viscosities of the lamellipodial (η = 4.2±1.1 cP) and perinuclear (η = 4.8±1.6 cP) cytoplasm. We concluded that the changes in the bulk viscosity caused by an alteration in MMC are probe-size dependent and cannot be measured with a probe whose size is comparable to or smaller than the crowder molecules [46,47]. Hence, we verify the size dependency *in vitro* by measuring the viscosity of protein solutions (BSA: 0mM, 2.26mM, and 4.52mM) with two different methods. Estimation of solution viscosity with FRAP of EGFP (size of EGFP is comparable to BSA) gives an average η = 2.73±1.1 cP for BSA-free Hepes buffer, η = 3.37±1.32 cP for 2.26 mM BSA, and η = 3.51±3.64 cP for 4.52 mM BSA at 20℃ (**Figure 3.14-B**). However, estimation of solution viscosity using the passive PTM method with a probe bigger than the crowder molecules, i.e., 200nm fluorescent microspheres (**Figure 3.14-C**), provides η = 1.48±2.72 cP for Hepes buffer (0 mM BSA), η = 3.09±5.41 cP for 2.26 mM BSA, and η = 26.02±4.07 cP for 4.56 mM BSA at 20℃, which are significantly different from the FRAP measurements, and agrees with reported bulk viscosity measurements [165].

Our measurements indicate that a 30%(w/v) increase in MMC using BSA affects the translational thermal motion (Mean Squared Displacement or MSD) of probe EGFP molecules by only 22%; as a result, only a tiny change in solution viscosity is observed by FRAP (**Figure 3.14-B**). However, a similar increase in MMC using BSA reduces the translational thermal motion of the bigger-sized probe particles by 94%, as observed by the passive PTM technique (**Figure 3.14-C**)**.** The comparison of the MSD of 200nm tracers reveals that the lamellipodial cytoplasm has a lower crowding (η = 2.22±1.63 cP) in comparison to the perinuclear cytoplasm (η = 18.56±15.82 cP) (**Figure 3.14-D**).

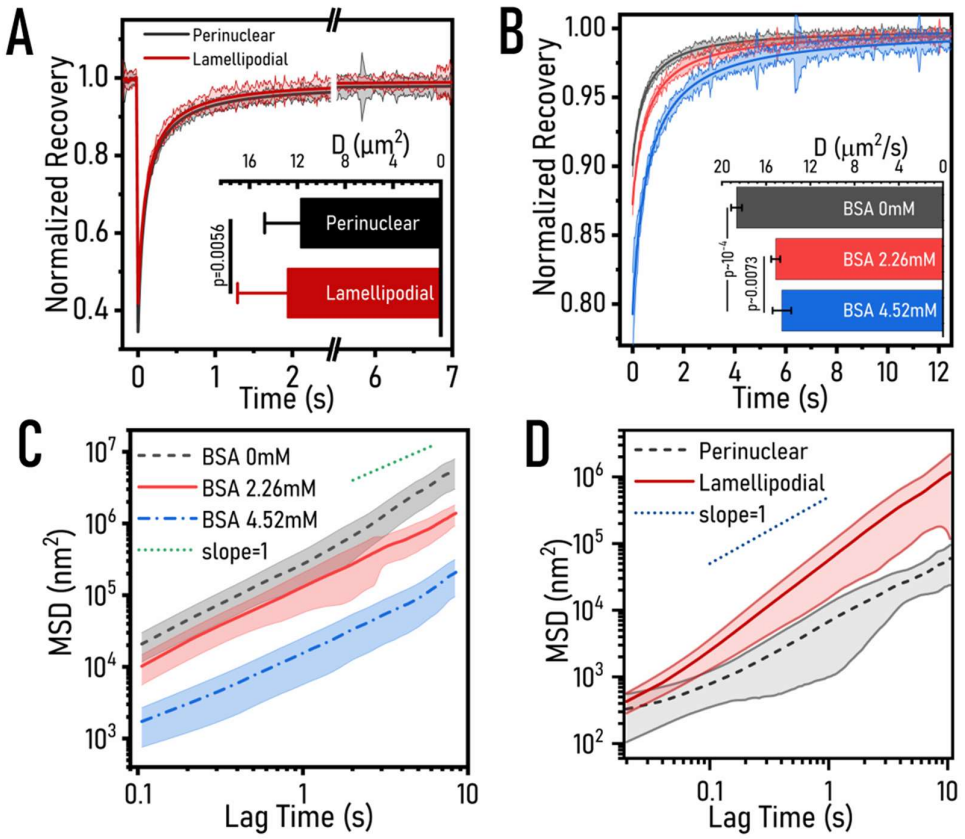

Figure 3. 14: (**A**) FRAP analysis of translational mobility of EGFP in the lamellipodial and perinuclear regions. (**B**) FRAP of purified EGFP in BSA solutions of indicated concentrations prepared in 100mM Hepes buffer (pH 7.4) at 25°C. (**C**) Mean Squared Displacement (MSD) from single particle tracking (passive PTM) of 200nm sized fluorescent microspheres in the same BSA solutions and under the same physical conditions as in (**B**). (**D**) Mean Squared Displacement (MSD) from single particle tracking of fluorescent microspheres in the lamellipodia and perinuclear regions.

3.4.4. Intracellular r_{EGFP} values are not compromised by homo-FRET

If the intracellular concentration of EGFP is so high that the average inter-fluorophore distance reduces to the Forster's radius, then homo-FRET is a likely possibility. To eliminate any scope of homo-FRET, we performed photobleaching experiments in EGFP (monomer) and 2GFP (EGFP dimer) expressing NIH/3T3 (**Figure 3.15-A**). Photobleaching EGFP expressing cells by ~20% does not affect the mean anisotropy value of the population, while photobleaching 2GFP expressing cells by ~20% increases the mean

anisotropy value of the cell population by ~7.5%. Thus, the intracellular EGFP concentration of the cells in our observation population does not lie in the homo-FRET regime. However, the 2GFP expressing cells exhibit homo-FRET even in the same total intensity range as the EGFP expressing cells. FCS in selected cells with varying EGFP expression levels puts the maximum intracellular EGFP concentration in the experimental population at 30.2 µM. The representative auto-correlation curve for the cell is provided in **Figure 3.15-B**. Since all the cells used for anisotropy measurements were from the same stock, we expect the intracellular concentration of EGFP to be in a similar range. Furthermore, we used the concentration estimation from our FCS data of EGFP solutions (**Figure 3.1-A-inset**) to evaluate the intracellular concentration of EGFP to be in the 2-20 µM range for the cell population used in the homo-FRET validation experiment (**Figure 3.15-B-inset**). The intracellular EGFP concentration estimation was obtained by deriving the relationship between the concentration of purified EGFP solutions (obtained from FCS) and the fluorescence intensity (at identical excitation power used for the cells) on our anisotropy setup.

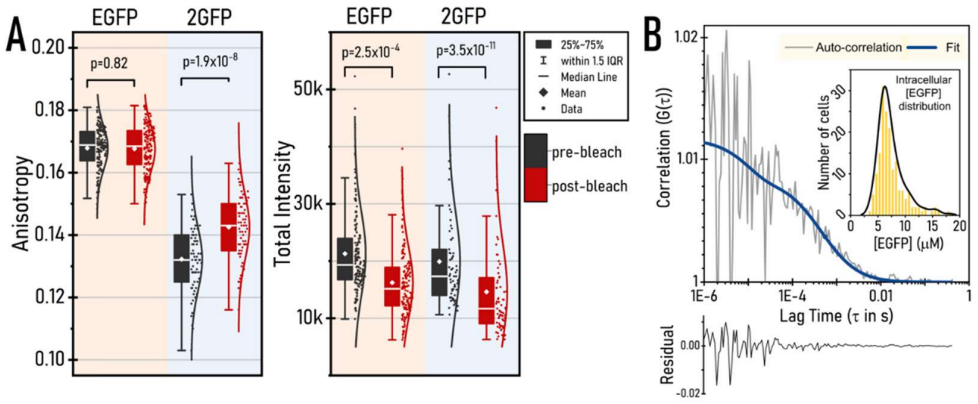

Figure 3. 15: (**A**) Fluorescence anisotropy and total intensity of EGFP (172 cells) or 2GFP (75 cells) expressing NIH/3T3 pre- and post- photobleaching.
(**B**) Representative autocorrelation curve (gray) and its fit (blue) in a bright NIH/3T3-EGFP cell, with the residual presented below. Inset shows the estimated concentration of EGFP in the cell population used for the homo-FRET validation experiment in (**A**).

3.5. Materials and methods

3.5.1. Cell culture and pharmacological studies

NIH/3T3 cell line was procured from NCCS (National Center for Cell Science, Pune, India). RAW 264.7 cell line was a generous gift from Dr. Sanjay Dutta (CSIR-Indian Institute of Chemical Biology, Kolkata), while HeLa and MDA-MB-231 cell lines were kindly gifted by Dr. Prosenjit Sen (Indian Association for the Cultivation of Science, Kolkata). Fugene® (Promega) was used to transfect cells with the following plasmids: pCAG-mGFP, a gift from Connie Cepko (Addgene plasmid # 14757); mCherry-Lifeact-7, a gift from Michael Davidson (Addgene plasmid # 54491); and EGFP-p65, a gift from Johannes A. Schmid (Addgene plasmid # 111190), following standard protocol. Cells cultured in DMEM (Himedia, #AI007G) at 37℃, 5% CO_2 in a humidified incubator, were seeded on custom-made glass bottom 35mm petridishes. The glass was coated with 50mg/mL Fibronectin (Sigma, #F1141) to promote rapid adhesion and proper spreading. Before microscopy, cells were gently washed with 1xPBS twice, and culture media was replaced with phenol red-free DMEM (Gibco, #21063029), which could be supplemented with the required drug when necessary. For all pharmacological treatments, Cytochalasin D (Merck, #C8273), Nocodazole (Merck, #487928), Withaferin A (Merck, #W4394), Heclin (Tocris, #5433), and Cycloheximide (Sigma, #18079) were dissolved in DMSO, and working concentrations were reconstituted as indicated in appropriate places. For applying heat shock, cells were incubated at 42℃ for 1h in the presence of 5% CO_2. To create osmotic imbalance, cells were first imaged in an isotonic complete medium, and then the culture media was replaced with either hypertonic or hypotonic complete medium using a custom-made flow system. Hypertonic media was prepared by adding Dextrose, Mannitol, or NaCl (Merck Empura) to phenol red-free DMEM at indicated concentrations and filtered for decontamination. Hypotonic media was prepared by adding

autoclaved MiliQ water to phenol red-free DMEM at the required amounts to create the desired osmolarity.

3.5.2. r_{EGFP} measurement

Cells seeded on glass-bottom petridishes were imaged with a 40x air immersion objective (NA 0.75) using the Zeiss AxioObserver Z1 epifluorescence microscope. Light from a mercury arc lamp (HXP 150) was passed through a linear polarizer (ThorLabs) to create horizontally polarized light. The resulting polarized fluorescence signal from the cells passes through a polarizing beam splitter (DV2, Photometrics) to divide the emission light into parallel and perpendicular polarizations. The light is then collected by a CMOS camera (Hamamatsu Orca Flash 4.0 C13440), and the polarized fluorescence signal appears as an image having 2048x2048 pixels, with each half (1024x2048 pixels) representing the parallel and perpendicularly polarized emission, respectively. Due to misalignment in the optical path, the two halves don't completely overlap. To resolve this, fluorescent polystyrene microspheres of 200nm diameter are dried on a glass coverslip and imaged in the same arrangement as r_{EGFP} measurement, such that the images of the beads may serve as fiduciary markers to register the two halves of the image. Using the Descriptor-based Registration plugin of Fiji (ImageJ) [166] and a custom Fiji Macro, the left (perpendicular channel, $I_{\perp}$) and right (parallel channel, $I_{\parallel}$) half of the 2048x2048 image is registered to create the best possible overlap of the corresponding pixels in both channels. Thence, r_{EGFP} is calculated for each pixel using the relation:

$$r_{EGFP} = \frac{I_{\parallel} - gI_{\perp}}{I_{\parallel} + 2gI_{\perp}}$$

where g refers to the G-factor. Images of 100nM fluorescein solution are used to find the G-factor. To correct for background fluorescence, a 2048x2048pixel image of the phenol red-free DMEM, having no cells and illuminated by similar conditions as the experimental subjects, was

subtracted from each 2048x2048 image. This process eliminates the background fluorescence of both the parallel and perpendicular channels in the correct ratio. The resultant r_{EGFP} the image was saved as a 32-bit TIFF image file, thresholded based on intensity (15000-50000 count for 16-bit image), and further analyzed using a custom-written code in Fiji (ImageJ). Statistics of at least 30 cells were collected for each experiment and their mean r_{EGFP} and the standard error of the mean was plotted. Confidence testing was performed with a Two-sample T-test in each case. A more detailed description is available in **Section 2.2.1** of this dissertation.

3.5.3. Fluorescence Recovery After Photobleaching (FRAP)

Using a home-built FRAP setup, photobleaching and recovery were imaged with a 488nm Laser (Coherent) through the 63x oil immersion objective of Zeiss AxioObserver Z1. Briefly, the 0.42mW Laser beam was split in a 90:10 ratio. The resultant beams were collimated using a lens system to be incident parallelly on the back focal plane of the microscope objective. The beams were aligned to illuminate the same spot (of 2μm diameter) when imaged with the 63x objective. The low-intensity beam was further dimmed using neutral density filters to minimize photobleaching and image the circular spot. To perform FRAP, the circular spot was continuously imaged at a rate of 50-100 frames per second with only the low-intensity beam. After 70-100 frames, the high-intensity beam was exposed for 10ms using a programmable shutter (Thorlabs, SC10) to achieve fast photobleaching. Imaging is continued for a total of 2000 frames, by which time the intensity of the spot becomes constant, indicating completion of recovery. The fluorophore's diffusion rate and mobile fractions are calculated by fitting the intensity recovery data from the spot with a custom-written MATLAB code, as explained in [118]. Before studying live cells, the FRAP setup was calibrated using a glycerol-water mix of known viscosity containing 100 nM fluorescein. A more detailed description is available in **Section 2.1.1** of this dissertation.

3.5.4. Single Particle Tracking

Fluorescent polystyrene beads of diameter 200nm (Invitrogen, #F8888) were imaged with a 63x oil immersion objective at a rate of 100 frames per second to capture the thermal motion. For *in vitro* measurement, beads were suspended in BSA solutions at previously indicated concentrations. The beads were ballistically injected with the Helios Gene Gun (BioRad) delivery system for intracellular measurement. Cells were "shot" with a pressure of 100PSI from a distance of 3-4cm from the petridish. Cells were gently washed with serum-free media thrice to remove beads stuck on the plasma membrane or glass. Then the cells were incubated in phenol red-free DMEM at 37℃, 5%CO_2 for 2h to allow them to recuperate. The trajectories of the fluorescent beads were extracted using the Mosaic plugin (Particle Tracking 2D/3D) of ImageJ. The following relation was used for MSD computation of a bead with trajectory (x_t, y_t): $MSD(\tau) = \langle (x_{t+\tau} - x_t)^2 + (y_{t+\tau} - y_t)^2 \rangle$, where, τ is the lag-time. MSD computation was performed using a custom-written MATLAB code. A more detailed description is available in **Section 2.3.1** of this dissertation.

3.5.5. Calculation of viscosity coefficient ($\boldsymbol{\eta}$) from Diffusion constant ($\boldsymbol{D}$) or Mean Squared Displacement ($\boldsymbol{MSD}$)

The Stoke-Einstein equation: $D = k_B T / 6\pi\eta r$, where r is the Stoke's radius of the particle of interest, relates D with η. Using r=4.2nm for EGFP, we can calculate η for simple diffusion of EGFP. Since $MSD(\tau) = 4D\tau$ (in 2D), we can easily obtain η using the Stoke-Einstein relation.

3.5.6. Time-resolved fluorescence anisotropy and fluorescence lifetime measurements

BL21 (DE3) *E. coli* variant, transformed to express monomeric EGFP, was grown to log phase (OD_{600} ≅ 0.7) in a 500 mL culture by 12 h incubation at

37℃. Then EGFP expression was maximized through Isopropyl ß-D-1-thiogalactopyranoside (IPTG) induction (40 mg/ml, 37℃, 4 h). The bacteria were harvested by centrifugation (6500 g, at 4℃ for 5 min), and the cell pellet was resuspended in 5 mL lysis buffer containing 50 mM Tris-HCl, 150 mM NaCl, 0.1X Protease Inhibitor and 1 mg/ml Lysozyme. The cells were then mechanically lysed using a probe sonicator (Cycle: 0.5, Amplitude: 30%) in an ice bath for 30 min. The cell debris were separated by centrifugation (10000 g, at 4℃ for 40 min) and the supernatant was collected. Proteins heavier than EGFP (MW: 27kDa) in the supernatant were salted out by slow addition of 80% $(NH_4)_2SO_4$ solution (w/v) (upto a final concentration of 20%). The precipitate was centrifuged for removal (13500 g, at 4℃ for 45 min) and the remnant proteins in the supernatant, including EGFP, were salted out using 40% $(NH_4)_2SO_4$ solution (final concentration). The precipitate was resuspended in 3 mL 50 mM Tris-HCl buffer and was dialysed against the same buffer overnight with mild stirring at 4℃. The dialysed solution was subjected to Ni-NTA affinity chromatography using standard protocol and the purified EGFP was lyophilized and reconstituted in Hepes (SRL, #63732) buffer of pH (7.2-7.6). The concentration of the reconstituted EGFP was estimated from UV absorbance and fluorescence correlation spectroscopy. Subsequently, the reconstituted EGFP was diluted to ~50 nM for all experiments (except r_{EGFP} vs EGFP concentration). Fluorescence lifetime and time-resolved anisotropy decay measurements were done using the DeltaFlex™ system (Horiba) using 4-side transparent UV quartz cuvettes.

3.5.7. Fluorescence Lifetime Imaging Microscopy (FLIM)

FLIM was carried out using a pico-second 480nm laser (PicoQuant), and fluorescence lifetime data for individual pixels were fitted to mono-exponential decay using the SymPhoTime64 software. The resultant 32-bit TIFF image was analyzed in a similar way as in r_{EGFP} measurements with Fiji (ImageJ) [166]. Cells were seeded on glass-bottom 35mm petridishes, and

hypertonic stress was applied following the same protocol as in r_{EGFP} experiments. Data of 30 cells were used for statistics.

3.6. Discussion

Our method of predicting macromolecular crowding using fluorescence anisotropy of EGFP is unprecedented and offers an easy, high-throughput way to estimate the MMC both *in vitro* and *in vivo*. Measurement of r_{EGFP} in solutions with controlled crowding establish that r_{EGFP} can reliably track macromolecular crowding to a high degree of precision. We find that changes in r_{EGFP} are more sensitive to proteins than polysucrose, amino acids, or salts. We show that MMC lowers τ and increases r_0 of EGFP, giving a linear relation between r_{EGFP} and crowder concentration. We show that r_{EGFP} is independent of solution pH, viscosity, and EGFP concentration in the physiological range. Intracellular r_{EGFP} measurements show that different cell lines maintain distinctly unique levels of average cytoplasmic MMC. The average cytoplasmic MMC in NIH/3T3 fibroblasts is maintained tightly for a relatively long time (at least 8h) if the spread area does not change significantly. Intracellular r_{EGFP} responds well to osmotic shock and can track the changes in intracellular MMC reliably, without any permanent alteration to the EGFP molecule. Additionally, intracellular MMC is spatially inhomogeneous, and the actin cytoskeleton is crucial in separating regions of varying MMC. The cellular regions containing lower MMC show a comparatively larger change in response to hypertonic challenges. The variability of cytoplasmic MMC cannot be estimated by tracking the translational diffusion rate of protein-sized probes like EGFP. Instead, larger probes of the size ~100 μm or bigger are necessary to visualize the difference in apparent viscosities imposed by the heterogeneous MMC. Earlier works [138,139,167] have utilized intracellular fluorescence lifetime measurements of the EGFP-family. However, compared to the complicated instrumentation of FLIM, r_{EGFP} is easier and more high throughput.

Chapter 4: Cytoplasmic Macromolecular Crowding- a cell volume sensor?

The degree of cytoplasmic macromolecular crowding (MMC) determines the thermodynamic activity of all the essential intracellular biochemistry. Hence it is intuitive to guess that any fluctuation in the volume of a cell will alter the intracellular MMC, and thus biochemical reaction rates. Whether the cell utilizes the alteration in the reaction kinetics of specific molecules to "sense" its volume is a question still unanswered. Having established r_{EGFP} as a reliable probe to measure intracellular MMC, we investigated if a cell uses the cytoplasmic MMC to sense its volume.

4.1. Cytoplasmic protein aggregation may resist osmotic cell volume shrinkage in hypertonic conditions

4.1.1. Cell volume and r_{EGFP} do not change equivalently in hypertonic conditions

Hypertonic conditions ensue rapid water efflux from cells, increasing the intracellular MMC and causing numerous proteins to undergo liquid-liquid phase separation in the cytoplasm [32,33,69,168]. Upon measuring cell volume at increasingly hypertonic conditions when r_{EGFP} scores the highest (10 minutes post-exposure to hypertonicity), we find that cells do not undergo the same level of shrinkage as expected from a "sealed box" of molecules, like a cell (**Figure 4.1-A**). The plasma membrane does not permit a free exchange of macromolecules with its surroundings. Aquaporins and ion channels only allow small molecules to be exchanged with the extracellular

space. Thus, the macromolecular concentration in the cytoplasm should be inversely proportional to the cell's volume if the number of macromolecules remains unchanged during any cellular process.

As r_{EGFP} scales linearly with protein concentration (say, C) (**Figure 3.1-B**), then $r_{EGFP} = m \times C + \alpha$, which implies, $C = \frac{r_{EGFP} - \alpha}{m}$. Now, if we consider a cell with a volume V_1 having protein concentration $C_1 = \frac{r_{EGFP,1} - \alpha}{m}$ shrinking to a volume V with a protein concentration $C = \frac{r_{EGFP} - \alpha}{m}$ during hypertonic shock, then since $C_1 V_1 = CV$, therefore $\frac{r_{EGFP,1} - \alpha}{m} V_1 = \frac{r_{EGFP} - \alpha}{m} V$, thus implying $r_{EGFP} = \frac{V_1}{V}\left(r_{EGFP,1} - \alpha\right) + \alpha$. In our investigation of the cytoplasmic r_{EGFP} dependency on cell volume (V) at different hypertonic conditions (**Figure 4.1-A**), we find that the shape of the measured r_{EGFP} vs. cell volume (V) curve deviates from the expected trendline: $r_{EGFP} = \frac{V_1}{V}\left(r_{EGFP,1} - \alpha\right) + \alpha$ (indicated by the arrows). The deviation of the r_{EGFP} vs. V curve suggests that in addition to cell volume change, other cellular processes may alter r_{EGFP} in hypertonic conditions. The shape of the curve in **Figure 4.1-A** suggests that either the total number of cytoplasmic macromolecular crowders increases in hypertonic conditions or the effective size of the crowders changes. However, there is no measurable increase in the average protein mass per cell in response to hypertonic shock (**Figure 4.1-B**). Thus, there is no significant change in the cytosolic protein content in response to hypertonic shock. Therefore we explore other possibilities like the reorganization of the cytoplasmic macromolecular crowders in response to hypertonic shock that changes the effective crowder size and causes the additional rise of r_{EGFP}, as in **Figure 4.1-A**.

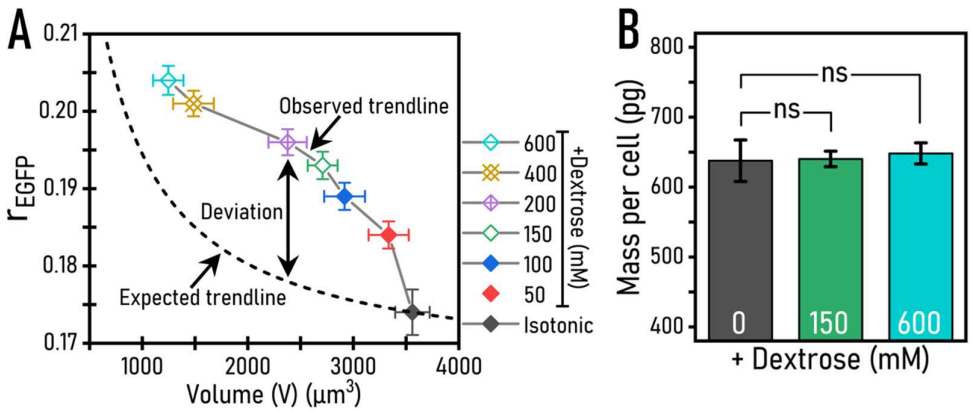

Figure 4. 1: (**A**) The observed r_{EGFP} vs. V curve deviates from the expected trendline for volume measurements at 10 minutes post excess dextrose addition. (**B**) Average protein mass per cell at indicated excess dextrose concentrations

4.1.2. Cell fixation causes r_{EGFP} to rise

We mimicked the reorganization of cytoplasmic proteins by fixing NIH/3T3-EGFP with 4% PFA (paraformaldehyde). Fixation by 4% PFA causes covalent links between neighboring protein molecules, increasing the effective crowder size around EGFP molecules. **Figure 4.2** compares the cytoplasmic r_{EGFP} of cells before and after fixation, confirming our speculation that an increase in the effective crowder size is an additional factor that can increase r_{EGFP} along with the change in cell volume.

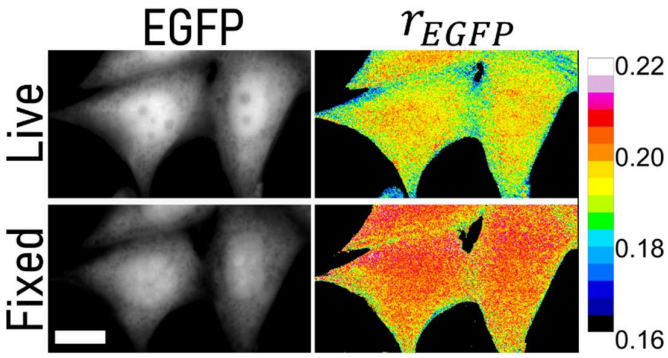

Figure 4. 2: NIH/3T3-EGFP before and after fixation

4.1.3. Non-specific cytoplasmic protein condensation during hypertonic shock

AiryScan super-resolution imaging of cytoplasmic EGFP in cells exposed to different hypertonic strengths confirms protein aggregation in the cytoplasm (**Figure 4.3-A**). However, increasing cytoplasmic MMC isotonically with Heclin treatment does not lead to noticeable protein aggregation (**Figure 4.3-B**). Literature suggests that multivalent proteins form aggregates in response to increased MMC via self-condensation [31–33,169].

While free EGFP shows a non-specific weaker aggregation in the cytoplasm, NFκβ, a protein with a DNA binding domain [170–172], shows globular self-aggregation in response to hypertonic shock in NIH/3T3 cells expressing p65-EGFP (Addgene, #111190), a subunit of the NFκβ complex (**Figure 4.3-C**). However, in Heclin treated NIH/3T3, NFκβ shows drastically massive, irregularly shaped aggregates (**Figure 4.2-D**), visibly different than the globular condensates from hypertonic shock. Hence, we speculate that protein condensation in the cytoplasm may resist osmotic cell volume shrinkage during hypertonic conditions. We observe that the rise in MMC due to hypertonic imbalance is either maintained (for ≥200 mM dextrose) or is gradually restored (for ≤200 mM dextrose) within 30 minutes of hypertonic shock. While non-specific aggregation of EGFP is not apparent in cases of ≤200 mM dextrose, NFκβ visibly forms condensates even under such conditions (data not shown).

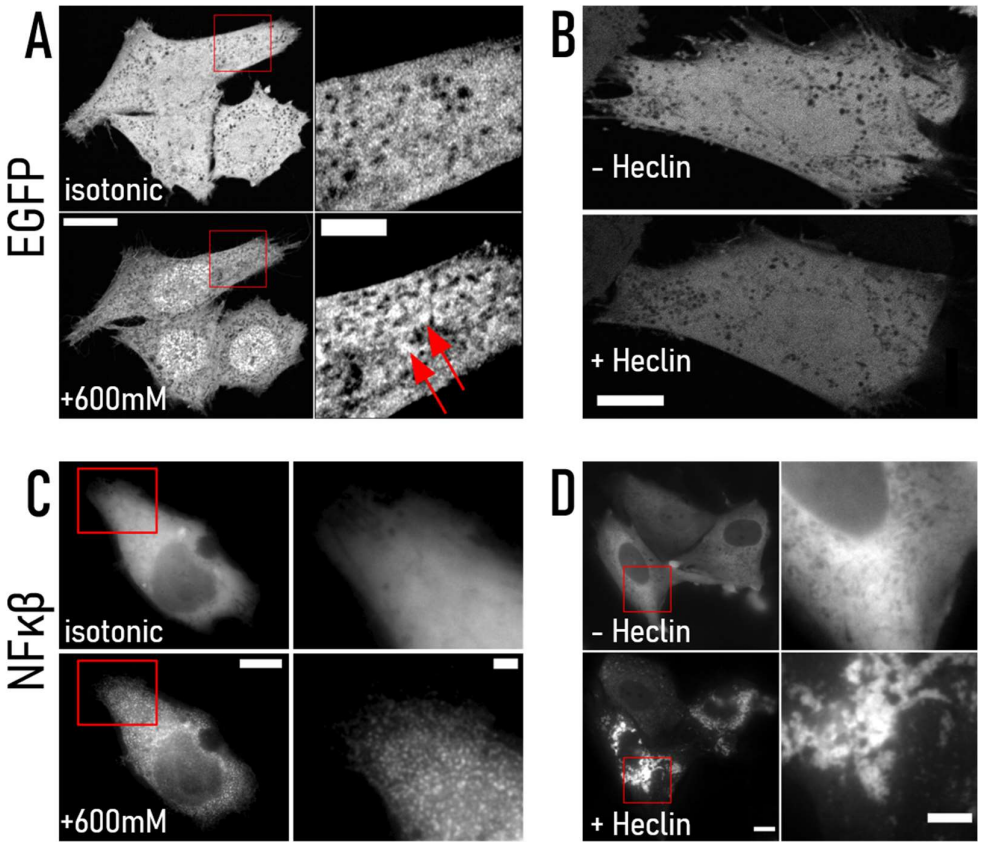

Figure 4. 3: (**A**) AiryScan super-resolution imaging of NIH/3T3-EGFP reveals submicron clustering of EGFP under hypertonic conditions (+600mM dextrose). Scale bar: main=15µm, inset=5µm. (**B**) AiryScan super-resolution imaging of NIH/3T3-EGFP before and after Heclin treatment shows no apparent aggregation of EGFP. Scale bar: main=15µm, inset=2µm. (**C**) NIH/3T3 show NFκβ-EGFP condensation in similar hypertonic conditions as (**A**). Scale bar: main=10µm, zoomed inset=2µm. (**D**) NFκβ-EGFP aggregates observed after treatment with Heclin (70µM,4h) in NIH/3T3. Scale bar=10µm, zoomed inset=5 µm (brightness-contrast adjusted for visualization)

Whether NFκβ condensation has a role in facilitating RVI at later time points remains unanswered. Previous studies [168] have shown that the WNK proteins phase-separate under hypertonic conditions and differentially regulate enzyme activity to trigger RVI. NFκβ has extreme importance in numerous biochemical pathways. Hence, we speculate that NFκβ could have a signal transmission role in the cell volume regulation pathway. The condensate forming behavior of NFκβ and WNK implies that liquid-liquid phase separation is an essential intracellular phenomenon that regulates cell volume.

4.2. Cell volume regulation and MMC during cell spreading

4.2.1. The morphological spread area of NIH/3T3 fibroblasts is proportional to cell volume and inversely related to r_{EGFP}

In NIH/3T3-EGFP fibroblasts seeded on fibronectin-coated glass, the morphological spread area of the cells and the corresponding average cytoplasmic MMC (r_{EGFP}) per cell exhibits a weak negative correlation (linear correlation coefficient $r = -0.386$) (**Figure 4.4-A**). Since cytoplasmic MMC should be inversely proportional to the volume of the cell, we speculated that the volume (V) and spread area (A) of the cells should exhibit a positive correlation. Expectedly, we find the spread area and volume of NIH/3T3 to be linearly related- $V = 4.2A + 86.8$ (**Figure 4.4-B**), with the positive correlation coefficient ($r = 0.909$). The positive correlation between the cell spread area and volume could arise due to a cell's size corresponding to its cell cycle stage or the extent of the morphological spreading independent of its cell cycle stage. Post adhesion, the time taken by cells to spread on glass substrates is significantly less than the time taken to transit through the G1, S, or G2 phases. Thus any effect on r_{EGFP} in this timescale is an effect of cell spreading, not cell cycle transition. We find that the area and volume in the spreading cell population also exhibit a positive correlation ($r = 0.818$) (**Figure 4.4-C**). However, the $V - A$ relation in spreading cells shows a slightly different slope: $V = 2.5A + 963.4$. Further, we find that r_{EGFP} decreases concurrently with increasing cell spreading (**Figure 4.4-D, 4.4-E**), as evident from continuous r_{EGFP} measurement at 10 minutes intervals, starting from 15 minutes post-seeding on fibronectin-coated glass. Thus, we can conclude that the spread area-MMC correlation of NIH/3T3-EGFP in **Figure 4.4-A** is a direct consequence of the cells' morphological spreading, not the cell cycle stage.

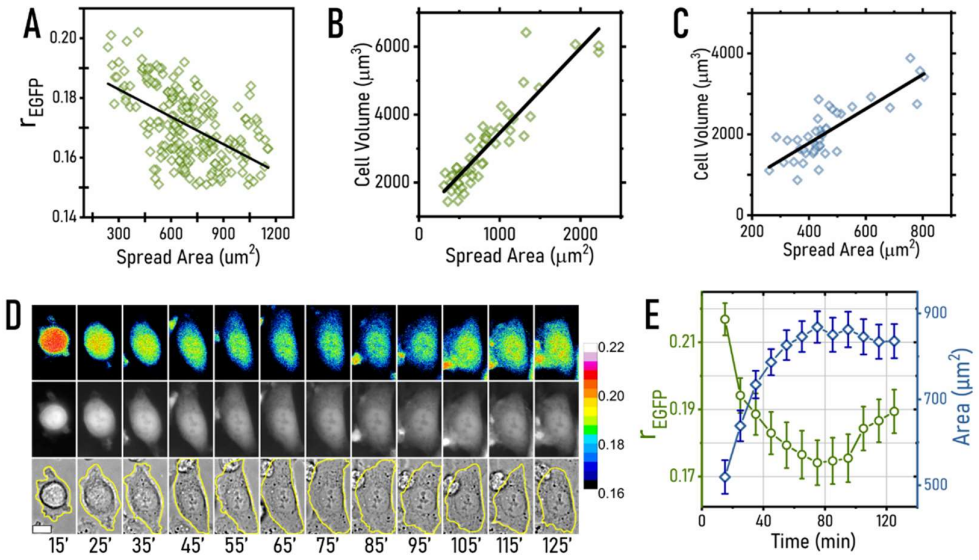

Figure 4. 4: (**A**) Scatter plot and linear correlation of average r_{EGFP} per cell vs spread area of NIH/3T3-EGFP for cells seeded on fibronectin-coated glass. (**B**) Cell volume vs spread area of NIH/3T3-EGFP in well-spread condition (on fibronectin-coated glass, post 24 hour of seeding). (**C**) Cell volume vs spread area of NIH/3T3-EGFP during spreading (on fibronectin-coated glass, post 15 mins of seeding). (**D**) Representative NIH/3T3-EGFP post seeding on fibronectin-coated glass with r_{EGFP} (top row), EGFP expression (middle row) and brightfield (bottom row). Scale bar = 10µm. (**E**) Quantification of average r_{EGFP} (green) and spread area (blue) of NIH/3T3-EGFP during spreading on Fibronectin coated glass. Error bars represent standard deviation of the quantities mentioned (N = 54 cells).

4.2.2. Restricting cell spreading prevents the decrease of r_{EGFP} post adhesion

If the cytoplasmic MMC were to be a sensor for cell volume regulation, cells must regulate their volume to maintain the MMC during cell spreading. On the contrary, despite no change in the extracellular tonicity, the average cell volume increases, leading to a decrease in cytoplasmic MMC during cell spreading (**Figure 4.4-D, 4.4-E**). There is a change in both cell volume and the cytoplasmic MMC in the time scales required for a cell to spread on fibronectin-coated glass. This observation alone cannot confirm whether the cells regulate their volume in response to the increased cytoplasmic MMC or if the cell volume changes are independent of the changes in cytoplasmic

MMC. If cell volume regulation is triggered to control MMC, then MMC must act as a sensor for volume regulation. To resolve this, we investigated the cytoplasmic MMC in cells seeded on surfaces that either promote (Fibronectin) or inhibit (10% PEG) cell spreading. Even after 2 hours of seeding, the cytoplasmic MMC in cells with compromised spreading is significantly higher than the well-spread cells (**Figure 4.5-A, 4.5-B**), establishing that increased cytoplasmic MMC does not trigger volume regulation in cells whose spreading is restricted. Cell spreading induces a significant decrease in the average cytoplasmic MMC, causing a 5.4% change in cytoplasmic viscosity (as further suggested by FRAP, η = 4.87 ± 1.15 cP for cells on Fibronectin, η = 7.5 ± 2.06 cP for cells on 10%PEG) (**Figure 4.5-C**).

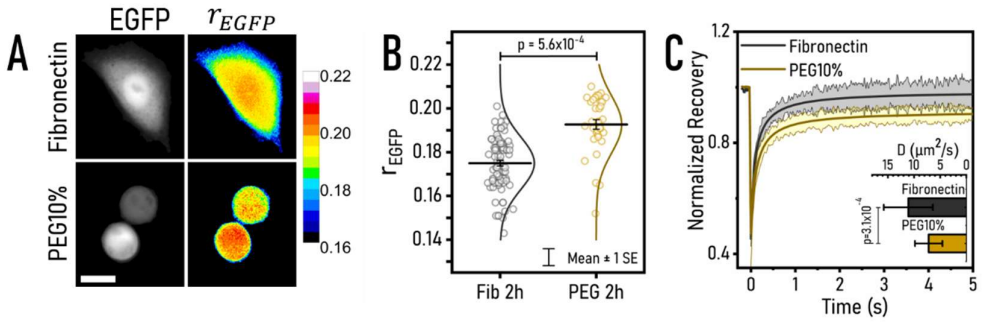

Figure 4. 5: (**A**) Representative NIH/3T3-EGFP seeded on fibronectin or 10%PEG coated glass 2 hours prior r_{EGFP} imaging. Scale bar = 10 μm. (**B**) r_{EGFP} of the cell population described in (**A**) with the mean and standard error depicted by the black horizontal lines. (**C**) FRAP in the cells described in (**A**) shows that the cytoplasmic viscosity experienced by EGFP is significantly increased in cells with restricted spreading (N=23 cells).

4.2.3. RAW 264.7 macrophages undergo a decrease in intracellular MMC upon treatment with PMA

PMA (phorbol 12-myristate 13-acetate) is known [173] to cause monocytes to undergo differentiation into macrophages. The murine macrophage cell line RAW 264.7 exists as a mix of low-adhering monocytes and highly adherent macrophages. PMA treatment in high concentrations induces the nuclear

translocation of NFκβ [174], and NFκβ is a key promoter of differentiation [175]. We measured r_{EGFP} in RAW264.7 transfected with EGFP before and after PMA (1 µM, 3 h) and observe a significant decrease in r_{EGFP} and an associated increase in the morphological spreading of the cells. The inverse relationship of the average r_{EGFP} of a cell and the spread area is similar to cell spreading post adhesion, with both phenomena occurring under isotonic conditions.

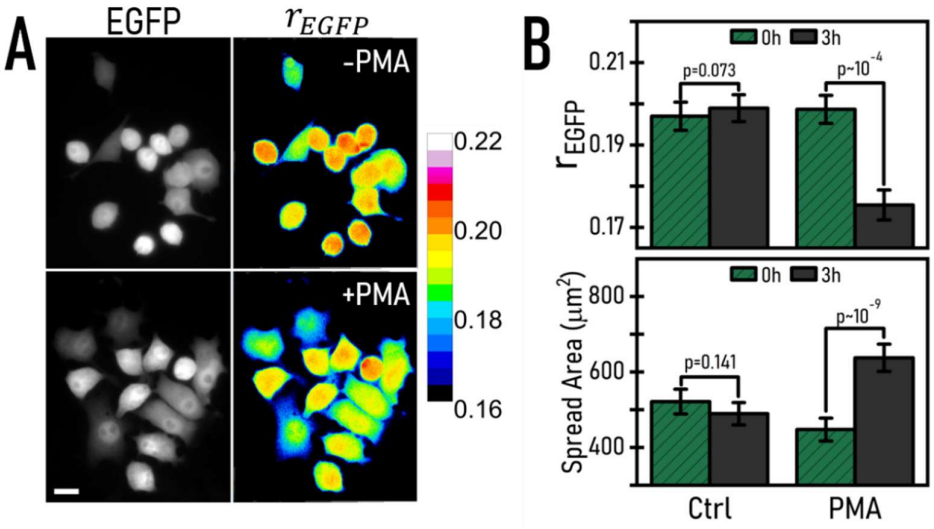

Figure 4. 6: Representative RAW 264.7 cells expressing EGFP before and after treatment with PMA (1 µM, 3 h) to induce differentiation are shown in (**A**). Scale bar = 15 µm. An increase in spreading area and a decrease in r_{EGFP} is observed for the PMA treated cells in comparison with the control group, as depicted in (**B**). N = 128 cells for control, 144 cells for PMA treatment.

4.2.4. Increased r_{EGFP} upon de-adhesion is a consequence of actin depolymerization

However, by inducing a rapid cell area contraction with exposure to Trypsin/EDTA, we observe an insignificant change in the cell volume between the spread state or 30min after trypsinization in NIH/3T3-EGFP (**Figure 4.7-A**), suggesting that contraction of cell spread area within few minutes do not maintain the same $V - A$ relation as in **Figure 4.7-A-inset**.

Yet, we find a measurable increase in cytoplasmic MMC during cell area contraction (**Figure 4.7-A-main**), presumably because of the mass depolymerization of cytoskeletal filaments to monomers, as we observe for actin (**Figure 4.7-B**) and according to previous reports for microtubules [176]. To test this hypothesis, we pre-disassembled the actin filaments using Cytochalasin D and then initiated cell area contraction by trypsin treatment in NIH/3T3-EGFP. Expectedly, the trypsinization-induced rise of r_{EGFP} is significantly less in Cytochalasin D pretreated cells when compared to untreated NIH/3T3-EGFP (**Figure 4.7-C**).

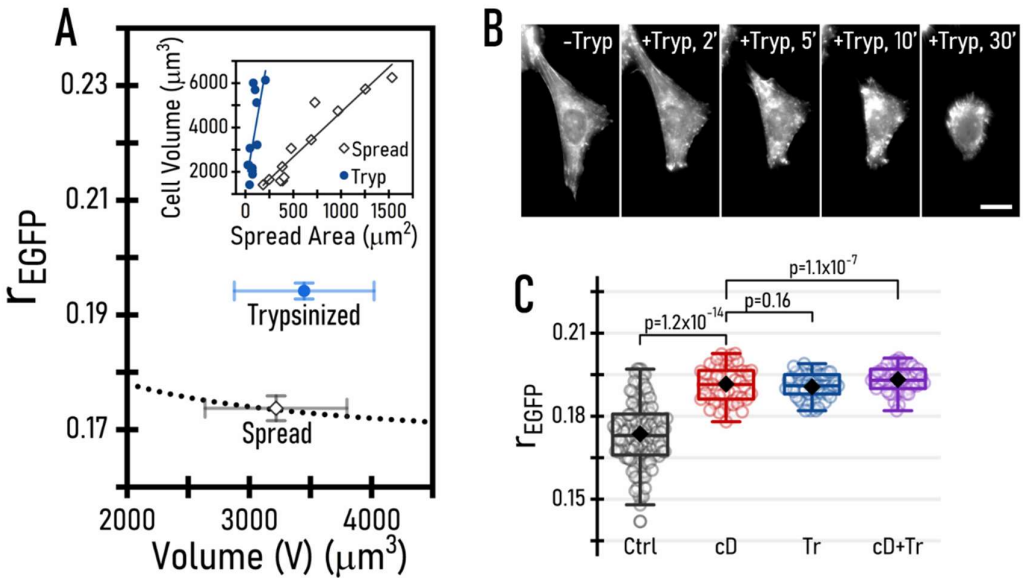

Figure 4. 7: (**A**) Change in r_{EGFP} and cell volume upon trypsinization does not fall on the expected trendline as described in **Figure 4.1-A**. Measuring the spread area and volume of the same cells pre- and post-30 mins of trypsinization shows that cell volume is not altered significantly (inset), however, r_{EGFP} increases substantialy. (**B**) Maximum intensity projection of Z-stacks for a representative NIH/3T3 cell expressing LifeAct-EGFP shows the gradual depolymerization of actin filamnets. (**C**) The increase in r_{EGFP} upon trypsinization in untreated cells (between Ctrl- gray and Tr- blue) and cytochalasin D (between Ctrl-gray to cD+Tr- purple) treated cells is similar. Cytochalasin D treatment (cD- red) itself increases r_{EGFP} significantly.

4.3. Zafirlukast inhibits cell volume regulation

4.3.1. Changes in cell volume and associated r_{EGFP} are not in tandem for hypertonic shock and cytoskeletal disruption

The cell volume regulatory apparatus can be decomposed into three principal modes- (i) the cell volume sensor- responsible for detecting changes in volume; (ii) the signal transmitter- responsible for receiving the volume change signal and propagating the information, such as intracellular signaling cascades; and (iii) the volume regulatory action- responsible for reacting to the transmitted signal and initiating responses to reset the cell volume to the pre-volume perturbation set-point. Regulatory volume change during osmotic imbalance involves the exchange of organic and inorganic osmolytes [77,148], which are smaller in size than the macromolecular crowders. Thus, there can be two possibly distinct features that could act as a volume sensor. 1) chemical signal, i.e., change in the cytoplasmic MMC that alters the thermodynamic activity of the cytoplasmic biochemistry via excluded volume effect, and 2) mechanical signal, i.e., change in the mechanical properties of the membrane/cytoskeleton that alters the intracellular levels of osmolyte for enforcing regulatory volume change. Previous reports [63] proposed that the altered cytoplasmic MMC in hypertonic conditions acts as a sensor for volume regulation in RBC cells, suggesting that cells sense their volume through changes in the cytoplasm's thermodynamic activity. These studies do not rule out the possibility that altered levels of smaller-sized osmolytes like ions or amino acids, which has a negligible effect on the thermodynamic activity, could also be the sensor for cellular volume regulation during RVI. To identify whether cytoplasmic MMC acts as a volume sensor for the cell, we performed experiments that changed the cytoplasmic MMC without altering the levels of intracellular smaller-sized osmolytes. Hypertonic conditions involve the exchange of osmolytes [74] and the non-specific aggregation of proteins (**Figure 4.3**). As a

result, the clustering of cytoplasmic proteins causes r_{EGFP} to rise above the expected curve (dotted line) in **Figure 4.8-A**. Since Heclin treatment leads to an increase in r_{EGFP}, whereas Cycloheximide treatment or heat shock causes no change or reduces r_{EGFP} (**Figure 3.11-A**), we investigated if the changes in r_{EGFP} under these conditions are due to a change in crowder concentration or protein clustering. **Figure 4.3-B** shows no visible clustering of cytoplasmic proteins in response to Heclin treatment. Thus, we conclude that Heclin treatment leads to a rise in cytoplasmic MMC. Next, we investigated whether the increase in cytoplasmic MMC in Heclin-treated cells triggers volume regulation. **Figure 4.8-B** shows no noticeable change in cell volume in response to increased (Heclin) or decreased (Cycloheximide) cytoplasmic MMC, demonstrating that changes in MMC in NIH/3T3 fibroblasts do not trigger cell volume regulation even until 4 hours of treatment. Since the cytoskeleton is the crucial component of the cell that decides its shape, we next investigated its role in determining cell volume and cytoplasmic MMC. Disassembly of actin causes no noticeable change in cell volume; however, the cytoplasmic MMC increases (**Figure 4.8-C**). Since actin is one of the most abundant cytoplasmic proteins, disruption of actin filaments leads to a significant increase in macromolecular crowder in the form of monomeric G-actin compared to microtubules. The intracellular concentration of actin is ~100 μM [177], while that of tubulin is ~2 μM [164]. Thus, the rise in cytoplasmic MMC is not proportional to the associated volume change for cytochalasin D treatment (**Figure 4.8-C**). However, depolymerizing microtubules through nocodazole treatment causes a significant increase in cell volume (**Figure 4.8-C**). The associated decrease in MMC is proportional to the increase in cell volume, indicating that cell volume increases in tandem with the increase of cytoplasmic MMC caused by nocodazole treatment.

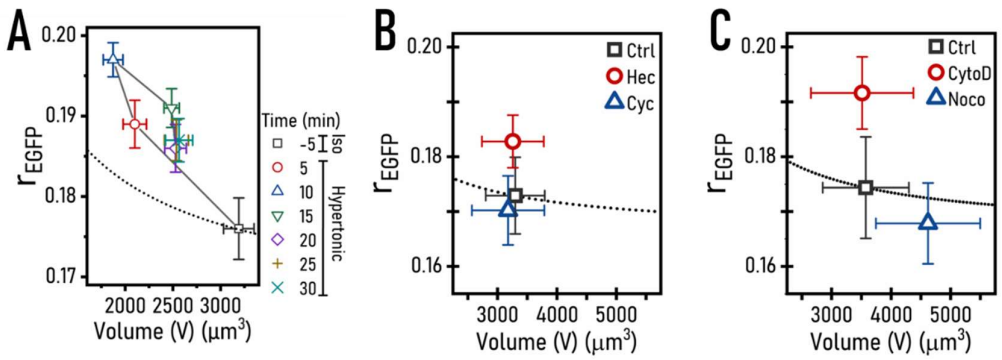

Figure 4. 8: (**A**) Trajectory of r_{EGFP} vs. cell volume at different time points after inducing hypertonic shock (+150 mM dextrose). N = 17 cells. (**B**) r_{EGFP} vs. cell volume after treatment with Heclin (70µM,4h) and Cycloheximide (1µM,4h) with respect to control in NIH/3T3-EGFP. N = 42 cells. (**C**) r_{EGFP} vs. cell volume after treatment with Cytochalasin D (2µM,1h) and Nocodazole (20µM,1h) with respect to control in NIH/3T3-EGFP. N = 38 cells. The dotted line in each graph denotes the expected trendline for cell volume and associated r_{EGFP} as described in **Figure 4.1-A**.

4.3.2. Pharmacological inhibition of TNFR1 by Zafirlukast abrogates cell volume regulation

Changes in cell volume simultaneously perturb plasma membrane organization [74]. To investigate the role of the plasma membrane behind cell volume regulation, we postulate the involvement of TNFR1 (Tumour Necrosis Factor Receptor 1), as it is reported to exhibit enhanced clustering and internalization during hypertonic stress [178]. TNFR1 is also known to localize in membrane caveolae [179,180], and caveolae are the excess membrane folds responsible for mitigating membrane tension imbalances [74,84]. Moreover, TNFR1 is upstream of NFκβ, which shows enhanced activity during hypertonic stress after 3-5h of stress induction [181,182]. Zafirlukast, a cysteinyl leukotriene antagonist [183], is reported to inhibit TNFR1 clustering [184]. Zafirlukast treatment abrogates RVI in NIH/3T3 in response to a hypertonic shock of an excess of 150 mM dextrose (**Figure 4.9-A**). In addition, Zafirlukast treatment leads to the arrest of cell volume regulatory activity during spreading (**Figure 4.9-B)** and microtubule depolymerized state (**Figure 4.9-C**).

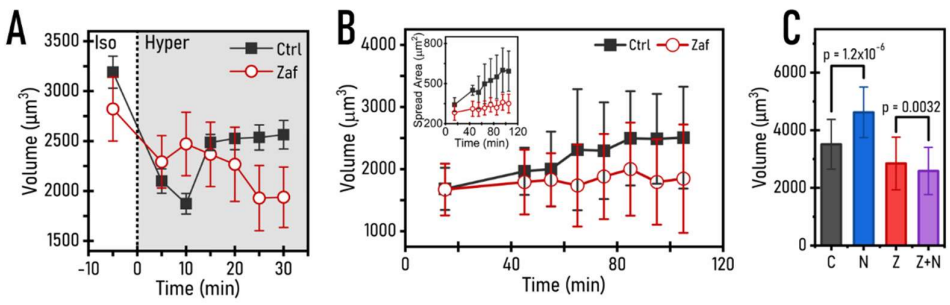

Figure 4. 9: (**A**) Mean cell volume trajectory in control and Zafirlukast (50μM,1h) treated NIH/3T3 in response to hypertonic shock (+150mM dextrose, gray region). N = 64 cells. (**B**) Mean cell volume trajectory (main) and corresponding spread area trajectory (inset) for control and Zafirlukast (50μM,1h) treated NIH/3T3 spreading on Fibronectin coated glass. N = 57 cells. (**C**) Comparison of cell volume in response to Nocodazole (20μM,1h) treatment in control (denoted C and N) and Zafirlukast (50μM,1h) treated (denoted Z and Z+N) NIH/3T3. Error bars represent standard deviation in all graphs.

4.3.3. Plasma membrane tension acts as a sensor of cell volume

To understand the effect of Zafirlukast treatment on the plasma membrane, we compared the membrane-fluctuation tension of control cells with that of Zafirlukast treated using interference reflection microscopy (IRM) (**Figure 4.10-A**) [185]. Membrane-fluctuation tension closely follows membrane frame tension for an extensive range of tension values [186]. **Figures 4.10-B** and **C** show that Zafirlukast treatment causes a rise in membrane tension. The amplitude of temporal fluctuations is decreased in cells treated with Zafirlukast (**Figure 4.10-B**). Thus, the increased membrane tension (**Figure 4.10-C**) deprives cells of their ability to trigger regulatory volume change in hypertonic, spreading, and microtubule depolymerized states.

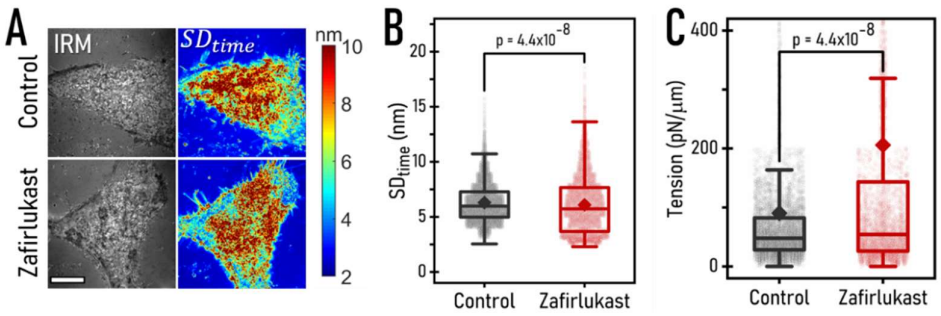

Figure 4. 10: (**A**) Representative Interference Reflection Microscopy images and corresponding SD_{time} maps of vehicle control (DMSO) and Zafirlukast treated cells. Scale bar=10µm. (**B-C**) Comparison of SD_{time} of membrane-fluctuation (**B**) and tension (**C**) in vehicle control and Zafirlukast treated cells. (Control=6880 FBRs, 13 cells; Zafirlukast=4514 FBRs, 10 cells).

4.4. Materials and methods

4.4.1. Cell culture and pharmacological studies

NIH/3T3 cell line was procured from NCCS (National Center for Cell Science, Pune, India). Fugene® (Promega) was used to transfect cells with the following plasmids: pCAG-mGFP, a gift from Connie Cepko (Addgene plasmid # 14757); mCherry-Lifeact-7, a gift from Michael Davidson (Addgene plasmid # 54491); and EGFP-p65, a gift from Johannes A. Schmid (Addgene plasmid # 111190), following standard protocol. Cells cultured in DMEM (Himedia, #AI007G) at 37℃, 5% CO_2 in a humidified incubator, were seeded on custom-made glass bottom 35mm petridishes. The glass was coated with 50mg/mL Fibronectin (Sigma, #F1141) to promote rapid adhesion and proper spreading, or with 10% PEG (Polyethylene glycol 1000, Sigma #81189) to arrest spreading in the appropriate cases. Before microscopy, cells were gently washed with 1xPBS twice, and culture media was replaced with phenol red-free DMEM (Gibco, #21063029), which could

be supplemented with the required drug when necessary. For all pharmacological treatments, Cytochalasin D (Merck, #C8273), Nocodazole (Merck, #487928), Heclin (Tocris, #5433), Cycloheximide (Sigma, #18079), and Zafirlukast (Merck, #Z4152) were dissolved in DMSO, and working concentrations were reconstituted as indicated in appropriate places. For applying heat shock, cells were incubated at 42℃ for 1h in the presence of 5% CO_2. To create osmotic imbalance, cells were first imaged in an isotonic complete medium, and then the culture media was replaced with either hypertonic or hypotonic complete medium using a custom-made flow system. Hypertonic media was prepared by adding Dextrose to phenol red-free DMEM at indicated concentrations and filtered for decontamination.

4.4.2. r_{EGFP} measurement

Same as **Section 3.5.2** of this dissertation.

4.4.3. Cell volume measurement

Cells were imaged using the Zeiss LSM 780 light scanning confocal system using a 63x oil immersion objective. Z-stack images of 0.4µm step size were taken using the AiryScan super-resolution mode to measure the whole cell volume. The whole Z-stack was binarized by an intensity threshold to mark the pixels containing cells as white and the background as black. Then, upon counting the number of white pixels contained in the binary Z-stack and multiplying the resultant with the appropriate voxel dimensions, the volume of the cells was calculated. Statistics of at least 10 cells were collected for plotting.

4.4.4. Fluorescence Recovery After Photobleaching (FRAP)

Same as **Section 3.5.3** of this dissertation.

4.4.5. Interference Reflection Microscopy

An inverted microscope (Nikon, Tokyo, Japan) with adjustable field and aperture diaphragms, 60x Plan Apo (NA 1.22, water immersion) with 1.5x external magnification, 100 W mercury arc lamp, (546 ± 12 nm) interference filter, 50:50 beam splitter, and CMOS (ORCA Flash 4.0 Hamamatsu, Japan) camera were used for IRM. Fast time-lapse images of cells were taken at 20 frames per second, and a total of 2048 frames were captured. Membrane fluctuations are quantified for regions within ~100 nm of the coverslip and termed First Branch Regions (FBRs). Calibration, identification of FBRs, and quantification of fluctuation amplitude (SD_{time}) and tension were done as previously reported [185].

4.5. Discussion

The cell is a closed system for macromolecules as free exchange with the extracellular environment is either not permitted or selectively permitted. Thus cell volume and intracellular MMC are reciprocally related, and the measurement of r_{EGFP} and cell volume allows us to investigate the role of cytoplasmic MMC as a sensor of cell volume. We find that heat-shock, trypsin-induced contraction, and treatment of Cytochalasin D, Heclin, or Cycloheximide shift the MMC in the cytoplasm without any change in cell volume. These observations establish that cells lack the ability for homeostasis of cytoplasmic MMC in isotonic conditions. Though the shift in MMC can alter a host of biochemical processes in the cytoplasm, NIH/3T3 fibroblasts lack the capabilities to regulate it. Imbalance in extracellular osmolarity is known to trigger RVI/RVD. We have identified additional conditions not linked to osmolarity shift, such as the morphological spreading of cells and microtubule depolymerization, in which cells invoke volume change autonomously. In these conditions, cells enforce volume changes, disregarding cytoplasmic MMC changes. Overall, our

observations indicate that cells do not use MMC as a sensor for cell volume. We have further identified that the inactivation of TNFR1 with Zafirlukast abrogates cellular ability for volume regulation. Having ruled out the role of cytoplasmic MMC as a sensor for cell volume, we studied the plasma membrane's mechanical state (tension) in Zafirlukast treated cells. Zafirlukast treatment causes an increase in membrane tension and abolishes the ability of the cells to regulate their volume. Thus, we can conclusively rule out the role of cytoplasmic MMC as a cell volume sensor. Instead, we believe that membrane tension has a more relevant role in activating the cell volume regulatory apparatus in NIH/3T3 cells.

Chapter 5: The influence of adherent cell morphology on cytoplasmic microrheology and intracellular oxidative stress

Adherent cells typically exhibit a wide range of morphologies that are unique to the source tissue and cell function. Further, they also possess different cytoskeletal organizations, focal adhesion dynamics, nucleus/cell volume ratio, lamellipodial protrusions, and so on. Cells also have different migration speeds and cell cycle duration. Within the variabilities, cell spreading on adhesion-promoting substrates is a common characteristic of all adherent cells. Adhesion is essential for all such cell types for survival, and lack of adhesion to compliant extracellular matrix drives the cells to a form of apoptosis called anoikis [187]. While non-cancerous cells may perish when deprived of anchorage, cancer cells can resist anoikis and metastasize [188–190]. Oxidative stress upon lack of adhesion points has been indicated to be the primary factor leading to anoikis [191,192]. Loss of integrin function and integrin-mediated anchorage to the extracellular substrate has been identified to be the leading cause of intracellular ROS (Reactive Oxygen Species) elevation. Rabbit synovial fibroblasts have been shown to possess elevated intracellular ROS levels upon blocking integrin function using the anti-α5 antibody [193], while endothelial cells have been shown to undergo oxidative stress-induced anoikis upon trypsin-mediated detachment from the extracellular matrix [116]. Even loss of integrin function due to simple mechanical unloading of the extracellular matrix has been implicated to trigger anoikis in fibroblasts [194].

In previous observations, we found that trypsin-mediated detachment of NIH/3T3 fibroblasts from adhesion-promoting substrates increased the

intracellular macromolecular crowding (**Figure 4.7-A**) while the volume of the cells remained relatively unchanged. Further, re-plating the cells on adhesion-promoting substrates led the cells to spread and reduce the intracellular macromolecular crowding (**Figure 4.4**). However, cells maintained the increased intracellular macromolecular crowding when cell spreading was arrested post adhesion to a compliant substrate, and the cytoplasmic viscosity increased (**Figure 4.5**). We were curious whether the emergence of anoikis had a role in preventing the cells from regulating their volume and adjusting the intracellular macromolecule density. Hence we probed the intracellular ROS levels using H_2DCFDA (an OH^- indicator, a general gauge of oxidative stress) during the processes of cell detachment and cell spreading to probe the state of oxidative stress in the cell and whether alterations in the viscoelastic nature of the cytoplasm has a role in the lack of cell volume regulation observed during adhesion deprivation.

5.1. Cell adherence is reciprocally related to intracellular oxidative stress

NIH/3T3 fibroblasts are adherent in nature and functionally secrete the collagen matrix essential for creating connective tissues. To see whether NIH/3T3 fibroblasts also suffer from oxidative stress upon trypsinization, we loaded NIH/3T3 fibroblasts with 20 μM H_2DCFDA for 20 minutes, washed the excess H_2DCFDA, and then monitored the intracellular ROS levels through DCF fluorescence after promoting detachment using culture grade 0.25% trypsin/EDTA solution at 37 °C. We noticed a significantly higher rise in the intracellular ROS levels upon trypsin treatment (**Figure 5.1-A**, **B**) compared to the control population, hence we hypothesized that the NIH/3T3 fibroblasts might be embarking on anoikis in the same manner as reported for endothelial cells. However, further keeping the cells suspended in serum-free media, the ROS levels decrease, and the re-introduction of the suspended cells to adherent substrates further reduces the intracellular

ROS levels with progressing cell spreading post adhesion (**Figure 5.1-C**). Previous reports have indicated that there is a pulse of elevated intracellular ROS levels during the progression of NIH/3T3 adhesion (at ~40 minutes post cell seeding), and redox regulation of FAK (Focal Adhesion Kinase), non-muscle myosin, and β-actin during this pulse is essential for cells to functionally adhere on substrates [114,195]. However, the authors used NIH/3T3 cells serum-starved overnight for their studies. When we replicated our ROS measurements using NIH/3T3 cells serum-starved overnight, we found an identical elevation of ROS levels peaking at ~40 minutes post cell seeding. Peculiarly, this phenomenon is absent in un-starved cells, and cells have no difficulty in attaching to the adherent substrate and spreading. Since serum starvation also leads to cell cycle synchronization, the elevated levels of intracellular ROS at 40 minutes post seeding could appear more pronounced in serum-starved cells due to a synchronized outburst of ROS intrinsic to the cell cycle stage.

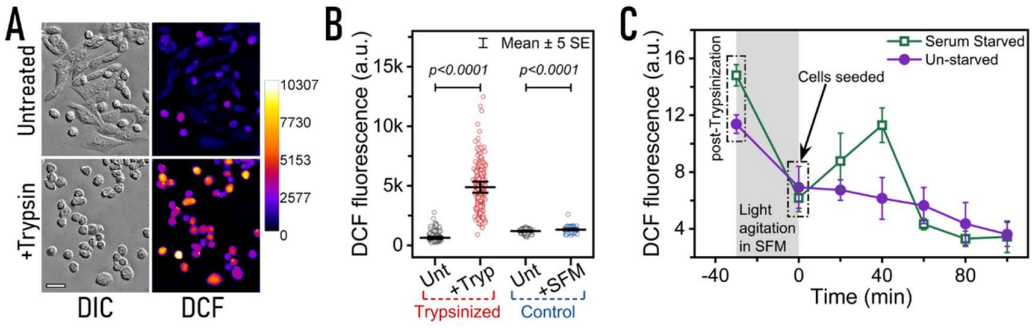

Figure 5. 1: (**A**) Representative images of NIH/3T3 fibrolasts stained with H_2DCFDA before and 10 minutes after trypsinization. The associated colorbar indiactes the intensity of DCF fluorescence. Scale bar = 30 µm. (**B**) Quantification of the mean intensity of DCF fluorescence per cell before and 10 minutes after trypsinization (red), or SFM addition (blue). Horizontal black lines represent the mean value and the standard error of mean multiplied by 5. N = 316 cells for the 'Trypsinized' group, N = 255 for the 'Control' group. (**C**) Evaluation of the intracellular oxidative stress levels post-trypsinization, immediately before seeding, and during cell spreading post seeding. The symbols at each time point indicate the average fluorescence intensity of triplicate measurements, while the error bars represent the standard deviation of the fluorescence intensities.

Experimental methodology for Figure 5.1-C:- NIH/3T3 fibroblasts were seeded on poly-l-lysine coated 60 mm dishes at a density of ~10^6 cells/dish. The cells were then extracted by trypsinization, and after pelleting the cells through centrifugation for 1 minute at 170g, the trypsin solution was decanted. The cell pellet was then resuspended in 2 mL of serum-free media and vortexed gently to obtain a uniform cell density. The whole process described above takes less than 5 minutes to complete. To evaluate the intracellular ROS levels at 10 minutes post-trypsinization, 200 µL of the cell suspension was taken out from the stock solution and deposited in one well (well #A1) of a poly-l-lysine 48-well plate. The rest of the cell suspension was deposited in a non-coated 35 mm polystyrene petridish (Tarsons, #460035) and placed atop a fastened smartphone kept in silent mode (calling the smartphone subjects the cells to gentle agitation due to the vibrating phone, thus preventing cell adhesion). At exactly 5 minutes after trypsinization, the cells in the well plate were loaded with 100 µL of SFM containing 60 µM H_2DCFDA and aspirated gently to obtain a uniform solution of 20 µM H_2DCFDA. At exactly 10 minutes after the time-point of trypsin addition, 500 µL of DMSO was added to the well to facilitate cell lysis. The cell suspension kept on the fastened smartphone inside the incubator was periodically subjected to gentle agitation every 2 minutes and after 25 minutes of incubation, another 200 µL of the cell suspension was taken out and deposited in a different well (well #A2) of the 48-well plate. This cell population was again loaded with 100 µL of SFM containing 60 µM H_2DCFDA, and after 5 minutes of incubation, the cells were lysed with 500 µL of DMSO. Finally, after spending a total of 30 minutes in the incubator, the leftover cell suspension was loaded into 5 different wells (well #A3-7) of the 48-well plate, with 200 µL of cell suspension in each well, and the cells were kept in standard culture conditions inside the incubator. Exactly 5 minutes before cell lysis (by 500 µL DMSO) for every measurement point depicted in **Figure 5.1-C**, 100 µL of SFM containing 60 µM H_2DCFDA was added to the relevant wells. The H_2DCFDA was not washed to prevent loss of cells and create a mismatch in the cell numbers for ROS measurement. The 48-well plate was kept in low-light conditions as much as possible to prevent spontaneous photoactivation of H_2DCFDA. Finally, at the 100

minutes time point, cell lysis was achieved at every well, and fluorescence of the DCF was measured using a SpectraMax M2e plate reader, with the last well of the row (well #A8) containing 500 µL DMSO and 300 µL SFM as the 'blank'. The average fluorescence intensity and the standard deviation of identically treated wells in three such experiments were plotted in **Figure 5.1-C**.

5.2. Restricting cell spreading induces oxidative stress and increases cytoplasmic viscoelasticity

In a population of NIH/3T3 fibroblasts seeded on glass for 24 hours and stained with 20 µM H_2DCFDA for 20 minutes, we observe that the cell spread area and the level of intracellular ROS are reciprocally related (**Figure 5.2-A**). While cell shape-dependent oxidative stress is a major probability [193,194,196], another possible explanation could be that cells with different spread areas might be at different cell cycle stages and the intracellular ROS levels could be a by-product of some cell cycle-dependent biological process [197,198]. To rule out the factor of the cell cycle stage, we synchronized the experimental NIH/3T3 population by serum-starving the cells overnight, then seeded the cells in adhesion promoting (fibronectin coating) or adhesion impeding (Poly-Ethylene Glycol coating) substrates. Expectedly, even in the cell cycle synchronized cells, the cells with restricted spreading (on PEG-coated glass substrate) had a higher ROS level than cells with enhanced spreading (on fibronectin-coated glass) (**Figure 5.2-B**). Our previous studies indicate that cells with higher intracellular ROS levels have a higher cytoplasmic stiffness [117], and cytoplasmic viscosity is also higher in the spreading restricted cells due to increased macromolecular crowding (**Figure 4.5**). To confirm, we ballistically injected 200 nm-sized fluorescent beads into NIH/3T3 fibroblasts, trypsinized the cells after an hour, then plated the cells on either fibronectin or PEG-coated glass (**Figure 5.2-C**). Then we measured the thermal fluctuation of the beads in the

cytoplasm to obtain information on the local microrheology. The cell nuclei were stained with Hoechst 33342 (1 µg/mL) so that beads located in the nucleoplasm can be excluded from the calculation of the rheological parameters. The slope of the average MSD of the 200 nm beads in the cytoplasm for cells adhering to fibronectin is steeper than that of cells seeded on PEG-coated glass (**Figure 5.2-D**), indicating that cells seeded on PEG have higher viscoelasticity than cells seeded on fibronectin. Computation of the elastic modulus (G') and the viscous modulus (G'') show that the cytoplasm of cells seeded on PEG-coated glass is more elastic and more viscous than the cytoplasm of cells seeded on fibronectin-coated glass at every vibrational mode of thermal fluctuations (**Figure 5.2-E, F**).

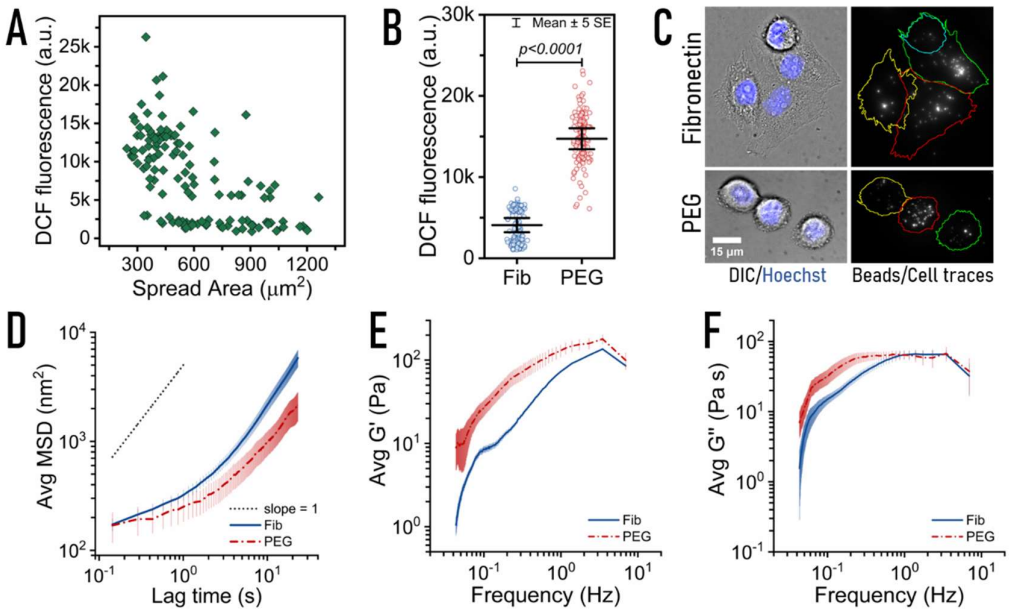

Figure 5. 2: (**A**) Mean intensity of DCF fluorescence per cell plotted against the cell spread area for NIH/3T3 fibroblasts (for H_2DCFDA- 20 µM, 20 mins). (**B**) Quantification of the mean intensity of DCF fluorescence per cell for NIH/3T3 fibroblasts (H_2DCFDA- 20 µM, 20 mins) seeded on fibronectin (20 µg/mL) or PEG (10% w/v) coated glass for 2 hours. (**C**) Representative images of NIH/3T3 fibroblasts seeded on fibronectin or PEG coated glass and ballistically injected with 200 nm fluorescent beads. (**D-F**) show the average MSD (mean-squared displacement), G' (elastic modulus), and G" (viscous modulus) obtained from the thermal fluctuations of the 200nm beads in the cytoplasm. Trace lines represent the mean quantity per cell and error bars represent the standard error of the mean for 28 cells in case of the fibronectin population and 22 cells in case of the PEG population.

5.3. Mechanical disruption of cell adhesion leads to elevation of intracellular oxidative stress

Trypsin is an enzyme that digests the integrins and other cell surface receptors, which leads to loss of cell anchorage and detachment from the substrate. The EDTA contained in the culture grade 0.25% trypsin/EDTA solutions is a chelator of divalent cations like Ca^{2+} and Mg^{2+}, which are essential for integrins to create stable anchorage. Thus, the advent of elevated intracellular ROS upon trypsinization could be a biochemical signal rather than a mechanical signal. Although it has been previously shown that cell detachment by mechanical unloading leads fibroblasts to apoptosis [194], we wanted to test whether mechanically induced cell detachment generates ROS in the same timescales as the biochemically induced cell detachment processes, like trypsinization. Hence, we loaded 20 μM H_2DCFDA into NIH/3T3 fibroblasts for 20 minutes, washed off the excess H_2DCFDA, and monitored the DCF fluorescence in cells poked with a glass capillary (**Figure 5.3-A**). We found a noticeable increase in DCF fluorescence in the cells with disrupted focal adhesions (as indicated by their shrinking area) compared to the undisturbed ones (**Figure 5.3-B**).

We were curious if similar mechanical stress can induce elevated ROS levels in the tissue level that do not have the same pattern of focal adhesion proteins as cultured cells. We dissected 1-day-old larvae of *Drosophila melanogaster* and extracted their salivary glands in 1xPBS. We loaded the salivary glands with H_2DCFDA (20 μM, 30 min) and monitored the ROS levels before, during, and after poking (**Figure 5.4**). The fat body attached to the salivary gland inherently has a high DCF fluorescence. However, the location of the salivary gland poked with the glass capillary shows enhanced DCF fluorescence after 15 minutes from the time of poking.

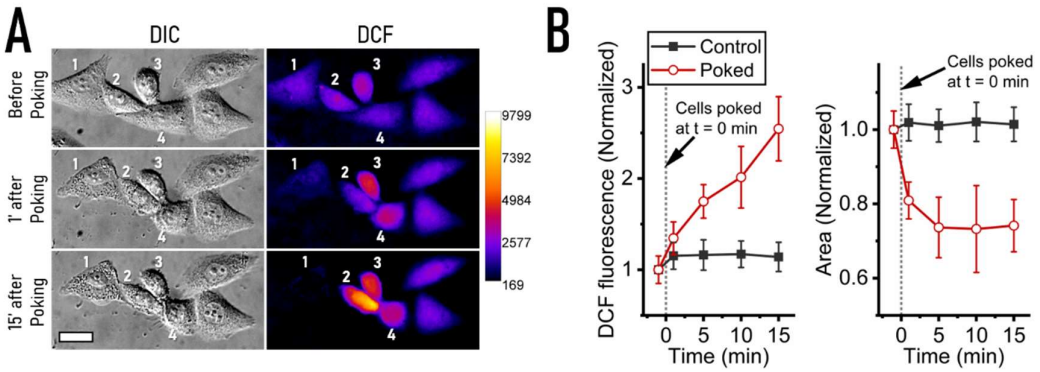

Figure 5. 3: (**A**) Representative NIH/3T3 fibrolasts stained with H_2DCFDA show increased oxidative stress upon mechanical disruption of cell adhesion. The numbered cells were poked with a fine glass capillary (diameter ~100 µm) by first lightly touching the cells and then moving the capillary forward by 1 µm. The capillary was made to approach the cells from the lower left corner of the representative images at a 45° angle from the horizontal While cell #1 is ruptured from excessive mechanical stress, cells #2-4 show rapid shrinkage of spread area while the DCF fluorescence increases. The unmarked cells were not poked and considered for the control group. Associated color bar indicates intensity of the DCF fluorescence. Scale bar = 20 µm. (**B**) Quantification of the DCF intensity and cell spread area of poked cells and their undisturbed control. Symbols indicate the average value of mean DCF intensity/cell normalized by the value of the first time point. Error bars indicate standard deviation of the normalized mean DCF intensity/cell values. N = 16 cells for the 'Poked' group and N = 53 cells for the 'Control' group.

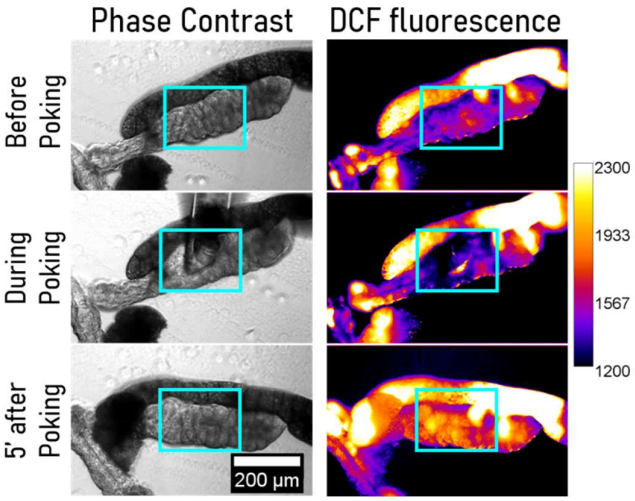

Figure 5. 4: Poking the salivary gland of drosophila larvae leads to elevated oxidative stress (cyan rectangles). Representative images depict the phase contrast and fluorescence micrographs of a salivary gland stained with H_2DCFDA (20 µM, 30 min) and imaged with a 10x objective. Associated color bar indicates DCF fluorescence intensity.

5.4. Discussion

From our experiments, it is clear that disturbing the anchor points of NIH/3T3 fibroblasts either biochemically (**Figure 5.1-A**) or mechanically (**Figure 5.3-A**) creates oxidative stress in the cells. Returning the cells to adhesion-promoting substrates rescues them from oxidative stress (**Figure 5.1-C**), but obstructing cell spreading does not mitigate the oxidative stress (**Figure 5.2-B**). **Figure 4.7-A** shows that the average volume of NIH/3T3 fibroblasts does not change appreciably upon trypsinization but the intracellular macromolecular crowding (MMC) rises significantly. Additionally, **Figure 4.7-B** shows that trypsinization ensues rapid actin disassembly, and previous reports indicate that microtubules also suffer rapid disassembly due to trypsinization [176]. Thus, a number of factors emerge that could potentially be leading the cells to oxidative stress upon anchorage depletion. Microtubule disassembly has been shown to induce excessive ROS in erythrocytes [199] and actin disassembly has been shown to create oxidative stress in different types of cells [200,201]. Another factor that could lead to the elevation of the intracellular ROS levels is the increased MMC upon trypsinization. To identify the cause of intracellular oxidative stress upon cell detachment, we must first locate the source of the ROS formation. Previous reports suggest that the immediate source of ROS upon cell detachment is the mitochondria [116]. However, the exact cause of the sudden elevation of mitochondrial ROS is still unknown. Another possible source of ROS could be the NADPH oxidase 2 (NOX-2) located on the membrane. The protein $p40^{phox}$ is known to localize with filamentous actin and also with NOX-2 [201]. Actin filament disruption releases $p40^{phox}$ from its bound form and increases its cytosolic fraction. Thus, $p40^{phox}$ can localize with NOX-2 and aid in its assembly, which subsequently increases the cytoplasmic ROS levels. As trypsinization also ensues actin filament disruption, the $p40^{phox}$ pathway to ROS elevation is a strong possibility. Further, **Figure 4.8-C** shows that microtubule disruption with nocodazole leads to cell volume increase, but f-actin disruption through cytochalasin D treatment does not induce any

change in cell volume while the intracellular MMC rises. Interestingly, microtubule disruption leads to a ~34% increase in nuclear volume (data not shown) while f-actin disruption leads to insignificant change in nuclear volume. Whether the cell volume increase observed within one hour of microtubule disruption is correlated with the increase in nuclear size is unclear from these preliminary experiments, but previous studies [202–204] indicate that tension in the nuclear membrane could be a driving factor behind the cell volume increase. Similarly, trypsinized cells do not undergo any change in cell volume but have a higher intracellular MMC. A question arises whether the enhanced intracellular ROS could be responsible for arresting cell volume regulation to counterbalance the rise in cytoplasmic MMC. We are still addressing these questions with new experiments.

Chapter 6: Summary

The cytoplasm is the reaction crucible for the chemistry of life. The aqueous microenvironment of the cytoplasm is crowded with proteins, nucleic acids, lipids, polysaccharides, and similar macromolecules. The macromolecules collectively occupy about 30% of the total cell volume [17]; thus, only 70% of the intracellular space is free for hosting biochemical reactions. The volume exclusion of the intracellular space increases the effective macromolecule concentration for a given cell; hence, interaction probability between macromolecules rises, resulting in accelerated reaction kinetics and self-association. The increased interactions also hinder a macromolecule's movement in the cell, thus contradictorily decreasing the effective chemical reactivity. This simultaneous enhancement of effective concentration and diminution of mobility results in the emergence of Macromolecular Crowding (MMC), which is an entropic phenomenon. Of late, the scientific community is vigorously scrutinizing MMC due to its undeniable role in numerous physiological and pathophysiological processes [34]. The current hypothesis envisages that physically, the cell is a closed system of macromolecules, which are not exchanged with the extracellular environment as rapidly as small molecules like ions and water. Thus the intracellular MMC should be reciprocal to the cell volume, and any perturbations in the cell volume should alter the cytoplasmic MMC enough to affect the reactivity of macromolecules like proteins and nucleic acids, which in turn makes a cell aware of its volume. Hence, one of the highly debated topics is the role of MMC in sensing cell volume [8–12].

Until the recent advent of FRET-based probes [50,52,205], there was a dearth of fast, high-throughput tools to quantify cytoplasmic MMC directly. However, studying FRET (Forster Resonance Energy Transfer) in the cytoplasm has drawbacks due to the interference from ionic interactions and pH conditions. A high-throughput, fast sensing probe that solely reacts to MMC could enable more thorough investigations of cytoplasmic MMC. Biologists

ubiquitously use EGFP (Enhanced Green Fluorescence Protein) as a probe for various studies owing to its inertness, photophysical stability, and ease of expression in the cell. We demonstrated that steady-state fluorescence anisotropy of EGFP (r_{EGFP}) is a reliable indicator of MMC, both *in vitro* and in the cytoplasm. The local MMC conditions around an EGFP determine the refractive index of the solution. The fluorescence lifetime of a fluorophore is related to the inverse square of the refractive index [133], while the electronic transition dipole moment of the fluorophore has a more non-trivial relation with the refractive index. Hence increased MMC conditions decrease the fluorescence lifetime of EGFP, while the intrinsic anisotropy, a property determined by the EGFP's transition dipole moment, scales proportionally with the local refractive index. Thus effectively, r_{EGFP} increases linearly with increasing MMC. According to the Perrin equation for fluorescence anisotropy [122], the fluorescence lifetime of EGFP is significantly smaller than the rotational correlation time. Thus, r_{EGFP} is more susceptible to changes in its fluorescence lifetime than the solution viscosity [141]. As the solution refractive index increases monotonically with protein density [136], and since proteins are the maximum contributors of cytoplasmic MMC, the fluorescence lifetime and concurrently, r_{EGFP} is highly sensitive to protein concentration in the solution. We demonstrated the linearity and broad range of sensing capacity of r_{EGFP} in BSA (Bovine Serum Albumin) and polysucrose solutions with purified EGFP in salt buffers and validated our observations with fluorescence lifetime measurements under the same conditions. We also observed a linear increment in the intrinsic anisotropy of EGFP, which could arise from a decrease in the transition dipole moment angle. We further showed that small molecules like amino acids and inorganic salts fail to induce sufficient change in r_{EGFP} at physiological concentrations, thus making r_{EGFP} a probe of crowding in the true sense of a macromolecule. The pH and self-concentration insensitivity of r_{EGFP} are also positive factors supporting r_{EGFP}'s inertness to cytoplasmic factors other than MMC. Our observations establish that r_{EGFP} is a good semi-quantitative indicator of cytoplasmic MMC.

We transiently expressed free, monomeric EGFP in different cell types and measured r_{EGFP} to map the cytoplasmic MMC levels. Different cell lines maintain noticeably unique levels of their respective average cytoplasmic MMC. Our measurements indicate that cytoplasmic MMC is spatially heterogeneous, despite the free diffusibility of cytoplasmic proteins. While the lamellipodial cytoplasm is less crowded, the perinuclear cytoplasm has significantly greater MMC. We observed similar MMC distributions in fluorescence lifetime maps of cytoplasmic EGFP. However, the average cytoplasmic MMC in a given cell is stable temporally for long durations. We validated the spatial inhomogeneity of MMC by measuring cytoplasmic viscosity with two different methods, which we independently assembled and calibrated- FRAP (Fluorescence Recovery After Photobleaching) and SPT (Single Particle Tracking). We find that the resistance offered to free diffusion is probe-size dependent. While the mobility of EGFP is scarcely affected by MMC, the mobility of fluorescent microspheres 100 times the size of EGFP is about 70% more sensitive to local MMC conditions. We also find that the actin cytoskeleton polices the heterogeneous distribution of MMC in the cytoplasm, as disruption of filamentous actin homogenizes the cytoplasmic MMC. Disruption of the microtubule and vimentin networks has no noticeable effect on the distribution of cytoplasmic MMC.

Osmotic challenges enforce water efflux/influx in cells, altering cytoplasmic MMC. Through r_{EGFP} measurements, we can monitor the cytoplasm responding and adapting to both hypertonic and hypotonic shocks. Cellular adaptation to osmotic challenges involves balancing the intracellular and extracellular osmolarity by osmolyte exchange and cell volume adjustment, which we independently validate. We find that lamellipodial regions expel more water during hypertonic challenges, possibly due to a higher abundance of aquaporins. Unlike epithelial carcinomas (HeLa, MDA-MB-237) and fibroblasts (NIH/3T3), the macrophage cell line RAW264.7 does not recover from dextrose-supplemented hypertonic shocks. Super-resolution imaging of cytosolic EGFP revealed that hypertonic shocks induce rapid and widespread protein condensation in cells. NFκβ (Nuclear

Factor κβ), a protein with DNA binding domains, forms spherical droplets during hypertonic challenges. The non-specific protein aggregation in the cytoplasm allows cells to deviate from the Normality equation when challenged with hypertonicity. While osmotic shocks alter the intracellular MMC through water exchange, we devised experiments that change the intracellular protein concentrations under isotonic conditions. Surprisingly, we did not observe any volume regulatory behavior when protein densities increase or decrease in the cytoplasm, even when cells have sufficient time to shift the intracellular osmolarity. There is also no visible non-specific protein aggregation, as in the case of hypertonic challenges. However, NFκβ forms large aggregates whose appearance differs significantly from the condensates observed during hypertonic shocks. Additionally, the elevation of MMC by increasing cytoplasmic protein density upshifts the intrinsic MMC to a new set-point in the cell, such as recovery from hypertonic shock does not return the MMC levels to the set-point before the protein density was artificially increased.

Cell volume and cytoplasmic MMC significantly change with increasing spread area of NIH/3T3 fibroblasts. Cell spread area is proportional to cell volume during and after the cell has completely spread. Cytoplasmic MMC is expectedly inversely proportional to cell volume/area. However, in the reverse case of cell area contraction (by trypsinization), cell volume changes insignificantly, while cytoplasmic MMC increases appreciably. We observe similarly elevated MMC levels upon restricting cell spreading while promoting more spreading reduces MMC. We also find that the elevation/demotion of MMC levels during cell contraction/spreading are accompanied by a concomitant change in the cytoplasmic ROS (Reactive Oxygen Species) levels and microrheology. This interplay between MMC, ROS, and microrheology of the cytoplasm could result from the forces suffered by the cytoskeletal components during cell spread area change. Disruption of filamentous actin does not cause a significant difference in cell volume, but a considerable upshift in MMC occurs. Disruption of microtubules causes a substantial increase in cell volume, but there is no

appreciable change in MMC. During trypsinization, both F-actin and microtubules depolymerize, and actin being one of the most abundant proteins in the cell, could be the critical crowder that elevates MMC and microrheology in the cytoplasm.

Since we observe that while certain conditions can invoke a cell volume change autonomously, other states can shift MMC in the cytoplasm without inducing any change in cell volume. Hence we concluded that cells lack the ability for cytoplasmic MMC homeostasis and cells can enforce volume changes disregarding the cytoplasmic MMC changes. Overall, our findings indicate that MMC does not act as a sensor for autonomous cell volume regulation. After ruling out the role of cytoplasmic MMC in cell volume regulation, we investigated the role of the plasma membrane's mechanical state (tension) in cell volume regulation. We identified TNFR1 (Tumour Necrosis Factor Receptor 1), a transmembrane protein, as a vital component essential for invoking cell volume regulation. Pharmacological inactivation of TNFR1 increased membrane tension and abrogated cell volume regulation in every condition we investigated. We can conclusively say that, in comparison to intracellular MMC, the plasma membrane plays a more crucial role in activating the cell volume regulatory apparatus.

We then investigated if the cell volume and cell morphology have any impact on the biochemical physiology of NIH/3T3 fibroblasts. We found that detaching cells from their adhesion points results in an elevation of intracellular reactive oxygen species (ROS) in the cytoplasm, while the reintroduction of adhesion-promoting substrates rescues the cells from oxidative stress. However, not allowing cells to spread after attachment makes the oxidative stress persist. The increased oxidative stress also makes the cells mechanically stiffer and the cytoplasm more viscous, as suggested by the data from particle tracking microrheology experiments. The effect of cytoplasmic microrheology and heightened oxidative stress on cell volume regulation during cell spreading is still under investigation.

Bibliography

1. Wozniak, M. A., Modzelewska, K., Kwong, L. & Keely, P. J. Focal adhesion regulation of cell behavior. *Biochimica et Biophysica Acta (BBA) - Molecular Cell Research* **1692**, 103–119 (2004).

2. Walpita, D. & Hay, E. D. Studying actin-dependent processes in tissue culture. *Nature Reviews Molecular Cell Biology 2002 3:2* **3**, 137–141 (2002).

3. Guo, M. *et al.* Cell volume change through water efflux impacts cell stiffness and stem cell fate. *Proc Natl Acad Sci U S A* **114**, E8618–E8627 (2017).

4. Hakkinen, K. M., Harunaga, J. S., Doyle, A. D. & Yamada, K. M. Direct Comparisons of the Morphology, Migration, Cell Adhesions, and Actin Cytoskeleton of Fibroblasts in Four Different Three-Dimensional Extracellular Matrices. *https://home.liebertpub.com/tea* **17**, 713–724 (2010).

5. Okada, Y., Sabirov, R. Z., Sato-Numata, K. & Numata, T. Cell Death Induction and Protection by Activation of Ubiquitously Expressed Anion/Cation Channels. Part 1: Roles of VSOR/VRAC in Cell Volume Regulation, Release of Double-Edged Signals and Apoptotic/Necrotic Cell Death. *Front Cell Dev Biol* **8**, 1776 (2021).

6. Okada, Y. & Maeno, E. Apoptosis, cell volume regulation and volume-regulatory chloride channels. *Comp Biochem Physiol A Mol Integr Physiol* **130**, 377–383 (2001).

7. Morishita, K., Watanabe, K. & Ichijo, H. Cell volume regulation in cancer cell migration driven by osmotic water flow. *Cancer Sci* **110**, 2337–2347 (2019).

8. Minton, A. P., Colclasure, G. C. & Parker, J. C. Model for the role of macromolecular crowding in regulation of cellular volume. *Proc Natl Acad Sci U S A* **89**, 10504–10506 (1992).

9. Al-Habori, M. Macromolecular crowding and its role as intracellular signalling of cell volume regulation. *Int J Biochem Cell Biol* **33**, 844–864 (2001).

10. Hoffmann, E. K., Lambert, I. H. & Pedersen, S. F. Physiology of cell volume regulation in vertebrates. *Physiol. Rev.* **89**, 193–277 (2009).

11. Watanabe, K., Umeda, T., Niwa, K., Naguro, I. & Ichijo, H. A PP6-ASK3 Module Coordinates the Bidirectional Cell Volume Regulation under Osmotic Stress. *Cell Rep* **22**, 2809–2817 (2018).

12. Delarue, M. *et al.* mTORC1 controls phase separation and the biophysical properties of the cytoplasm by tuning crowding. *Cell* **174**, 338-349.e20 (2018).

13. Burg, M. B. Macromolecular Crowding as a Cell VolumeSensor. *Cellular Physiology and Biochemistry* **10**, 251–256 (2000).

14. Model, M. A., Hollembeak, J. E. & Kurokawa, M. Macromolecular crowding: A hidden link between cell volume and everything else. *Cellular Physiology and Biochemistry* **55**, 25–40 (2021).

15. Kohata, K. & Miyoshi, D. RNA phase separation–mediated direction of molecular trafficking under conditions of molecular crowding. *Biophys Rev* **12**, 669–676 (2020).

16. Erickson, H. P. Size and Shape of Protein Molecules at the Nanometer Level Determined by Sedimentation, Gel Filtration, and Electron Microscopy. *Biol Proced Online* **11**, 32 (2009).

17. Yamamoto, J. *et al.* Quantitative evaluation of macromolecular crowding environment based on translational and rotational diffusion using polarization dependent fluorescence correlation spectroscopy. *Scientific Reports 2021 11:1* **11**, 1–11 (2021).

18. Speer, S. L., Stewart, C. J., Sapir, L., Harries, D. & Pielak, G. J. Macromolecular Crowding Is More than Hard-Core Repulsions. *https://doi.org/10.1146/annurev-biophys-091321-071829* **51**, (2022).

19. Minton, A. P. Excluded volume as a determinant of macromolecular structure and reactivity. *Biopolymers* **20**, 2093–2120 (1981).

20. Ralston, G. B. Effects of ‘crowding’ in protein solutions. *J Chem Educ* **67**, 857–860 (1990).

21. Willis, P. R., Nichol, L. W. & Siezen, R. J. The indefinite self-association of lysozyme: consideration of composition-dependent activity coefficients. *Biophys Chem* **11**, 71–82 (1980).

22. Vöpel, T. & Makhatadze, G. I. Enzyme Activity in the Crowded Milieu. *PLoS One* **7**, e39418 (2012).

23. Ma, B. & Nussinov, R. Structured crowding and its effects on enzyme catalysis. *Top Curr Chem* **337**, 123–138 (2013).

24. Ellis, R. J. Macromolecular crowding: obvious but underappreciated. *Trends Biochem Sci* **26**, 597–604 (2001).

25. Qin, S., Minh, D. D. L., McCammon, J. A. & Zhou, H. X. Method to predict crowding effects by postprocessing molecular dynamics trajectories: Application to the flap dynamics of HIV-1 protease. *Journal of Physical Chemistry Letters* **1**, 107–110 (2010).

26. Minh, D. D. L., Chang, C. E., Trylska, J., Tozzini, V. & McCammon, J. A. The influence of macromolecular crowding on HIV-1 protease internal dynamics. *J Am Chem Soc* **128**, 6006–6007 (2006).

27. Asakura, S. & Oosawa, F. Interaction between particles suspended in solutions of macromolecules. *Journal of Polymer Science* **33**, 183–192 (1958).

28. Asakura, S. & Oosawa, F. On Interaction between Two Bodies Immersed in a Solution of Macromolecules. *J Chem Phys* **22**, 1255 (2004).

29. Marenduzzo, D., Finan, K. & Cook, P. R. The depletion attraction: an underappreciated force driving cellular organization. *Journal of Cell Biology* **175**, 681–686 (2006).

30. André, A. A. M. & Spruijt, E. Liquid–Liquid Phase Separation in Crowded Environments. *International Journal of Molecular Sciences 2020, Vol. 21, Page 5908* **21**, 5908 (2020).

31. Shin, Y. & Brangwynne, C. P. Liquid phase condensation in cell physiology and disease. *Science (1979)* **357**, (2017).

32. Jalihal, A. P. *et al.* Hyperosmotic phase separation: Condensates beyond inclusions, granules and organelles. *Journal of Biological Chemistry* **296**, (2021).

33. Jalihal, A. P. *et al.* Multivalent Proteins Rapidly and Reversibly Phase-Separate upon Osmotic Cell Volume Change. *Mol Cell* **79**, 978-990.e5 (2020).

34. Mittal, S., Chowhan, R. K. & Singh, L. R. Macromolecular crowding: Macromolecules friend or foe. *Biochimica et Biophysica Acta (BBA) - General Subjects* **1850**, 1822–1831 (2015).

35. Soleimaninejad, H., Chen, M. Z., Lou, X., Smith, T. A. & Hong, Y. Measuring macromolecular crowding in cells through fluorescence anisotropy imaging with an AIE fluorogen. *Chemical Communications* **53**, 2874–2877 (2017).

36. Verkman, A. S. Solute and macromolecule diffusion in cellular aqueous compartments. *Trends Biochem Sci* **27**, 27–33 (2002).

37. Puchkov, E. O. Intracellular viscosity: Methods of measurement and role in metabolism. *Biochemistry (Moscow) Supplement Series A: Membrane and Cell Biology 2013 7:4* **7**, 270–279 (2013).

38. Luby-Phelps, K. Cytoarchitecture and Physical Properties of Cytoplasm: Volume, Viscosity, Diffusion, Intracellular Surface Area. *Int Rev Cytol* **192**, 189–221 (1999).

39. Kuimova, M. K., Yahioglu, G., Levitt, J. A. & Suhling, K. Molecular rotor measures viscosity of live cells via fluorescence lifetime imaging. *J Am Chem Soc* **130**, 6672–6673 (2008).

40. Liu, F. *et al.* Ratiometric Detection of Viscosity Using a Two-Photon Fluorescent Sensor. *Chemistry – A European Journal* **19**, 1548–1553 (2013).

41. Kuimova, M. K. *et al.* Imaging intracellular viscosity of a single cell during photoinduced cell death. *Nature Chemistry 2009 1:1* **1**, 69–73 (2009).

42. Miermont, A. *et al.* Severe osmotic compression triggers a slowdown of intracellular signaling, which can be explained by molecular crowding. *Proc Natl Acad Sci U S A* **110**, 5725–5730 (2013).

43. Swaminathan, R., Hoang, C. P. & Verkman, A. S. Photobleaching recovery and anisotropy decay of green fluorescent protein GFP-S65T in solution and cells: cytoplasmic viscosity probed by green fluorescent protein translational and rotational diffusion. *Biophys J* **72**, 1900–1907 (1997).

44. Kao, H. P., Abney, J. R. & Verkman, A. S. Determinants of the translational mobility of a small solute in cell cytoplasm. *Journal of Cell Biology* **120**, 175–184 (1993).

45. Guigas, G., Kalla, C. & Weiss, M. Probing the Nanoscale Viscoelasticity of Intracellular Fluids in Living Cells. *Biophys J* **93**, 316–323 (2007).

46. Fabry, B. *et al.* Scaling the microrheology of living cells. *Phys Rev Lett* **87**, 148102–148102 (2001).

47. Wong, I. Y. *et al.* Anomalous diffusion probes microstructure dynamics of entangled F-actin networks. *Phys Rev Lett* **92**, 178101 (2004).

48. Yadav, S., Shire, S. J. & Kalonia, D. S. Viscosity Analysis of High Concentration Bovine Serum Albumin Aqueous Solutions. *Pharmaceutical Research 2011 28:8* **28**, 1973–1983 (2011).

49. Gnutt, D. *et al.* Excluded-Volume Effects in Living Cells. *Angewandte Chemie International Edition* **54**, 2548–2551 (2015).

50. Boersma, A. J., Zuhorn, I. S. & Poolman, B. A sensor for quantification of macromolecular crowding in living cells. *Nature Methods 2015 12:3* **12**, 227–229 (2015).

51. Morikawa, T. J. *et al.* Dependence of fluorescent protein brightness on protein concentration in solution and enhancement of it. *Scientific Reports 2016 6:1* **6**, 1–13 (2016).

52. Murade, C. U. & Shubeita, G. T. A molecular sensor reveals differences in macromolecular crowding between the cytoplasm and nucleoplasm. *ACS Sens* **4**, 1835–1843 (2019).

53. Murade, C. U. & Shubeita, G. T. A molecular sensor reveals differences in macromolecular crowding between the cytoplasm and nucleoplasm. *ACS Sens* **4**, 1835–1843 (2019).

54. Kim, M. K. Digital holographic microscopy. *Springer Series in Optical Sciences* **162**, 149–190 (2011).

55. Marian, A. *et al.* Cell refractive index tomography by digital holographic microscopy. *Optics Letters, Vol. 31, Issue 2, pp. 178-180* **31**, 178–180 (2006).

56. Cheung, M. C., Evans, J. G., Mckenna, B. & Ehrlich, D. J. Deep ultraviolet mapping of intracellular protein and nucleic acid in femtograms per pixel. *Cytometry Part A* **79A**, 920–932 (2011).

57. Cheung, M. C. *et al.* Intracellular protein and nucleic acid measured in eight cell types using deep-ultraviolet mass mapping. *Cytometry Part A* **83A**, 540–551 (2013).

58. Kim, T. *et al.* White-light diffraction tomography of unlabelled live cells. *Nature Photonics 2014 8:3* **8**, 256–263 (2014).

59. Yanase, Y. *et al.* Detection of refractive index changes in individual living cells by means of surface plasmon resonance imaging. *Biosens Bioelectron* **26**, 674–681 (2010).

60. Yanase, Y. *et al.* The SPR signal in living cells reflects changes other than the area of adhesion and the formation of cell constructions. *Biosens Bioelectron* **22**, 1081–1086 (2007).

61. Model, M. A. & Petruccelli, J. C. Intracellular Macromolecules in Cell Volume Control and Methods of Their Quantification. *Curr Top Membr* **81**, 237–289 (2018).

62. Parker, J. C. In defense of cell volume? *https://doi.org/10.1152/ajpcell.1993.265.5.C1191* **265**, (1993).

63. Dunham, P. B. Effects of urea on K-Cl cotransport in sheep red blood cells: evidence for two signals of swelling. *https://doi.org/10.1152/ajpcell.1995.268.4.C1026* **268**, (1995).

64. Sarma, P. R. Red Cell Indices. *Clinical Methods: The History, Physical, and Laboratory Examinations* **3rd editio**, (1990).

65. Koltsova, S. v. *et al.* Transcriptomic Changes Triggered by Hypoxia: Evidence for HIF-1α -Independent, [Na+]i/[K+]i-Mediated, Excitation-Transcription Coupling. *PLoS One* **9**, e110597 (2014).

66. Koltsova, S. v., Akimova, O. A., Kotelevtsev, S. v., Grygorczyk, R. & Orlov, S. N. Hyperosmotic and isosmotic shrinkage differentially affect protein phosphorylation and ion transport. *Can J Physiol Pharmacol* **90**, 209–217 (2012).

67. Kojima, R. *et al.* Hypertonicity-Induced Expression of Monocyte Chemoattractant Protein-1 through a Novel Cis-Acting Element and MAPK Signaling Pathways. *The Journal of Immunology* **184**, 5253–5262 (2010).

68. Naguro, I. *et al.* ASK3 responds to osmotic stress and regulates blood pressure by suppressing WNK1-SPAK/OSR1 signaling in the kidney. *Nat. Commun.* **3**, (2012).

69. de los Heros, P., Pacheco-Alvarez, D. & Gamba, G. Role of WNK Kinases in the Modulation of Cell Volume. *Curr Top Membr* **81**, 207–235 (2018).

70. Lambert, I. H., Hoffmann, E. K. & Pedersen, S. F. Cell volume regulation: physiology and pathophysiology. *Acta Physiologica* **194**, 255–282 (2008).

71. Carafoli, E. Calcium signaling: A tale for all seasons. *Proc Natl Acad Sci U S A* **99**, 1115–1122 (2002).

72. Lang, F. *et al.* Functional significance of cell volume regulatory mechanisms. *Physiol Rev* **78**, 247–306 (1998).

73. Lang, F. Mechanisms and Significance of Cell Volume Regulation. *https://doi.org/10.1080/07315724.2007.10719667* **26**, 613S-623S (2013).

74. Roffay, C. *et al.* Passive coupling of membrane tension and cell volume during active response of cells to osmosis. *Proc Natl Acad Sci U S A* **118**, (2021).

75. Deneka, D. *et al.* Allosteric modulation of LRRC8 channels by targeting their cytoplasmic domains. *Nature Communications 2021 12:1* **12**, 1–14 (2021).

76. Qiu, Z. *et al.* SWELL1, a Plasma Membrane Protein, Is an Essential Component of Volume-Regulated Anion Channel. *Cell* **157**, 447–458 (2014).

77. Jentsch, T. J. VRACs and other ion channels and transporters in the regulation of cell volume and beyond. *Nat. Rev. Mol. Cell Biol.* **17**, 293–307 (2016).

78. le Roux, A. L., Quiroga, X., Walani, N., Arroyo, M. & Roca-Cusachs, P. The plasma membrane as a mechanochemical transducer. *Philos. Trans. R. Soc. Lond. B Biol. Sci.* **374**, 20180221 (2019).

79. Riggi, M. *et al.* Decrease in plasma membrane tension triggers PtdIns(4,5)P2 phase separation to inactivate TORC2. *Nat. Cell Biol.* **20**, 1043–1051 (2018).

80. Riggi, M., Kusmider, B. & Loewith, R. The flipside of the TOR coin - TORC2 and plasma membrane homeostasis at a glance. *J Cell Sci* **133**, jcs242040–jcs242040 (2020).

81. Ha¨ussinger, D. & Ha¨ussinger, H. Neural control of hepatic osmolytes and parenchymal cell hydration. *Anat Rec A Discov Mol Cell Evol Biol* **280A**, 893–900 (2004).

82. Browe, D. M. & Baumgarten, C. M. Angiotensin II (AT1) Receptors and NADPH Oxidase Regulate Cl− Current Elicited by β1 Integrin Stretch in Rabbit Ventricular Myocytes. *J Gen Physiol* **124**, 273 (2004).

83. Moeckel, G. W. *et al.* Role of integrin α1β1 in the regulation of renal medullary osmolyte concentration. *Am J Physiol Renal Physiol* **290**, 223–231 (2006).

84. Sinha, B. *et al.* Cells respond to mechanical stress by rapid disassembly of caveolae. *Cell* **144**, 402–413 (2011).

85. Ingber, D. E. Tensegrity I. Cell structure and hierarchical systems biology. *J Cell Sci* **116**, 1157–1173 (2003).

86. Henson, J. H. Relationships Between the Actin Cytoskeleton and Cell Volume Regulation. *Microsc. Res. Tech* **47**, 155–162 (1999).

87. Gonzalez, N. P. *et al.* Cell tension and mechanical regulation of cell volume. *Mol Biol Cell* **29**, 2591–2600 (2018).

88. Perez-Gonzalez, N. A. *et al.* YAP and TAZ regulate cell volume. *Journal of Cell Biology* **218**, 3472–3488 (2019).

89. Orlov, S. N., Shiyan, A., Boudreault, F., Ponomarchuk, O. & Grygorczyk, R. Search for Upstream Cell Volume Sensors: The Role of Plasma Membrane and Cytoplasmic Hydrogel. *Curr Top Membr* **81**, 53–82 (2018).

90. Szatmári, D. *et al.* Intracellular ion concentrations and cation-dependent remodelling of bacterial MreB assemblies. *Scientific Reports 2020 10:1* **10**, 1–13 (2020).

91. Chao, P. C., Sivaselvan, M. & Sachs, F. Cytoskeletal Contribution to Cell Stiffness Due to Osmotic Swelling; Extending the Donnan Equilibrium. *Curr Top Membr* **81**, 83–96 (2018).

92. Essig, A. The 'Pump-Leak' Model and Exchange Diffusion. *Biophys J* **8**, 53–63 (1968).

93. Cadart, C., Venkova, L., Recho, P., Lagomarsino, M. C. & Piel, M. The physics of cell-size regulation across timescales. *Nat Phys* **15**, 993–1004 (2019).

94. Venkova, L. *et al.* A mechano-osmotic feedback couples cell volume to the rate of cell deformation. *Elife* **11**, (2022).

95. Friis, M. B., Vorum, K. G. & Lambert, I. H. Volume-sensitive NADPH oxidase activity and taurine efflux in NIH3T3 mouse fibroblasts. *Am J Physiol Cell Physiol* **294**, 1552–1565 (2008).

96. Zhang, Z., Dmitrieva, N. I., Park, J. H., Levine, R. L. & Burg, M. B. High urea and NaCl carbonylate in renal cells in culture and in vivo, and high urea causes 8-oxoguanine lesions in their DNA. *Proc Natl Acad Sci U S A* **101**, 9491–9496 (2004).

97. Dmitrieva, N. I., Cai, Q. & Burg, M. B. Cells adapted to high NaCl have many DNA breaks and impaired DNA repair both in cell culture and in vivo. *Proc Natl Acad Sci U S A* **101**, 2317–2322 (2004).

98. Kültz, D. & Chakravarty, D. Hyperosmolality in the form of elevated NaCl but not urea causes DNA damage in murine kidney cells. *Proc Natl Acad Sci U S A* **98**, 1999–2004 (2001).

99. Hu, F. *et al.* Hypotonic stress promotes ATP release, reactive oxygen species production and cell proliferation via TRPV4 activation in rheumatoid arthritis rat synovial fibroblasts. *Biochem Biophys Res Commun* **486**, 108–115 (2017).

100. López-Hernández, T., Haucke, V. & Maritzen, T. Endocytosis in the adaptation to cellular stress. *Cell Stress* **4**, 230 (2020).

101. Choe, K. P. & Strange, K. Genome-wide RNAi screen and in vivo protein aggregation reporters identify degradation of damaged proteins as an essential hypertonic stress response. *Am J Physiol Cell Physiol* **295**, 1488–1498 (2008).

102. Yang, T. *et al.* Hypertonic Induction of COX-2 in Collecting Duct Cells by Reactive Oxygen Species of Mitochondrial Origin. *Journal of Biological Chemistry* **280**, 34966–34973 (2005).

103. Ma, P. *et al.* NFAT5 mediates hypertonic stress-induced atherosclerosis via activating NLRP3 inflammasome in endothelium. *Cell Communication and Signaling* **17**, 1–13 (2019).

104. Brocker, C., Thompson, D. C. & Vasiliou, V. The role of hyperosmotic stress in infl ammation and disease. *Biomol Concepts* **3**, 345–364 (2012).

105. Kültz, D. Hyperosmolality triggers oxidative damage in kidney cells. *Proc Natl Acad Sci U S A* **101**, 9177–9178 (2004).

106. Burg, M. B., Ferraris, J. D. & Dmitrieva, N. I. Cellular response to hyperosmotic stresses. *Physiol Rev* **87**, 1441–1474 (2007).

107. Schlenker, T. *et al.* Functional interactions between oxidative stress, membrane Na+ permeability, and cell volume in rat hepatoma cells. *Gastroenterology* **118**, 395–403 (2000).

108. Ringel, F., Bieringer, F., Baethmann, A. & Plesnila, N. Effect of Oxidative Stress on Glial Cell Volume. *https://home.liebertpub.com/neu* **23**, 1693–1704 (2006).

109. Trono, D., Laus, M. N., Soccio, M., Alfarano, M. & Pastore, D. Modulation of potassium channel activity in the balance of ROS and ATP production by durum wheat mitochondria — An amazing defense tool against hyperosmotic stress. *Front Plant Sci* **6**, 1072 (2015).

110. Vellino, S. *et al.* Cross-talk between the calcium channel TRPV4 and reactive oxygen species interlocks adhesive and degradative functions of invadosomes. *Journal of Cell Biology* **220**, (2021).

111. Chen, S. jen *et al.* Transient receptor potential ion channel TRPM2 promotes AML proliferation and survival through modulation of mitochondrial function, ROS, and autophagy. *Cell Death & Disease 2020 11:4* **11**, 1–17 (2020).

112. Fiaschi, T. *et al.* Redox Regulation of β-Actin during Integrin-mediated Cell Adhesion. *Journal of Biological Chemistry* **281**, 22983–22991 (2006).

113. Giannoni, E. *et al.* Redox regulation of anoikis: reactive oxygen species as essential mediators of cell survival. *Cell Death & Differentiation 2008 15:5* **15**, 867–878 (2008).

114. Chiarugi, P. *et al.* Reactive oxygen species as essential mediators of cell adhesion the oxidative inhibition of a FAK tyrosine phosphatase is required for cell adhesion. *Journal of Cell Biology* **161**, 933–944 (2003).

115. Liang, X. *et al.* Cyclic stretch induced oxidative stress by mitochondrial and NADPH oxidase in retinal pigment epithelial cells. *BMC Ophthalmol* **19**, 1–8 (2019).

116. Li, A. E. *et al.* A Role for Reactive Oxygen Species in Endothelial Cell Anoikis. *Circ Res* **85**, 304–310 (1999).

117. Agarwal, M., Biswas, P., Bhattacharya, A. & Sinha, D. K. Reactive oxygen species-mediated cytoplasmic stiffening impairs the phagocytic ability of the macrophage. *J Cell Sci* **133**, (2020).

118. Kang, M., Day, C. A., di Benedetto, E. & Kenworthy, A. K. A quantitative approach to analyze binding diffusion kinetics by confocal FRAP. *Biophys J* **99**, 2737–2747 (2010).

119. Kang, M., Day, C. A., Drake, K., Kenworthy, A. K. & DiBenedetto, E. A Generalization of Theory for Two-Dimensional Fluorescence Recovery after Photobleaching Applicable to Confocal Laser Scanning Microscopes. *Biophys J* **97**, 1501–1511 (2009).

120. Kang, M., Day, C. A., Kenworthy, A. K. & DiBenedetto, E. Simplified Equation to Extract Diffusion Coefficients from Confocal FRAP Data. *Traffic* **13**, 1589–1600 (2012).

121. Wu, J., Shekhar, N., Lele, P. P. & Lele, T. P. FRAP Analysis: Accounting for Bleaching during Image Capture. *PLoS One* **7**, e42854 (2012).

122. Principles of Fluorescence Spectroscopy - Joseph R. Lakowicz - Google Books. https://books.google.co.in/books?id=-PSybuLNxcAC&q=perrin+equation#v=snippet&q=perrin%20equation&f=false.

123. Jameson, D. M. & Sawyer, W. H. [12] Fluorescence anisotropy applied to biomolecular interactions. *Methods Enzymol* **246**, 283–300 (1995).

124. Introduction to Fluorescence - David M. Jameson - Google Books. https://books.google.co.in/books?hl=en&lr=&id=SI-lAgAAQBAJ&oi=fnd&pg=PP1&dq=info:mROVhAlnb0oJ:scholar.google.com&ots=bA_mCYIi9l&sig=o1lokdcfxd8OhMi_62ihVo83oQw&redir_esc=y#v=onepage&q&f=false.

125. Ghosh, S., Saha, S., Goswami, D., Bilgrami, S. & Mayor, S. Dynamic Imaging of Homo-FRET in Live Cells by Fluorescence Anisotropy Microscopy. *Methods Enzymol* **505**, 291–327 (2012).

126. Li, B. & Wang, J. H. C. Fibroblasts and myofibroblasts in wound healing: Force generation and measurement. *J Tissue Viability* **20**, 108–120 (2011).

127. D'Urso, M. & Kurniawan, N. A. Mechanical and Physical Regulation of Fibroblast–Myofibroblast Transition: From Cellular Mechanoresponse to Tissue Pathology. *Front Bioeng Biotechnol* **8**, 1459 (2020).

128. Enyedi, B. & Niethammer, P. Mechanisms of epithelial wound detection. *Trends Cell Biol* **25**, 398–407 (2015).

129. Jonas, M., Huang, H., Kamm, R. D. & So, P. T. C. Fast Fluorescence Laser Tracking Microrheometry, II: Quantitative Studies of Cytoskeletal Mechanotransduction. *Biophys J* **95**, 895–909 (2008).

130. Tanida, I., Ueno, T. & Uchiyama, Y. A Super-Ecliptic, pHluorin-mKate2, Tandem Fluorescent Protein-Tagged Human LC3 for the Monitoring of Mammalian Autophagy. *PLoS One* **9**, e110600 (2014).

131. Shinoda, H., Shannon, M. & Nagai, T. Fluorescent Proteins for Investigating Biological Events in Acidic Environments. *International Journal of Molecular Sciences 2018, Vol. 19, Page 1548* **19**, 1548 (2018).

132. Cranfill, P. J. *et al.* Quantitative assessment of fluorescent proteins. *Nature Methods 2016 13:7* **13**, 557–562 (2016).

133. Strickler, S. J. & Berg, R. A. Relationship between Absorption Intensity and Fluorescence Lifetime of Molecules. *J Chem Phys* **37**, 814–822 (1962).

134. Tregidgo, C. L., Levitt, J. A. & Suhling, K. Effect of refractive index on the fluorescence lifetime of green fluorescent protein. *https://doi.org/10.1117/1.2937212* **13**, 031218 (2008).

135. Toptygin, D., Savtchenko, R. S., Meadow, N. D., Roseman, S. & Brand, L. Effect of the solvent refractive index on the excited-state lifetime of a single tryptophan residue in a protein. *Journal of Physical Chemistry B* **106**, 3724–3734 (2002).

136. Suhling, K. *et al.* Imaging the Environment of Green Fluorescent Protein. *Biophys J* **83**, 3589–3595 (2002).

137. Novikov, E. G., Skakun, V. v, Borst, J. W. & Visser, A. J. W. G. Maximum entropy analysis of polarized fluorescence decay of (E)GFP in aqueous solution. *Methods Appl Fluoresc* **6**, 014001 (2017).

138. Pliss, A. *et al.* Cycles of protein condensation and discharge in nuclear organelles studied by fluorescence lifetime imaging. *Nature Communications 2019 10:1* **10**, 1–9 (2019).

139. Levchenko, S. M., Pliss, A. & Qu, J. Fluorescence lifetime imaging of fluorescent proteins as an effective quantitative tool for noninvasive study of intracellular processes. *https://doi.org/10.1142/S1793545817300099* **11**, (2017).

140. Rashid, R., Chee, S. M. L., Raghunath, M. & Wohland, T. Macromolecular crowding gives rise to microviscosity, anomalous diffusion and accelerated actin polymerization. *Phys Biol* **12**, 034001 (2015).

141. Suhling, K., Davis, D. M. & Phillips, D. The Influence of Solvent Viscosity on the Fluorescence Decay and Time-Resolved Anisotropy of Green Fluorescent Protein. *Journal of Fluorescence 2002 12:1* **12**, 91–95 (2002).

142. Devauges, V. *et al.* Homodimerization of Amyloid Precursor Protein at the Plasma Membrane: A homoFRET Study by Time-Resolved Fluorescence Anisotropy Imaging. *PLoS One* **7**, e44434 (2012).

143. CRC Handbook of Chemistry and Physics, 85th Edition - Google Books. https://books.google.co.in/books?hl=en&lr&id=WDll8hA006AC&oi=fnd&pg=PA1&dq=D.R.+Lide.+.+CRC+Handbook+of+Chemistry+and+Physics,+84th+Edition+Edited+by+David+R.+Lide+.+CRC+Press+LLC:+Boca+Raton.+2003.+2616+pp.+139.95.+ISBN+08493-04849.+J+Am+Chem+Soc,+126,+15861586.&ots=U0lG_LOVJp&sig=OW4yzDM8oWZJyIaaW033Idps-6w&redir_esc=y&pli=1#v=onepage&q&f=false.

144. Miermont, A. *et al.* Severe osmotic compression triggers a slowdown of intracellular signaling, which can be explained by molecular crowding. *Proc Natl Acad Sci U S A* **110**, 5725–5730 (2013).

145. Ho, S. N. Intracellular water homeostasis and the mammalian cellular osmotic stress response. *J Cell Physiol* **206**, 9–15 (2006).

146. Petelenz-Kurdziel, E. *et al.* Quantification of cell volume changes upon hyperosmotic stress in Saccharomyces cerevisiae. *Integr Biol (Camb)* **3**, 1120–1126 (2011).

147. Vallés, P. G., Bocanegra, V., Gil Lorenzo, A. & Costantino, V. V. Physiological Functions and Regulation of the Na⁺/H⁺ Exchanger [NHE1] in Renal Tubule Epithelial Cells. *Kidney Blood Press Res* **40**, 452–466 (2015).

148. Serra, S. A. *et al.* LRRC8A-containing chloride channel is crucial for cell volume recovery and survival under hypertonic conditions. *Proceedings of the National Academy of Sciences* **118**, e2025013118 (2021).

149. Irianto, J. *et al.* Osmotic Challenge Drives Rapid and Reversible Chromatin Condensation in Chondrocytes. *Biophys J* **104**, 759–769 (2013).

150. Olins, A. L., Gould, T. J., Boyd, L., Sarg, B. & Olins, D. E. Hyperosmotic stress: in situ chromatin phase separation. *Nucleus* **11**, 1–18 (2020).

151. James, A. L., Dreiss, C. A., Steinmark, I. E., Suhling, K. & Yahioglu, G. Imaging mitochondrial matrix viscosity in live cells via fluorescence

lifetime imaging (FLIM) of fluorescent molecular rotors. *https://doi.org/10.1117/12.2508676* **10893**, 43–49 (2019).

152. Schlame, M. Protein crowding in the inner mitochondrial membrane. *Biochimica et Biophysica Acta (BBA) - Bioenergetics* **1862**, 148305 (2021).

153. Yuan, L. *et al.* Real-time imaging of viscosity in the mitochondrial matrix by a red-emissive molecular rotor. *Anal Methods* **13**, 3181–3186 (2021).

154. Mund, T., Lewis, M. J., Maslen, S. & Pelham, H. R. Peptide and small molecule inhibitors of HECT-type ubiquitin ligases. *Proc Natl Acad Sci U S A* **111**, 16736–16741 (2014).

155. Siegel, M. R. & Sisler, H. D. Inhibition of Protein Synthesis in vitro by Cycloheximide. *Nature 1963 200:4907* **200**, 675–676 (1963).

156. Parag, H. A., Raboy, B. & Kulka, R. G. Effect of heat shock on protein degradation in mammalian cells: involvement of the ubiquitin system. *EMBO J* **6**, 55 (1987).

157. Sizaire, F. *et al.* Refractive index sensing using Fluorescence Lifetime Imaging (FLIM). *J Phys Conf Ser* **45**, 223 (2006).

158. Laurent, V. M. *et al.* Gradient of Rigidity in the Lamellipodia of Migrating Cells Revealed by Atomic Force Microscopy. *Biophys J* **89**, 667–675 (2005).

159. Karlsson, T., Bolshakova, A., Magalhães, M. A. O., Loitto, V. M. & Magnusson, K. E. Fluxes of Water through Aquaporin 9 Weaken

Membrane-Cytoskeleton Anchorage and Promote Formation of Membrane Protrusions. *PLoS One* **8**, e59901 (2013).

160. Direito, I., Madeira, A., Brito, M. A. & Soveral, G. Aquaporin-5: from structure to function and dysfunction in cancer. *Cellular and Molecular Life Sciences 2016 73:8* **73**, 1623–1640 (2016).

161. Papadopoulos, M. C. & Saadoun, S. Key roles of aquaporins in tumor biology. *Biochimica et Biophysica Acta (BBA) - Biomembranes* **1848**, 2576–2583 (2015).

162. Liebermeister, W. *et al.* Visual account of protein investment in cellular functions. *Proceedings of the National Academy of Sciences* **111**, 8488–8493 (2014).

163. Pegoraro, A. F., Janmey, P. & Weitz, D. A. Mechanical Properties of the Cytoskeleton and Cells. *Cold Spring Harb Perspect Biol* **9**, a022038 (2017).

164. Loiodice, I. *et al.* Quantifying Tubulin Concentration and Microtubule Number Throughout the Fission Yeast Cell Cycle. *Biomolecules 2019, Vol. 9, Page 86* **9**, 86 (2019).

165. Yadav, S., Shire, S. J. & Kalonia, D. S. Viscosity Analysis of High Concentration Bovine Serum Albumin Aqueous Solutions. *Pharmaceutical Research 2011 28:8* **28**, 1973–1983 (2011).

166. Schindelin, J. *et al.* Fiji: an open-source platform for biological-image analysis. *Nat. Methods* **9**, 676–682 (2012).

167. Pliss, A., Zhao, L., Ohulchanskyy, T. Y., Qu, J. & Prasad, P. N. Fluorescence lifetime of fluorescent proteins as an intracellular

environment probe sensing the cell cycle progression. *ACS Chem Biol* **7**, 1385–1392 (2012).

168. Boyd-Shiwarski, C. R. *et al.* WNK kinases sense molecular crowding and rescue cell volume via phase separation. *bioRxiv* 2022.01.10.475707 (2022) doi:10.1101/2022.01.10.475707.

169. Keber, F. C., Nguyen, T., Brangwynne, C. P. & Wühr, M. Evidence for widespread cytoplasmic structuring into mesoscopic condensates. *bioRxiv* 2021.12.17.473234 (2021) doi:10.1101/2021.12.17.473234.

170. Vonderach, M., Byrne, D. P., Barran, P. E., Eyers, P. A. & Eyers, C. E. DNA Binding and Phosphorylation Regulate the Core Structure of the NF-κB p50 Transcription Factor. *J Am Soc Mass Spectrom* **30**, 128–138 (2019).

171. Yan, Q. *et al.* Nuclear factor-κB binding motifs specify Toll-like receptor-induced gene repression through an inducible repressosome. *Proc Natl Acad Sci U S A* **109**, 14140–14145 (2012).

172. Smith, E. L. *et al.* The regulation of sequence specific NF-κB DNA binding and transcription by IKKβ phosphorylation of NF-κB p50 at serine 80. *Nucleic Acids Res* **47**, 11151–11163 (2019).

173. Takashiba, S. *et al.* Differentiation of monocytes to macrophages primes cells for lipopolysaccharide stimulation via accumulation of cytoplasmic nuclear factor κB. *Infect Immun* **67**, 5573–5578 (1999).

174. Jones, E., Adcock, I. M., Ahmed, B. Y. & Punchard, N. A. Modulation of LPS stimulated NF-kappaB mediated nitric oxide production by PKCε and JAK2 in RAW macrophages. *J Inflamm* **4**, 1–9 (2007).

175. Bhattacharya, A., Agarwal, M., Mukherjee, R., Sen, P. & Sinha, D. K. 3D micro-environment regulates NF-κβ dependent adhesion to induce monocyte differentiation. *Cell Death & Disease 2018 9:9* **9**, 1–16 (2018).

176. Celik, E., Abdulreda, M. H., Maiguel, D., Li, J. & Moy, V. T. Rearrangement of microtubule network under biochemical and mechanical stimulations. *Methods* **60**, 195–201 (2013).

177. Kiuchi, T., Nagai, T., Ohashi, K. & Mizuno, K. Measurements of spatiotemporal changes in G-actin concentration reveal its effect on stimulus-induced actin assembly and lamellipodium extension. *Journal of Cell Biology* **193**, 365–380 (2011).

178. Rosette, C. & Karin, M. Ultraviolet Light and Osmotic Stress: Activation of the JNK Cascade Through Multiple Growth Factor and Cytokine Receptors. *Science (1979)* **274**, 1194–1197 (1996).

179. D'Alessio, A. *et al.* Targeting of Tumor Necrosis Factor Receptor 1 to Low Density Plasma Membrane Domains in Human Endothelial Cells. *Journal of Biological Chemistry* **285**, 23868–23879 (2010).

180. Bae, G. D. *et al.* Upregulation of caveolin-1 and its colocalization with cytokine receptors contributes to beta cell apoptosis. *Scientific Reports 2019 9:1* **9**, 1–10 (2019).

181. Roth, I. *et al.* Osmoprotective transcription factor NFAT5/TonEBP modulates nuclear factor-κB activity. *Mol Biol Cell* **21**, 3459–3474 (2010).

182. Farabaugh, K. T. *et al.* PACT-mediated pkr activation acts as a hyperosmotic stress intensity sensor weakening osmoadaptation and enhancing inflammation. *Elife* **9**, (2020).

183. Zhou, X., Cai, J., Liu, W., Wu, X. & Gao, C. Cysteinyl leukotriene receptor type 1 (CysLT1R) antagonist zafirlukast protects against TNF-α-induced endothelial inflammation. *Biomedicine & Pharmacotherapy* **111**, 452–459 (2019).

184. Weinelt, N. *et al.* Quantitative single-molecule imaging of TNFR1 reveals zafirlukast as antagonist of TNFR1 clustering and TNFα-induced NF-κB signaling. *J Leukoc Biol* **109**, 363–371 (2021).

185. Biswas, A., Alex, A. & Sinha, B. Mapping Cell Membrane Fluctuations Reveals Their Active Regulation and Transient Heterogeneities. *Biophys J* **113**, 1768–1781 (2017).

186. Shiba, H., Noguchi, H. & Fournier, J. B. Monte Carlo study of the frame, fluctuation and internal tensions of fluctuating membranes with fixed area. *Soft Matter* **12**, 2373–2380 (2016).

187. Taddei, M. L., Giannoni, E., Fiaschi, T. & Chiarugi, P. Anoikis: an emerging hallmark in health and diseases. *J Pathol* **226**, 380–393 (2012).

188. Kim, Y. N., Koo, K. H., Sung, J. Y., Yun, U. J. & Kim, H. Anoikis resistance: An essential prerequisite for tumor metastasis. *Int J Cell Biol* (2012) doi:10.1155/2012/306879.

189. Paoli, P., Giannoni, E. & Chiarugi, P. Anoikis molecular pathways and its role in cancer progression. *Biochimica et Biophysica Acta (BBA) - Molecular Cell Research* **1833**, 3481–3498 (2013).

190. Adeshakin, F. O. *et al.* Mechanisms for Modulating Anoikis Resistance in Cancer and the Relevance of Metabolic Reprogramming. *Front Oncol* **11**, 528 (2021).

191. Kamarajugadda, S. *et al.* Glucose Oxidation Modulates Anoikis and Tumor Metastasis. *Mol Cell Biol* **32**, 1893–1907 (2012).

192. Wang, G. X. *et al.* ΔNp63 Inhibits Oxidative Stress-Induced Cell Death, Including Ferroptosis, and Cooperates with the BCL-2 Family to Promote Clonogenic Survival. *Cell Rep* **21**, 2926–2939 (2017).

193. Kheradmand, F., Werner, E., Tremble, P., Symons, M. & Werb, Z. Role of rac1 and oxygen radicals in collagenase-1 expression induced by cell shape change. *Science (1979)* **280**, 898–902 (1998).

194. Grinnell, F., Zhu, M., Carlson, M. A. & Abrams, J. M. Release of Mechanical Tension Triggers Apoptosis of Human Fibroblasts in a Model of Regressing Granulation Tissue. *Exp Cell Res* **248**, 608–619 (1999).

195. Fiaschi, T., Cozzi, G. & Chiarugi, P. Redox Regulation of Nonmuscle Myosin Heavy Chain during Integrin Engagement. *J Signal Transduct* **2012**, 1–9 (2012).

196. Ma, Z., Liu, Z., Myers, D. P. & Terada, L. S. Mechanotransduction and anoikis: Death and the homeless cell. *http://dx.doi.org/10.4161/cc.7.16.6463* **7**, 2462–2465 (2008).

197. Verbon, E. H., Post, J. A. & Boonstra, J. The influence of reactive oxygen species on cell cycle progression in mammalian cells. *Gene* **511**, 1–6 (2012).

198. Patterson, J. C. *et al.* ROS and Oxidative Stress Are Elevated in Mitosis during Asynchronous Cell Cycle Progression and Are Exacerbated by Mitotic Arrest. *Cell Syst* **8**, 163-167.e2 (2019).

199. Signoretto, E. *et al.* Nocodazole Induced Suicidal Death of Human Erythrocytes. *Cellular Physiology and Biochemistry* **38**, 379–392 (2016).

200. Zheng, J. Y., Tan, H. L., Matsudaira, P. T. & Choo, A. Excess reactive oxygen species production mediates monoclonal antibody-induced human embryonic stem cell death via oncosis. *Cell Death & Differentiation 2017 24:3* **24**, 546–558 (2017).

201. Munnamalai, V. *et al.* Bidirectional interactions between NOX2-type NADPH oxidase and the F-actin cytoskeleton in neuronal growth cones. *J Neurochem* **130**, 526–540 (2014).

202. Kim, D. H. *et al.* Volume regulation and shape bifurcation in the cell nucleus. *J Cell Sci* **128**, 3375–3385 (2015).

203. Huber, M. D. & Gerace, L. The size-wise nucleus: nuclear volume control in eukaryotes. *Journal of Cell Biology* **179**, 583–584 (2007).

204. Lemière, J., Real-Calderon, P., Holt, L. J., Fai, T. G. & Chang, F. Control of nuclear size by osmotic forces in Schizosaccharomyces pombe. *Elife* **11**, (2022).

205. Pittas, T., Zuo, W. & Boersma, A. J. Engineering crowding sensitivity into protein linkers. *Methods Enzymol* **647**, 51–81 (2021).

206. Löwe, M., Kalacheva, M., Boersma, A. J. & Kedrov, A. The more the merrier: effects of macromolecular crowding on the structure and

dynamics of biological membranes. *FEBS Journal* **287**, 5039–5067 (2020).

207. Franco, R., Panayiotidis, M. I. & de La Paz, L. D. O. Autocrine signaling involved in cell volume regulation: The role of released transmitters and plasma membrane receptors. *J Cell Physiol* **216**, 14–28 (2008).

List of Publications

1. Wozniak, M. A., Modzelewska, K., Kwong, L. & Keely, P. J. Focal adhesion regulation of cell behavior. *Biochimica et Biophysica Acta (BBA) - Molecular Cell Research* **1692**, 103–119 (2004).

2. Walpita, D. & Hay, E. D. Studying actin-dependent processes in tissue culture. *Nature Reviews Molecular Cell Biology 2002 3:2* **3**, 137–141 (2002).

3. Guo, M. *et al.* Cell volume change through water efflux impacts cell stiffness and stem cell fate. *Proc Natl Acad Sci U S A* **114**, E8618–E8627 (2017).

4. Hakkinen, K. M., Harunaga, J. S., Doyle, A. D. & Yamada, K. M. Direct Comparisons of the Morphology, Migration, Cell Adhesions, and Actin Cytoskeleton of Fibroblasts in Four Different Three-Dimensional Extracellular Matrices. *https://home.liebertpub.com/tea* **17**, 713–724 (2010).

5. Okada, Y., Sabirov, R. Z., Sato-Numata, K. & Numata, T. Cell Death Induction and Protection by Activation of Ubiquitously Expressed Anion/Cation Channels. Part 1: Roles of VSOR/VRAC in Cell Volume Regulation, Release of Double-Edged Signals and Apoptotic/Necrotic Cell Death. *Front Cell Dev Biol* **8**, 1776 (2021).

6. Okada, Y. & Maeno, E. Apoptosis, cell volume regulation and volume-regulatory chloride channels. *Comp Biochem Physiol A Mol Integr Physiol* **130**, 377–383 (2001).

7. Morishita, K., Watanabe, K. & Ichijo, H. Cell volume regulation in cancer cell migration driven by osmotic water flow. *Cancer Sci* **110**, 2337–2347 (2019).

8. Minton, A. P., Colclasure, G. C. & Parker, J. C. Model for the role of macromolecular crowding in regulation of cellular volume. *Proc Natl Acad Sci U S A* **89**, 10504–10506 (1992).

9. Al-Habori, M. Macromolecular crowding and its role as intracellular signalling of cell volume regulation. *Int J Biochem Cell Biol* **33**, 844–864 (2001).

10. Hoffmann, E. K., Lambert, I. H. & Pedersen, S. F. Physiology of cell volume regulation in vertebrates. *Physiol. Rev.* **89**, 193–277 (2009).

11. Watanabe, K., Umeda, T., Niwa, K., Naguro, I. & Ichijo, H. A PP6-ASK3 Module Coordinates the Bidirectional Cell Volume Regulation under Osmotic Stress. *Cell Rep* **22**, 2809–2817 (2018).

12. Delarue, M. *et al.* mTORC1 controls phase separation and the biophysical properties of the cytoplasm by tuning crowding. *Cell* **174**, 338-349.e20 (2018).

13. Burg, M. B. Macromolecular Crowding as a Cell VolumeSensor. *Cellular Physiology and Biochemistry* **10**, 251–256 (2000).

14. Model, M. A., Hollembeak, J. E. & Kurokawa, M. Macromolecular crowding: A hidden link between cell volume and everything else. *Cellular Physiology and Biochemistry* **55**, 25–40 (2021).

15. Kohata, K. & Miyoshi, D. RNA phase separation–mediated direction of molecular trafficking under conditions of molecular crowding. *Biophys Rev* **12**, 669–676 (2020).

16. Erickson, H. P. Size and Shape of Protein Molecules at the Nanometer Level Determined by Sedimentation, Gel Filtration, and Electron Microscopy. *Biol Proced Online* **11**, 32 (2009).

17. Yamamoto, J. *et al.* Quantitative evaluation of macromolecular crowding environment based on translational and rotational diffusion using polarization dependent fluorescence correlation spectroscopy. *Scientific Reports 2021 11:1* **11**, 1–11 (2021).

18. Speer, S. L., Stewart, C. J., Sapir, L., Harries, D. & Pielak, G. J. Macromolecular Crowding Is More than Hard-Core Repulsions. *https://doi.org/10.1146/annurev-biophys-091321-071829* **51**, (2022).

19. Minton, A. P. Excluded volume as a determinant of macromolecular structure and reactivity. *Biopolymers* **20**, 2093–2120 (1981).

20. Ralston, G. B. Effects of ‘crowding’ in protein solutions. *J Chem Educ* **67**, 857–860 (1990).

21. Willis, P. R., Nichol, L. W. & Siezen, R. J. The indefinite self-association of lysozyme: consideration of composition-dependent activity coefficients. *Biophys Chem* **11**, 71–82 (1980).

22. Vöpel, T. & Makhatadze, G. I. Enzyme Activity in the Crowded Milieu. *PLoS One* **7**, e39418 (2012).

23. Ma, B. & Nussinov, R. Structured crowding and its effects on enzyme catalysis. *Top Curr Chem* **337**, 123–138 (2013).

24. Ellis, R. J. Macromolecular crowding: obvious but underappreciated. *Trends Biochem Sci* **26**, 597–604 (2001).

25. Qin, S., Minh, D. D. L., McCammon, J. A. & Zhou, H. X. Method to predict crowding effects by postprocessing molecular dynamics trajectories: Application to the flap dynamics of HIV-1 protease. *Journal of Physical Chemistry Letters* **1**, 107–110 (2010).

26. Minh, D. D. L., Chang, C. E., Trylska, J., Tozzini, V. & McCammon, J. A. The influence of macromolecular crowding on HIV-1 protease internal dynamics. *J Am Chem Soc* **128**, 6006–6007 (2006).

27. Asakura, S. & Oosawa, F. Interaction between particles suspended in solutions of macromolecules. *Journal of Polymer Science* **33**, 183–192 (1958).

28. Asakura, S. & Oosawa, F. On Interaction between Two Bodies Immersed in a Solution of Macromolecules. *J Chem Phys* **22**, 1255 (2004).

29. Marenduzzo, D., Finan, K. & Cook, P. R. The depletion attraction: an underappreciated force driving cellular organization. *Journal of Cell Biology* **175**, 681–686 (2006).

30. André, A. A. M. & Spruijt, E. Liquid–Liquid Phase Separation in Crowded Environments. *International Journal of Molecular Sciences 2020, Vol. 21, Page 5908* **21**, 5908 (2020).

31. Shin, Y. & Brangwynne, C. P. Liquid phase condensation in cell physiology and disease. *Science (1979)* **357**, (2017).

32. Jalihal, A. P. *et al.* Hyperosmotic phase separation: Condensates beyond inclusions, granules and organelles. *Journal of Biological Chemistry* **296**, (2021).

33. Jalihal, A. P. *et al.* Multivalent Proteins Rapidly and Reversibly Phase-Separate upon Osmotic Cell Volume Change. *Mol Cell* **79**, 978-990.e5 (2020).

34. Mittal, S., Chowhan, R. K. & Singh, L. R. Macromolecular crowding: Macromolecules friend or foe. *Biochimica et Biophysica Acta (BBA) - General Subjects* **1850**, 1822–1831 (2015).

35. Soleimaninejad, H., Chen, M. Z., Lou, X., Smith, T. A. & Hong, Y. Measuring macromolecular crowding in cells through fluorescence anisotropy imaging with an AIE fluorogen. *Chemical Communications* **53**, 2874–2877 (2017).

36. Verkman, A. S. Solute and macromolecule diffusion in cellular aqueous compartments. *Trends Biochem Sci* **27**, 27–33 (2002).

37. Puchkov, E. O. Intracellular viscosity: Methods of measurement and role in metabolism. *Biochemistry (Moscow) Supplement Series A: Membrane and Cell Biology 2013 7:4* **7**, 270–279 (2013).

38. Luby-Phelps, K. Cytoarchitecture and Physical Properties of Cytoplasm: Volume, Viscosity, Diffusion, Intracellular Surface Area. *Int Rev Cytol* **192**, 189–221 (1999).

39. Kuimova, M. K., Yahioglu, G., Levitt, J. A. & Suhling, K. Molecular rotor measures viscosity of live cells via fluorescence lifetime imaging. *J Am Chem Soc* **130**, 6672–6673 (2008).

40. Liu, F. *et al.* Ratiometric Detection of Viscosity Using a Two-Photon Fluorescent Sensor. *Chemistry – A European Journal* **19**, 1548–1553 (2013).

41. Kuimova, M. K. *et al.* Imaging intracellular viscosity of a single cell during photoinduced cell death. *Nature Chemistry 2009 1:1* **1**, 69–73 (2009).

42. Miermont, A. *et al.* Severe osmotic compression triggers a slowdown of intracellular signaling, which can be explained by molecular crowding. *Proc Natl Acad Sci U S A* **110**, 5725–5730 (2013).

43. Swaminathan, R., Hoang, C. P. & Verkman, A. S. Photobleaching recovery and anisotropy decay of green fluorescent protein GFP-S65T in solution and cells: cytoplasmic viscosity probed by green fluorescent protein translational and rotational diffusion. *Biophys J* **72**, 1900–1907 (1997).

44. Kao, H. P., Abney, J. R. & Verkman, A. S. Determinants of the translational mobility of a small solute in cell cytoplasm. *Journal of Cell Biology* **120**, 175–184 (1993).

45. Guigas, G., Kalla, C. & Weiss, M. Probing the Nanoscale Viscoelasticity of Intracellular Fluids in Living Cells. *Biophys J* **93**, 316–323 (2007).

46. Fabry, B. *et al.* Scaling the microrheology of living cells. *Phys Rev Lett* **87**, 148102–148102 (2001).

47. Wong, I. Y. *et al.* Anomalous diffusion probes microstructure dynamics of entangled F-actin networks. *Phys Rev Lett* **92**, 178101 (2004).

48. Yadav, S., Shire, S. J. & Kalonia, D. S. Viscosity Analysis of High Concentration Bovine Serum Albumin Aqueous Solutions. *Pharmaceutical Research 2011 28:8* **28**, 1973–1983 (2011).

49. Gnutt, D. *et al.* Excluded-Volume Effects in Living Cells. *Angewandte Chemie International Edition* **54**, 2548–2551 (2015).

50. Boersma, A. J., Zuhorn, I. S. & Poolman, B. A sensor for quantification of macromolecular crowding in living cells. *Nature Methods 2015 12:3* **12**, 227–229 (2015).

51. Morikawa, T. J. *et al.* Dependence of fluorescent protein brightness on protein concentration in solution and enhancement of it. *Scientific Reports 2016 6:1* **6**, 1–13 (2016).

52. Murade, C. U. & Shubeita, G. T. A molecular sensor reveals differences in macromolecular crowding between the cytoplasm and nucleoplasm. *ACS Sens* **4**, 1835–1843 (2019).

53. Murade, C. U. & Shubeita, G. T. A molecular sensor reveals differences in macromolecular crowding between the cytoplasm and nucleoplasm. *ACS Sens* **4**, 1835–1843 (2019).

54. Kim, M. K. Digital holographic microscopy. *Springer Series in Optical Sciences* **162**, 149–190 (2011).

55. Marian, A. *et al.* Cell refractive index tomography by digital holographic microscopy. *Optics Letters, Vol. 31, Issue 2, pp. 178-180* **31**, 178–180 (2006).

56. Cheung, M. C., Evans, J. G., Mckenna, B. & Ehrlich, D. J. Deep ultraviolet mapping of intracellular protein and nucleic acid in femtograms per pixel. *Cytometry Part A* **79A**, 920–932 (2011).

57. Cheung, M. C. *et al.* Intracellular protein and nucleic acid measured in eight cell types using deep-ultraviolet mass mapping. *Cytometry Part A* **83A**, 540–551 (2013).

58. Kim, T. *et al.* White-light diffraction tomography of unlabelled live cells. *Nature Photonics 2014 8:3* **8**, 256–263 (2014).

59. Yanase, Y. *et al.* Detection of refractive index changes in individual living cells by means of surface plasmon resonance imaging. *Biosens Bioelectron* **26**, 674–681 (2010).

60. Yanase, Y. *et al.* The SPR signal in living cells reflects changes other than the area of adhesion and the formation of cell constructions. *Biosens Bioelectron* **22**, 1081–1086 (2007).

61. Model, M. A. & Petruccelli, J. C. Intracellular Macromolecules in Cell Volume Control and Methods of Their Quantification. *Curr Top Membr* **81**, 237–289 (2018).

62. Parker, J. C. In defense of cell volume? *https://doi.org/10.1152/ajpcell.1993.265.5.C1191* **265**, (1993).

63. Dunham, P. B. Effects of urea on K-Cl cotransport in sheep red blood cells: evidence for two signals of swelling. *https://doi.org/10.1152/ajpcell.1995.268.4.C1026* **268**, (1995).

64. Sarma, P. R. Red Cell Indices. *Clinical Methods: The History, Physical, and Laboratory Examinations* **3rd editio**, (1990).

65. Koltsova, S. v. *et al.* Transcriptomic Changes Triggered by Hypoxia: Evidence for HIF-1α -Independent, [Na+]i/[K+]i-Mediated, Excitation-Transcription Coupling. *PLoS One* **9**, e110597 (2014).

66. Koltsova, S. v., Akimova, O. A., Kotelevtsev, S. v., Grygorczyk, R. & Orlov, S. N. Hyperosmotic and isosmotic shrinkage differentially affect protein phosphorylation and ion transport. *Can J Physiol Pharmacol* **90**, 209–217 (2012).

67. Kojima, R. *et al.* Hypertonicity-Induced Expression of Monocyte Chemoattractant Protein-1 through a Novel Cis-Acting Element and MAPK Signaling Pathways. *The Journal of Immunology* **184**, 5253–5262 (2010).

68. Naguro, I. *et al.* ASK3 responds to osmotic stress and regulates blood pressure by suppressing WNK1-SPAK/OSR1 signaling in the kidney. *Nat. Commun.* **3**, (2012).

69. de los Heros, P., Pacheco-Alvarez, D. & Gamba, G. Role of WNK Kinases in the Modulation of Cell Volume. *Curr Top Membr* **81**, 207–235 (2018).

70. Lambert, I. H., Hoffmann, E. K. & Pedersen, S. F. Cell volume regulation: physiology and pathophysiology. *Acta Physiologica* **194**, 255–282 (2008).

71. Carafoli, E. Calcium signaling: A tale for all seasons. *Proc Natl Acad Sci U S A* **99**, 1115–1122 (2002).

72. Lang, F. *et al.* Functional significance of cell volume regulatory mechanisms. *Physiol Rev* **78**, 247–306 (1998).

73. Lang, F. Mechanisms and Significance of Cell Volume Regulation. *https://doi.org/10.1080/07315724.2007.10719667* **26**, 613S-623S (2013).

74. Roffay, C. *et al.* Passive coupling of membrane tension and cell volume during active response of cells to osmosis. *Proc Natl Acad Sci U S A* **118**, (2021).

75. Deneka, D. *et al.* Allosteric modulation of LRRC8 channels by targeting their cytoplasmic domains. *Nature Communications 2021 12:1* **12**, 1–14 (2021).

76. Qiu, Z. *et al.* SWELL1, a Plasma Membrane Protein, Is an Essential Component of Volume-Regulated Anion Channel. *Cell* **157**, 447–458 (2014).

77. Jentsch, T. J. VRACs and other ion channels and transporters in the regulation of cell volume and beyond. *Nat. Rev. Mol. Cell Biol.* **17**, 293–307 (2016).

78. le Roux, A. L., Quiroga, X., Walani, N., Arroyo, M. & Roca-Cusachs, P. The plasma membrane as a mechanochemical transducer. *Philos. Trans. R. Soc. Lond. B Biol. Sci.* **374**, 20180221 (2019).

79. Riggi, M. *et al.* Decrease in plasma membrane tension triggers PtdIns(4,5)P2 phase separation to inactivate TORC2. *Nat. Cell Biol.* **20**, 1043–1051 (2018).

80. Riggi, M., Kusmider, B. & Loewith, R. The flipside of the TOR coin - TORC2 and plasma membrane homeostasis at a glance. *J Cell Sci* **133**, jcs242040–jcs242040 (2020).

81. Ha¨ussinger, D. & Ha¨ussinger, H. Neural control of hepatic osmolytes and parenchymal cell hydration. *Anat Rec A Discov Mol Cell Evol Biol* **280A**, 893–900 (2004).

82. Browe, D. M. & Baumgarten, C. M. Angiotensin II (AT1) Receptors and NADPH Oxidase Regulate Cl− Current Elicited by β1 Integrin Stretch in Rabbit Ventricular Myocytes. *J Gen Physiol* **124**, 273 (2004).

83. Moeckel, G. W. *et al.* Role of integrin α1β1 in the regulation of renal medullary osmolyte concentration. *Am J Physiol Renal Physiol* **290**, 223–231 (2006).

84. Sinha, B. *et al.* Cells respond to mechanical stress by rapid disassembly of caveolae. *Cell* **144**, 402–413 (2011).

85. Ingber, D. E. Tensegrity I. Cell structure and hierarchical systems biology. *J Cell Sci* **116**, 1157–1173 (2003).

86. Henson, J. H. Relationships Between the Actin Cytoskeleton and Cell Volume Regulation. *Microsc. Res. Tech* **47**, 155–162 (1999).

87. Gonzalez, N. P. *et al.* Cell tension and mechanical regulation of cell volume. *Mol Biol Cell* **29**, 2591–2600 (2018).

88. Perez-Gonzalez, N. A. *et al.* YAP and TAZ regulate cell volume. *Journal of Cell Biology* **218**, 3472–3488 (2019).

89. Orlov, S. N., Shiyan, A., Boudreault, F., Ponomarchuk, O. & Grygorczyk, R. Search for Upstream Cell Volume Sensors: The Role of Plasma Membrane and Cytoplasmic Hydrogel. *Curr Top Membr* **81**, 53–82 (2018).

90. Szatmári, D. *et al.* Intracellular ion concentrations and cation-dependent remodelling of bacterial MreB assemblies. *Scientific Reports 2020 10:1* **10**, 1–13 (2020).

91. Chao, P. C., Sivaselvan, M. & Sachs, F. Cytoskeletal Contribution to Cell Stiffness Due to Osmotic Swelling; Extending the Donnan Equilibrium. *Curr Top Membr* **81**, 83–96 (2018).

92. Essig, A. The 'Pump-Leak' Model and Exchange Diffusion. *Biophys J* **8**, 53–63 (1968).

93. Cadart, C., Venkova, L., Recho, P., Lagomarsino, M. C. & Piel, M. The physics of cell-size regulation across timescales. *Nat Phys* **15**, 993–1004 (2019).

94. Venkova, L. *et al.* A mechano-osmotic feedback couples cell volume to the rate of cell deformation. *Elife* **11**, (2022).

95. Friis, M. B., Vorum, K. G. & Lambert, I. H. Volume-sensitive NADPH oxidase activity and taurine efflux in NIH3T3 mouse fibroblasts. *Am J Physiol Cell Physiol* **294**, 1552–1565 (2008).

96. Zhang, Z., Dmitrieva, N. I., Park, J. H., Levine, R. L. & Burg, M. B. High urea and NaCl carbonylate in renal cells in culture and in vivo, and high urea causes 8-oxoguanine lesions in their DNA. *Proc Natl Acad Sci U S A* **101**, 9491–9496 (2004).

97. Dmitrieva, N. I., Cai, Q. & Burg, M. B. Cells adapted to high NaCl have many DNA breaks and impaired DNA repair both in cell culture and in vivo. *Proc Natl Acad Sci U S A* **101**, 2317–2322 (2004).

98. Kültz, D. & Chakravarty, D. Hyperosmolality in the form of elevated NaCl but not urea causes DNA damage in murine kidney cells. *Proc Natl Acad Sci U S A* **98**, 1999–2004 (2001).

99. Hu, F. *et al.* Hypotonic stress promotes ATP release, reactive oxygen species production and cell proliferation via TRPV4 activation in rheumatoid arthritis rat synovial fibroblasts. *Biochem Biophys Res Commun* **486**, 108–115 (2017).

100. López-Hernández, T., Haucke, V. & Maritzen, T. Endocytosis in the adaptation to cellular stress. *Cell Stress* **4**, 230 (2020).

101. Choe, K. P. & Strange, K. Genome-wide RNAi screen and in vivo protein aggregation reporters identify degradation of damaged proteins as an essential hypertonic stress response. *Am J Physiol Cell Physiol* **295**, 1488–1498 (2008).

102. Yang, T. *et al.* Hypertonic Induction of COX-2 in Collecting Duct Cells by Reactive Oxygen Species of Mitochondrial Origin. *Journal of Biological Chemistry* **280**, 34966–34973 (2005).

103. Ma, P. *et al.* NFAT5 mediates hypertonic stress-induced atherosclerosis via activating NLRP3 inflammasome in endothelium. *Cell Communication and Signaling* **17**, 1–13 (2019).

104. Brocker, C., Thompson, D. C. & Vasiliou, V. The role of hyperosmotic stress in infl ammation and disease. *Biomol Concepts* **3**, 345–364 (2012).

105. Kültz, D. Hyperosmolality triggers oxidative damage in kidney cells. *Proc Natl Acad Sci U S A* **101**, 9177–9178 (2004).

106. Burg, M. B., Ferraris, J. D. & Dmitrieva, N. I. Cellular response to hyperosmotic stresses. *Physiol Rev* **87**, 1441–1474 (2007).

107. Schlenker, T. *et al.* Functional interactions between oxidative stress, membrane Na+ permeability, and cell volume in rat hepatoma cells. *Gastroenterology* **118**, 395–403 (2000).

108. Ringel, F., Bieringer, F., Baethmann, A. & Plesnila, N. Effect of Oxidative Stress on Glial Cell Volume. *https://home.liebertpub.com/neu* **23**, 1693–1704 (2006).

109. Trono, D., Laus, M. N., Soccio, M., Alfarano, M. & Pastore, D. Modulation of potassium channel activity in the balance of ROS and ATP production by durum wheat mitochondria — An amazing defense tool against hyperosmotic stress. *Front Plant Sci* **6**, 1072 (2015).

110. Vellino, S. *et al.* Cross-talk between the calcium channel TRPV4 and reactive oxygen species interlocks adhesive and degradative functions of invadosomes. *Journal of Cell Biology* **220**, (2021).

111. Chen, S. jen *et al.* Transient receptor potential ion channel TRPM2 promotes AML proliferation and survival through modulation of mitochondrial function, ROS, and autophagy. *Cell Death & Disease 2020 11:4* **11**, 1–17 (2020).

112. Fiaschi, T. *et al.* Redox Regulation of β-Actin during Integrin-mediated Cell Adhesion. *Journal of Biological Chemistry* **281**, 22983–22991 (2006).

113. Giannoni, E. *et al.* Redox regulation of anoikis: reactive oxygen species as essential mediators of cell survival. *Cell Death & Differentiation 2008 15:5* **15**, 867–878 (2008).

114. Chiarugi, P. *et al.* Reactive oxygen species as essential mediators of cell adhesion the oxidative inhibition of a FAK tyrosine phosphatase is required for cell adhesion. *Journal of Cell Biology* **161**, 933–944 (2003).

115. Liang, X. *et al.* Cyclic stretch induced oxidative stress by mitochondrial and NADPH oxidase in retinal pigment epithelial cells. *BMC Ophthalmol* **19**, 1–8 (2019).

116. Li, A. E. *et al.* A Role for Reactive Oxygen Species in Endothelial Cell Anoikis. *Circ Res* **85**, 304–310 (1999).

117. Agarwal, M., Biswas, P., Bhattacharya, A. & Sinha, D. K. Reactive oxygen species-mediated cytoplasmic stiffening impairs the phagocytic ability of the macrophage. *J Cell Sci* **133**, (2020).

118. Kang, M., Day, C. A., di Benedetto, E. & Kenworthy, A. K. A quantitative approach to analyze binding diffusion kinetics by confocal FRAP. *Biophys J* **99**, 2737–2747 (2010).

119. Kang, M., Day, C. A., Drake, K., Kenworthy, A. K. & DiBenedetto, E. A Generalization of Theory for Two-Dimensional Fluorescence Recovery after Photobleaching Applicable to Confocal Laser Scanning Microscopes. *Biophys J* **97**, 1501–1511 (2009).

120. Kang, M., Day, C. A., Kenworthy, A. K. & DiBenedetto, E. Simplified Equation to Extract Diffusion Coefficients from Confocal FRAP Data. *Traffic* **13**, 1589–1600 (2012).

121. Wu, J., Shekhar, N., Lele, P. P. & Lele, T. P. FRAP Analysis: Accounting for Bleaching during Image Capture. *PLoS One* **7**, e42854 (2012).

122. Principles of Fluorescence Spectroscopy - Joseph R. Lakowicz - Google Books. https://books.google.co.in/books?id=-PSybuLNxcAC&q=perrin+equation#v=snippet&q=perrin%20equation&f=false.

123. Jameson, D. M. & Sawyer, W. H. [12] Fluorescence anisotropy applied to biomolecular interactions. *Methods Enzymol* **246**, 283–300 (1995).

124. Introduction to Fluorescence - David M. Jameson - Google Books. https://books.google.co.in/books?hl=en&lr=&id=SI-lAgAAQBAJ&oi=fnd&pg=PP1&dq=info:mROVhAlnb0oJ:scholar.google.com&ots=bA_mCYIi9l&sig=o1lokdcfxd8OhMi_62ihVo83oQw&redir_esc=y#v=onepage&q&f=false.

125. Ghosh, S., Saha, S., Goswami, D., Bilgrami, S. & Mayor, S. Dynamic Imaging of Homo-FRET in Live Cells by Fluorescence Anisotropy Microscopy. *Methods Enzymol* **505**, 291–327 (2012).

126. Li, B. & Wang, J. H. C. Fibroblasts and myofibroblasts in wound healing: Force generation and measurement. *J Tissue Viability* **20**, 108–120 (2011).

127. D'Urso, M. & Kurniawan, N. A. Mechanical and Physical Regulation of Fibroblast–Myofibroblast Transition: From Cellular Mechanoresponse to Tissue Pathology. *Front Bioeng Biotechnol* **8**, 1459 (2020).

128. Enyedi, B. & Niethammer, P. Mechanisms of epithelial wound detection. *Trends Cell Biol* **25**, 398–407 (2015).

129. Jonas, M., Huang, H., Kamm, R. D. & So, P. T. C. Fast Fluorescence Laser Tracking Microrheometry, II: Quantitative Studies of Cytoskeletal Mechanotransduction. *Biophys J* **95**, 895–909 (2008).

130. Tanida, I., Ueno, T. & Uchiyama, Y. A Super-Ecliptic, pHluorin-mKate2, Tandem Fluorescent Protein-Tagged Human LC3 for the Monitoring of Mammalian Autophagy. *PLoS One* **9**, e110600 (2014).

131. Shinoda, H., Shannon, M. & Nagai, T. Fluorescent Proteins for Investigating Biological Events in Acidic Environments. *International Journal of Molecular Sciences 2018, Vol. 19, Page 1548* **19**, 1548 (2018).

132. Cranfill, P. J. *et al.* Quantitative assessment of fluorescent proteins. *Nature Methods 2016 13:7* **13**, 557–562 (2016).

133. Strickler, S. J. & Berg, R. A. Relationship between Absorption Intensity and Fluorescence Lifetime of Molecules. *J Chem Phys* **37**, 814–822 (1962).

134. Tregidgo, C. L., Levitt, J. A. & Suhling, K. Effect of refractive index on the fluorescence lifetime of green fluorescent protein. *https://doi.org/10.1117/1.2937212* **13**, 031218 (2008).

135. Toptygin, D., Savtchenko, R. S., Meadow, N. D., Roseman, S. & Brand, L. Effect of the solvent refractive index on the excited-state lifetime of a single tryptophan residue in a protein. *Journal of Physical Chemistry B* **106**, 3724–3734 (2002).

136. Suhling, K. *et al.* Imaging the Environment of Green Fluorescent Protein. *Biophys J* **83**, 3589–3595 (2002).

137. Novikov, E. G., Skakun, V. v, Borst, J. W. & Visser, A. J. W. G. Maximum entropy analysis of polarized fluorescence decay of (E)GFP in aqueous solution. *Methods Appl Fluoresc* **6**, 014001 (2017).

138. Pliss, A. *et al.* Cycles of protein condensation and discharge in nuclear organelles studied by fluorescence lifetime imaging. *Nature Communications 2019 10:1* **10**, 1–9 (2019).

139. Levchenko, S. M., Pliss, A. & Qu, J. Fluorescence lifetime imaging of fluorescent proteins as an effective quantitative tool for noninvasive study of intracellular processes. *https://doi.org/10.1142/S1793545817300099* **11**, (2017).

140. Rashid, R., Chee, S. M. L., Raghunath, M. & Wohland, T. Macromolecular crowding gives rise to microviscosity, anomalous diffusion and accelerated actin polymerization. *Phys Biol* **12**, 034001 (2015).

141. Suhling, K., Davis, D. M. & Phillips, D. The Influence of Solvent Viscosity on the Fluorescence Decay and Time-Resolved Anisotropy of Green Fluorescent Protein. *Journal of Fluorescence 2002 12:1* **12**, 91–95 (2002).

142. Devauges, V. *et al.* Homodimerization of Amyloid Precursor Protein at the Plasma Membrane: A homoFRET Study by Time-Resolved Fluorescence Anisotropy Imaging. *PLoS One* **7**, e44434 (2012).

143. CRC Handbook of Chemistry and Physics, 85th Edition - Google Books. https://books.google.co.in/books?hl=en&lr&id=WDll8hA006AC&oi=fnd&pg=PA1&dq=D.R.+Lide.+.+CRC+Handbook+of+Chemistry+and+Physics,+84th+Edition+Edited+by+David+R.+Lide+.+CRC+Press+LLC:+Boca+Raton.+2003.+2616+pp.+139.95.+ISBN+08493-04849.+J+Am+Chem+Soc,+126,+15861586.&ots=U0lG_LOVJp&sig=OW4yzDM8oWZJyIaaW033Idps-6w&redir_esc=y&pli=1#v=onepage&q&f=false.

144. Miermont, A. *et al.* Severe osmotic compression triggers a slowdown of intracellular signaling, which can be explained by molecular crowding. *Proc Natl Acad Sci U S A* **110**, 5725–5730 (2013).

145. Ho, S. N. Intracellular water homeostasis and the mammalian cellular osmotic stress response. *J Cell Physiol* **206**, 9–15 (2006).

146. Petelenz-Kurdziel, E. *et al.* Quantification of cell volume changes upon hyperosmotic stress in Saccharomyces cerevisiae. *Integr Biol (Camb)* **3**, 1120–1126 (2011).

147. Vallés, P. G., Bocanegra, V., Gil Lorenzo, A. & Costantino, V. V. Physiological Functions and Regulation of the Na⁺/H⁺ Exchanger [NHE1] in Renal Tubule Epithelial Cells. *Kidney Blood Press Res* **40**, 452–466 (2015).

148. Serra, S. A. *et al.* LRRC8A-containing chloride channel is crucial for cell volume recovery and survival under hypertonic conditions. *Proceedings of the National Academy of Sciences* **118**, e2025013118 (2021).

149. Irianto, J. *et al.* Osmotic Challenge Drives Rapid and Reversible Chromatin Condensation in Chondrocytes. *Biophys J* **104**, 759–769 (2013).

150. Olins, A. L., Gould, T. J., Boyd, L., Sarg, B. & Olins, D. E. Hyperosmotic stress: in situ chromatin phase separation. *Nucleus* **11**, 1–18 (2020).

151. James, A. L., Dreiss, C. A., Steinmark, I. E., Suhling, K. & Yahioglu, G. Imaging mitochondrial matrix viscosity in live cells via fluorescence

lifetime imaging (FLIM) of fluorescent molecular rotors. *https://doi.org/10.1117/12.2508676* **10893**, 43–49 (2019).

152. Schlame, M. Protein crowding in the inner mitochondrial membrane. *Biochimica et Biophysica Acta (BBA) - Bioenergetics* **1862**, 148305 (2021).

153. Yuan, L. *et al.* Real-time imaging of viscosity in the mitochondrial matrix by a red-emissive molecular rotor. *Anal Methods* **13**, 3181–3186 (2021).

154. Mund, T., Lewis, M. J., Maslen, S. & Pelham, H. R. Peptide and small molecule inhibitors of HECT-type ubiquitin ligases. *Proc Natl Acad Sci U S A* **111**, 16736–16741 (2014).

155. Siegel, M. R. & Sisler, H. D. Inhibition of Protein Synthesis in vitro by Cycloheximide. *Nature 1963 200:4907* **200**, 675–676 (1963).

156. Parag, H. A., Raboy, B. & Kulka, R. G. Effect of heat shock on protein degradation in mammalian cells: involvement of the ubiquitin system. *EMBO J* **6**, 55 (1987).

157. Sizaire, F. *et al.* Refractive index sensing using Fluorescence Lifetime Imaging (FLIM). *J Phys Conf Ser* **45**, 223 (2006).

158. Laurent, V. M. *et al.* Gradient of Rigidity in the Lamellipodia of Migrating Cells Revealed by Atomic Force Microscopy. *Biophys J* **89**, 667–675 (2005).

159. Karlsson, T., Bolshakova, A., Magalhães, M. A. O., Loitto, V. M. & Magnusson, K. E. Fluxes of Water through Aquaporin 9 Weaken

Membrane-Cytoskeleton Anchorage and Promote Formation of Membrane Protrusions. *PLoS One* **8**, e59901 (2013).

160. Direito, I., Madeira, A., Brito, M. A. & Soveral, G. Aquaporin-5: from structure to function and dysfunction in cancer. *Cellular and Molecular Life Sciences 2016 73:8* **73**, 1623–1640 (2016).

161. Papadopoulos, M. C. & Saadoun, S. Key roles of aquaporins in tumor biology. *Biochimica et Biophysica Acta (BBA) - Biomembranes* **1848**, 2576–2583 (2015).

162. Liebermeister, W. *et al.* Visual account of protein investment in cellular functions. *Proceedings of the National Academy of Sciences* **111**, 8488–8493 (2014).

163. Pegoraro, A. F., Janmey, P. & Weitz, D. A. Mechanical Properties of the Cytoskeleton and Cells. *Cold Spring Harb Perspect Biol* **9**, a022038 (2017).

164. Loiodice, I. *et al.* Quantifying Tubulin Concentration and Microtubule Number Throughout the Fission Yeast Cell Cycle. *Biomolecules 2019, Vol. 9, Page 86* **9**, 86 (2019).

165. Yadav, S., Shire, S. J. & Kalonia, D. S. Viscosity Analysis of High Concentration Bovine Serum Albumin Aqueous Solutions. *Pharmaceutical Research 2011 28:8* **28**, 1973–1983 (2011).

166. Schindelin, J. *et al.* Fiji: an open-source platform for biological-image analysis. *Nat. Methods* **9**, 676–682 (2012).

167. Pliss, A., Zhao, L., Ohulchanskyy, T. Y., Qu, J. & Prasad, P. N. Fluorescence lifetime of fluorescent proteins as an intracellular

environment probe sensing the cell cycle progression. *ACS Chem Biol* **7**, 1385–1392 (2012).

168. Boyd-Shiwarski, C. R. *et al.* WNK kinases sense molecular crowding and rescue cell volume via phase separation. *bioRxiv* 2022.01.10.475707 (2022) doi:10.1101/2022.01.10.475707.

169. Keber, F. C., Nguyen, T., Brangwynne, C. P. & Wühr, M. Evidence for widespread cytoplasmic structuring into mesoscopic condensates. *bioRxiv* 2021.12.17.473234 (2021) doi:10.1101/2021.12.17.473234.

170. Vonderach, M., Byrne, D. P., Barran, P. E., Eyers, P. A. & Eyers, C. E. DNA Binding and Phosphorylation Regulate the Core Structure of the NF-κB p50 Transcription Factor. *J Am Soc Mass Spectrom* **30**, 128–138 (2019).

171. Yan, Q. *et al.* Nuclear factor-κB binding motifs specify Toll-like receptor-induced gene repression through an inducible repressosome. *Proc Natl Acad Sci U S A* **109**, 14140–14145 (2012).

172. Smith, E. L. *et al.* The regulation of sequence specific NF-κB DNA binding and transcription by IKKβ phosphorylation of NF-κB p50 at serine 80. *Nucleic Acids Res* **47**, 11151–11163 (2019).

173. Takashiba, S. *et al.* Differentiation of monocytes to macrophages primes cells for lipopolysaccharide stimulation via accumulation of cytoplasmic nuclear factor κB. *Infect Immun* **67**, 5573–5578 (1999).

174. Jones, E., Adcock, I. M., Ahmed, B. Y. & Punchard, N. A. Modulation of LPS stimulated NF-kappaB mediated nitric oxide production by PKCε and JAK2 in RAW macrophages. *J Inflamm* **4**, 1–9 (2007).

175. Bhattacharya, A., Agarwal, M., Mukherjee, R., Sen, P. & Sinha, D. K. 3D micro-environment regulates NF-κβ dependent adhesion to induce monocyte differentiation. *Cell Death & Disease 2018 9:9* **9**, 1–16 (2018).

176. Celik, E., Abdulreda, M. H., Maiguel, D., Li, J. & Moy, V. T. Rearrangement of microtubule network under biochemical and mechanical stimulations. *Methods* **60**, 195–201 (2013).

177. Kiuchi, T., Nagai, T., Ohashi, K. & Mizuno, K. Measurements of spatiotemporal changes in G-actin concentration reveal its effect on stimulus-induced actin assembly and lamellipodium extension. *Journal of Cell Biology* **193**, 365–380 (2011).

178. Rosette, C. & Karin, M. Ultraviolet Light and Osmotic Stress: Activation of the JNK Cascade Through Multiple Growth Factor and Cytokine Receptors. *Science (1979)* **274**, 1194–1197 (1996).

179. D'Alessio, A. *et al.* Targeting of Tumor Necrosis Factor Receptor 1 to Low Density Plasma Membrane Domains in Human Endothelial Cells. *Journal of Biological Chemistry* **285**, 23868–23879 (2010).

180. Bae, G. D. *et al.* Upregulation of caveolin-1 and its colocalization with cytokine receptors contributes to beta cell apoptosis. *Scientific Reports 2019 9:1* **9**, 1–10 (2019).

181. Roth, I. *et al.* Osmoprotective transcription factor NFAT5/TonEBP modulates nuclear factor-κB activity. *Mol Biol Cell* **21**, 3459–3474 (2010).

182. Farabaugh, K. T. *et al.* PACT-mediated pkr activation acts as a hyperosmotic stress intensity sensor weakening osmoadaptation and enhancing inflammation. *Elife* **9**, (2020).

183. Zhou, X., Cai, J., Liu, W., Wu, X. & Gao, C. Cysteinyl leukotriene receptor type 1 (CysLT1R) antagonist zafirlukast protects against TNF-α-induced endothelial inflammation. *Biomedicine & Pharmacotherapy* **111**, 452–459 (2019).

184. Weinelt, N. *et al.* Quantitative single-molecule imaging of TNFR1 reveals zafirlukast as antagonist of TNFR1 clustering and TNFα-induced NF-κB signaling. *J Leukoc Biol* **109**, 363–371 (2021).

185. Biswas, A., Alex, A. & Sinha, B. Mapping Cell Membrane Fluctuations Reveals Their Active Regulation and Transient Heterogeneities. *Biophys J* **113**, 1768–1781 (2017).

186. Shiba, H., Noguchi, H. & Fournier, J. B. Monte Carlo study of the frame, fluctuation and internal tensions of fluctuating membranes with fixed area. *Soft Matter* **12**, 2373–2380 (2016).

187. Taddei, M. L., Giannoni, E., Fiaschi, T. & Chiarugi, P. Anoikis: an emerging hallmark in health and diseases. *J Pathol* **226**, 380–393 (2012).

188. Kim, Y. N., Koo, K. H., Sung, J. Y., Yun, U. J. & Kim, H. Anoikis resistance: An essential prerequisite for tumor metastasis. *Int J Cell Biol* (2012) doi:10.1155/2012/306879.

189. Paoli, P., Giannoni, E. & Chiarugi, P. Anoikis molecular pathways and its role in cancer progression. *Biochimica et Biophysica Acta (BBA) - Molecular Cell Research* **1833**, 3481–3498 (2013).

190. Adeshakin, F. O. *et al.* Mechanisms for Modulating Anoikis Resistance in Cancer and the Relevance of Metabolic Reprogramming. *Front Oncol* **11**, 528 (2021).

191. Kamarajugadda, S. *et al.* Glucose Oxidation Modulates Anoikis and Tumor Metastasis. *Mol Cell Biol* **32**, 1893–1907 (2012).

192. Wang, G. X. *et al.* ΔNp63 Inhibits Oxidative Stress-Induced Cell Death, Including Ferroptosis, and Cooperates with the BCL-2 Family to Promote Clonogenic Survival. *Cell Rep* **21**, 2926–2939 (2017).

193. Kheradmand, F., Werner, E., Tremble, P., Symons, M. & Werb, Z. Role of rac1 and oxygen radicals in collagenase-1 expression induced by cell shape change. *Science (1979)* **280**, 898–902 (1998).

194. Grinnell, F., Zhu, M., Carlson, M. A. & Abrams, J. M. Release of Mechanical Tension Triggers Apoptosis of Human Fibroblasts in a Model of Regressing Granulation Tissue. *Exp Cell Res* **248**, 608–619 (1999).

195. Fiaschi, T., Cozzi, G. & Chiarugi, P. Redox Regulation of Nonmuscle Myosin Heavy Chain during Integrin Engagement. *J Signal Transduct* **2012**, 1–9 (2012).

196. Ma, Z., Liu, Z., Myers, D. P. & Terada, L. S. Mechanotransduction and anoikis: Death and the homeless cell. *http://dx.doi.org/10.4161/cc.7.16.6463* **7**, 2462–2465 (2008).

197. Verbon, E. H., Post, J. A. & Boonstra, J. The influence of reactive oxygen species on cell cycle progression in mammalian cells. *Gene* **511**, 1–6 (2012).

198. Patterson, J. C. *et al.* ROS and Oxidative Stress Are Elevated in Mitosis during Asynchronous Cell Cycle Progression and Are Exacerbated by Mitotic Arrest. *Cell Syst* **8**, 163-167.e2 (2019).

199. Signoretto, E. *et al.* Nocodazole Induced Suicidal Death of Human Erythrocytes. *Cellular Physiology and Biochemistry* **38**, 379–392 (2016).

200. Zheng, J. Y., Tan, H. L., Matsudaira, P. T. & Choo, A. Excess reactive oxygen species production mediates monoclonal antibody-induced human embryonic stem cell death via oncosis. *Cell Death & Differentiation 2017 24:3* **24**, 546–558 (2017).

201. Munnamalai, V. *et al.* Bidirectional interactions between NOX2-type NADPH oxidase and the F-actin cytoskeleton in neuronal growth cones. *J Neurochem* **130**, 526–540 (2014).

202. Kim, D. H. *et al.* Volume regulation and shape bifurcation in the cell nucleus. *J Cell Sci* **128**, 3375–3385 (2015).

203. Huber, M. D. & Gerace, L. The size-wise nucleus: nuclear volume control in eukaryotes. *Journal of Cell Biology* **179**, 583–584 (2007).

204. Lemière, J., Real-Calderon, P., Holt, L. J., Fai, T. G. & Chang, F. Control of nuclear size by osmotic forces in Schizosaccharomyces pombe. *Elife* **11**, (2022).

205. Pittas, T., Zuo, W. & Boersma, A. J. Engineering crowding sensitivity into protein linkers. *Methods Enzymol* **647**, 51–81 (2021).

206. Löwe, M., Kalacheva, M., Boersma, A. J. & Kedrov, A. The more the merrier: effects of macromolecular crowding on the structure and

dynamics of biological membranes. *FEBS Journal* **287**, 5039–5067 (2020).

207. Franco, R., Panayiotidis, M. I. & de La Paz, L. D. O. Autocrine signaling involved in cell volume regulation: The role of released transmitters and plasma membrane receptors. *J Cell Physiol* **216**, 14–28 (2008).